NEAR-FIELD PRESSURE DISTRIBUTIONS TO ENHANCE SOUND

TRANSMISSION INTO MULTI-LAYER MATERIALS

A Dissertation

Submitted to the Faculty

of

Purdue University

by

Andrew M. Jessop

In Partial Fulfillment of the

Requirements for the Degree

of

Doctor of Philosophy

December 2013

Purdue University

West Lafayette, Indiana

1. REPORT DATE	2. REPORT TYPE	3. DATES COVERED
10 DEC 2013	**Final**	**1 Aug 2010 - 31 Dec 2016**

4. TITLE AND SUBTITLE	5a. CONTRACT NUMBER
Near-field Pressure Distributions to Enhance Sounds Transmission into Multi-layer Materials / PhD Dissertation	**N/A**
	5b. GRANT NUMBER
	N00014-10-1-0958
	5c. PROGRAM ELEMENT NUMBER
	N/A

6. AUTHOR(S)	5d. PROJECT NUMBER
Andrew M. Jessop Mechanical Engineering Purdue University	**N/A**
	5e. TASK NUMBER
	N/A
	5f. WORK UNIT NUMBER
	N/A

7. PERFORMING ORGANIZATION NAME(S) AND ADDRESS(ES)	8. PERFORMING ORGANIZATION REPORT NUMBER
Ray W. Herrick Laboratories Purdue University West Lafayette, IN 47907	**64**

9. SPONSORING/MONITORING AGENCY NAME(S) AND ADDRESS(ES)	10. SPONSOR/MONITOR'S ACRONYM(S)
Office of Naval Research (ONR) 875 North Randolph Street - Suite 1425 Code 03R Arlington, VA 22203-1995	**ONR**
	11. SPONSOR/MONITOR'S REPORT NUMBER(S)
	N/A

12. DISTRIBUTION/AVAILABILITY STATEMENT
Approved for public release, distribution unlimited

13. SUPPLEMENTARY NOTES
N/A, The original document contains color images.

14. ABSTRACT

The large impedance difference between air and most solids prevents significant energy transfer from incident acoustic waves across the air-material interface. Refraction also plays a role in preventing acoustic transmission, as the wave speed difference between air and solid materials results in an increase of the resulting propagation angles, creating near-field pressure distributions in the solid material. By utilizing evanescent pressure distributions, which decay normal to the usual direction of propagation and are represented as plane waves propagating with complex angles, energy propagation through the interface can be increased in the subsonic region of wave propagation: i.e., where waves typically do not propagate into a material with any effectiveness. By using an array of sources, it is possible to produce evanescent pressure distributions in the solid. The way in which the characteristics of this array of sources affect the efficiency of the generation of evanescent pressure distributions are explored. Because high impedance materials can be paired to a lower impedance materials of interest to impede acoustical energy transmission, the wave propagation through multi-layer materials must be considered to give an full accounting of power transmission into structures. A model for wave propagation in multi-layer systems of solids and fluids was developed using wave potentials in each layer, allowing for coupling between material types and calculation of inter-layer states. By using wavenumber-frequency analysis, it is possible to target specific components in the multi-layer system and understand the particular wavetypes that cause energy propagation into the system.

15. SUBJECT TERMS

16. SECURITY CLASSIFICATION OF:			17. LIMITATION OF ABSTRACT	18. NUMBER OF PAGES	19a. NAME OF RESPONSIBLE PERSON
a. REPORT	b. ABSTRACT	c. THIS PAGE	**SAR**	**178**	
unclassified	**unclassified**	**unclassified**			

To my grandparents, George and Mary Jessop and Connie and Marty Melhorn. When they stressed the value of education, I don't think they ever thought I would run with it quite like this.

ACKNOWLEDGMENTS

Dr. J. Stuart Bolton served as my advisor for this project. His input, edits, and support were invaluable throughout my time at Purdue.

The support system, both intellectually and socially, provided by my labmates over the years was a tremendous asset. Tyler Dare, Sarah McGuire, Andrew Marshall, Frank Eberhardt, Ryan Schultz, Chlöe Giacomoni, Wong-Hong Choi, YangFan Liu, Mike Hayward, Nick Sakamoto, Andy McMullen, and Brandon Sobecki (and anyone else I might have left out) all contributed in some way to this document, whether they wanted to or not.

Jelena Paripovic, Jake Miller, Chris Watson, and Daniel Woods worked on the MURI project along with me. Best of luck to them in completing their studies. They, along with Drs. Davies, Rhoads, and Adams provided spectacular feedback through our weekly meetings and progress reports.

The support staff in the Herrick Laboratories shop and front office were a tremendous help as well. In the shop, Bob Brown, Frank Lee, Ron Evans, Fritz Peacock, and Gilbert Gordon assisted in setting up tests and maintaining and evaluating equipment.

TABLE OF CONTENTS

LIST OF TABLES

LIST OF FIGURES

Figure   Page

ABSTRACT

Jessop, Andrew M. Ph.D, Purdue University, December 2013. Near-Field Pressure Distributions to Enhance Sound Transmission into Multi-Layer Materials. Major Professor: J. Stuart Bolton, School of Mechanical Engineering.

The large impedance difference between air and most solids prevents significant energy transfer from incident acoustic waves across the air-material interface. Refraction also plays a role in preventing acoustic transmission, as the wave speed difference between air and solid materials results in an increase of the resulting propagation angles, creating near-field pressure distributions in the solid material. By utilizing evanescent pressure distributions, which decay normal to the usual direction of propagation and are represented as plane waves propagating with complex angles, energy propagation through the interface can be increased in the subsonic region of wave propagation: i.e., where waves typically do not propagate into a material with any effectiveness. By using an array of sources, it is possible to produce evanescent pressure distributions in the solid. The way in which the characteristics of this array of sources affect the efficiency of the generation of evanescent pressure distributions are explored.

Because high impedance materials can be paired to a lower impedance materials of interest to impede acoustical energy transmission, the wave propagation through multi-layer materials must be considered to give an full accounting of power transmission into structures. A model for wave propagation in multi-layer systems of solids and fluids was developed using wave potentials in each layer, allowing for coupling between material types and calculation of inter-layer states. By using wavenumber-frequency analysis, it is possible to target specific components in the multi-layer system and understand the particular wavetypes that cause energy propagation into the system.

CHAPTER 1. INTRODUCTION

Evanescent waves, i.e., waves that simultaneously propagate and attenuate, can be used to improve energy transmission into high impedance solid materials. By overcoming restrictions due to refraction at the air-solid interface, an evanescent wave incident on the surface can propagate energy into a solid material at a greater range of angles than classical plane waves. For high-impedance materials in multi-layer systems, geometry effects may provide addditional avenues for energy transmission into the material. An understanding of evanescent wave effects and their propagation into multi-layer materials will enable novel methods for excitation of those materials.

Acoustical transmission into solid materials is typically limited by the large impedance difference between air and the material. Lower-density solid materials have densities at least 1,000 times greater than air, and speed of sound differences of 10 times or more are typical. While the density difference can be overcome by exploiting the compressional and shear coupling effects in the material, refraction due to the difference in sound speed is a limit that prevents energy transmission beyond the critical angle of incidence.

The production of evanescent pressure distributions requires special sources. When using a multi-source array, each source can be given a phase and amplitude in such a way that the interference of the wavefronts produces the desired wave characteristics on a surface. The amplitudes and phases of these sources can be found by constructing a least-squares calculation of source strength that would approximate a wave at a particular angle of incidence. Factors such as the angle and frequency of the desired pressure distribution, as well as the geometry of the sources, all affect the ability of the source array to produce an approximation of the desired pressure distribution.

For more complex multi-layer structures, the geometry and component materials both affect the wave transmission into the system. Accounting for geometry will allow

for flexural waves and cut-on of modes in each layer, which will affect the total sound transmission through the system.

The wave propagation characteristics of materials with unknown properties can be found experimentally and used to improve the accuracy of wave propagation models. The waves resulting from such tests vary greatly with excitation location, and the materials tested need to be mounted properly to prevent damping and geometry constraints. Understanding these effects and the waves produced by different experimental conditions will allow for assessment of wave propagation and material properties.

1.1   Motivation

The research undertaken in this project was part of a multi-university research initiative (MURI) focused on non-contact excitation of energetic materials. There are existing spectrographic methods for large-standoff detection of chemical signatures, but when these chemical signatures are weak, excitation is needed to produce more outgassing of the energetic material. Electromagnetic methods of excitation can be defeated be installing a dielectric buffer around the material; in those cases, to excite the materials, mechanical displacement is necessary. Acoustical excitation may be able to provide a large-standoff method for excitation.

A typical scenario involves an energetic material behind a thin, rigid material. Such a material would serve as both a container for the energetic material (which typically needs to be cast from a liquid state) as well as concealment of the energetic material. Examples would be a milk jug, which is composed of a thin layer of plastic, or an aluminum can. There may be additional barriers serving as concealment, as well as imperfections in the coupling between the barrier materials and the energetic material that produce air gaps and further limit energy transmission.

Related aspects of the research performed by other reseachers in this overall project involve classification of the coupling of the materials, its response to low

frequency excitations, and extensive exploration of the thermo-physical properties that may allow for heating and outgassing.

1.2 Contribution of Research

The primary goal of this research was the exploration of evanescent wave energy transfer into multi-layer materials. To that end, several methodologies to increase our understanding of evanescent waves and techniques for simulation of wave propagation through multi-layer materials have been developed.

A detailed discussion of evanescent waves in air, as a result of complex angle of transmission along a plane, will allow for the development of a model exploring energy transfer of evanescent waves across the fluid-solid interface. While this model is based on previous formulations of fluid-solid interaction, an accounting for the effects of evanescent waves has not previously been undertaken.

Wave propagation in multi-layer materials is modeled by using wave potentials in each layer to allow for inter-layer material state calculation. In the model, the incoming and outgoing waves are separated, which allows for calculation of the intensity of each wave and a more accurate understanding of the effects of each layer on energy propagation. In addition, since the incoming and outgoing waves are separated, an evanescent incident wave can be accurately represented.

A detailed accounting is also given of the effects of excitation and material mounting conditions on wave propagation measurements. This information can be used to improve classification of wavetypes in unknown materials.

Generation of plane and evanescent waves using multi-source methods was also explored and a simple model was developed. The contribution of the research on this subject is a thorough exploration of the effects of the incident wave properties and source geometry on the ability to produce desired pressure distributions in energetic materials.

1.3   Outline

After a discussion of previous work relevent to this research is given in Chapter 2, Chapter 3 begins with a discussion of evanescent waves and how they can be represented using complex angles. An evanescent wave's ability to increase energy transmission in the subsonic region of incident angles will be presented using closed-form solutions of fluid-solid interaction. An assessment of the evanescent waves that are generated in the near-field of a monopole then allows for experimental exploration of their effects on energy transmission into solids.

Chapter 4 is focused on multi-source methods for generating evanescent pressure distributions. It will begin with a discussion of the radiation effects of simple sources and the incident wave that is to be modeled, before presenting a least-squares formulation for approximating incident waves using multiple simple sources. An analysis of the effects of incident wave parameters and source geometry follows, including a comparison of monopole and dipole efficiency in modeling.

In Chapter 5 a model for multi-layer wave propagation using wave potentials is presented. Several representative models are explored to show how multi-layer systems affect wave propagation.

Chapter 6 contains a description of experimental tests of wave propagation in both previously classified and unknown materials. These tests allowed for an exploration of mounting and excitation effects on the resulting vibration in the material, and their effects on wave properties.

Finally, a summary of the research findings and recommendations for continuing avenues of research are given in Chapter 7.

CHAPTER 2. PREVIOUS RESEARCH

The results of the literature survey are organized into three general areas of research: near-field effects on sound transmission; wave propagation in multi-layer systems; and generation of arbitrary pressure distributions. The chapter ends with a summary of what is and is not known is these areas that is relevent to the current research.

2.1 Near-Field Effects on Sound Transmission

Much research has been performed regarding acoustic transmission into solids using waves in the ultrasonic frequency domain. For example, Gan, Hutchins, Billson, and Schindel [1] have looked at the transmissibility of ultrasonic waves through material samples. Many of these methods exploit resonances of the structure or the microstructure of the material being investigated. However, ultrasound is only useful in applications where propagation distances through air are short because the decay of ultrasonic waves in air is significant; Fox, Khuri-Yakub, an Kino [2], for example, found decay levels of 52 dB over 40 centimeters. Because a primary goal of the work reported here is large-standoff investigation of materials, ultrasonic methods will not be useful.

The basic theory of solid-fluid interaction is explained by Brekhovskikh [3]. By equating the pressure and velocity in the wave-carrying fluid with that on the solid surface, Brekhoskikh derived the equations for acoustic reflection and transmission that are used as the basis for this study. He derived transmission coefficients for both the compressional and shear waves propagating into a solid, and performed a thorough exploration of various regions of transmission, such as the supersonic and subsonic regions of both the compressional and shear waves. Brekhovskikh also derived transfer matrices for multi-layer propagation.

The most common high-impedance-difference interface studied is the air-water interface, due to its naval applications. Hudimac [4] looked at the effects of refraction across the interface on energy transmission, deriving iso-intensity lines for sound originating in air and transmitted into water. Weinstein and Henney [5] used that work as the basis to calculate monopole sound transmission into water, looking at energy transmission as a function of height above the surface. Young performed experimental measurements of sound transmission between water and air [6]. From his measurements, he found pressure levels equal to those predicted by a theory based on ray-tracing, with an accuracy of 1-2 dB at most levels.

Meecham looked at sound propagation into water from an airborne source [7]. He formulated conditions in which acoustical energy from the air would propagate into the water at small grazing angles caused by refraction in the air. He also found transmission enhancement effects due to surface roughness.

Bobrovnitskii [8, 9] briefly discussed the possibility of energy flow from evanescent waves. He shows that the power resulting from a combination of evanescent waves in opposing directions will lead to interaction between the otherwise out-of-phase velocity and pressure components, resulting in an intensity equal to the cross-product of the two waves' amplitudes.

Godin [10, 11, 12, 13] has explored theoretical conditions under which a high-impedance difference boundary becomes acoustically transparent due to evanescent waves from a source. In his research on both the air-water interface [10, 11, 12] and the air-solid interface [13], he formulated equations for transmission from a monopole source in the higher-impedance solid material into the fluid. Godin found significant power flux across the interface due to inhomogeneous wave components in a monopole close to the interface. For the air-solid transmission interface, Godin also accounted for various lossy wavetypes that are typically seen in this type of transmission. He also investigated the effects of interface roughness; he found that there is no significant additional transmission due to roughness that is much smaller than a wavelength in the incident fluid [10]. Godin's theory was tested by Calvo, McDonald, Nicholas,

and Orris, who further developed the formulation to account for total power flux when accounting for reflections from the surface [14], and performed preliminary experimental measurements [15]. However, in these formulations the authors made use of inhomogeneous wave components in water which are supersonic in air; the inverse of this problem cannot take advantage of such a range of inhomogeneous waves.

The coupling of acoustical energy and flexural waves in materials has been described by Fahy and Gardonio [16]. Flexural waves typically have much lower wave speeds than longitudinal or shear waves in a material, and they can therefore be excited across a much broader range of incident angles. Flexural waves are not useful for formulation of sound power transmission across a material interface, however, because the flexural wave is structure-dependent and will not provide general transmission across a variety of different geometries.

Park et al. [17] discussed the use of metamaterials in increasing the transfer of electromagnetic waves into materials. By using a structure with an effective cell size much smaller than a wavelength, a negative density that enhances the transmission of an evanescent electromagnetic wave can be created. However, despite the use of metamaterials being shown to increase the acoustic transmission in classical wave propagation [18], these evanescent transmission effects cannot be seen in acoustical materials because mechanical dissapation negates the effects of the negative density in the metamaterial.

2.2   Wave Propagation in Multi-Layer Systems

Folds and Loggins [19] expanded on the sound transmission work performed by Brekhovskikh [3] to create propagation matrices for general cases of multi-layer solids. He calculated ultrasonic wave propagation through single-layer and three-layer panels, and found good correlation between the model and experimental results for lower grazing angles.

Pierce [20] explains more general theories for multi-layer propagation, such as the effects of inter-layer states and the ideal properties for a coupling layer. He also considers flexural waves, though as an independent wavetype rather than through coupling effects of material waves in a thin plate system.

Brouard, Lafarge, and Allard formulated a system of linear equations to model sound propagation in mixed fluid-solid layered systems [21]. By working from similar matrix-based methods for sound propagation in fluids and solids, Brouard developed a matrix relating the pressure and velocity of waves propagating through multiple layers. At interfaces where the medium changes, such as from fluid to solid, a coupling matrix is used to equate the different types of pressure and velocity amplitudes. The use of this formulation allows for generation of transfer functions between the incoming pressure and the resulting pressure or velocity at an internal layer.

Auld's investigated propagation in waveguides, and derived dispersion relationships for the different wavetypes in the system [22]. In his calculations using existing models, based primarily on Folds and Pierce's formulations, he found dispersion relationships showing material and flexural waves in constrained systems. He explained the relationship of cut-on frequencies for particular modes of vibration and how they transitioned into waveguide-like behavior at higher angles of incidence. He also showed how coupling of material waves can create Lamb waves, such as flexural and dilatational waves.

Maidanik and Dickey developed a methodology for deriving a low-reflectivity material [23]. In a two-layer material consisting of a thin plate and a thicker material layer underneath, certain conditions for resonance could be met that couple the flexural waves in the plate with other wavetypes in the material to produce a low-reflectivity condition. They explored the material combinations under which this could occur as well.

Mead has looked at vibration propagation through periodic systems [24, 25]. He accounted for the presence of the modes of individual layers of a multi-layer sys-

tem, and found resonance conditions that would cause ideal wave propagation in the system.

In previous work by the author [26] on assessing the effects of deformation on the tire acoustic mode, the author used a wave potential-based method in a system of linear equations. The work was built upon a model developed by Thompson [27], who used wave potentials across a simpler geometry to formulate a closed-form solution for the effects of tire deformation on the tire's acoustic mode.

Grosh and Williams developed a wavenumber-frequency decomposition technique to visualize wavetypes in a material [28]. In addition to other techniques such as Prony series decomposition, often used in modal analysis of vibrations in structures, the use of wavenumber-frequency decomposition allows for identification of vibrational modes. Grosh et al. applied this technique to both measured and simulated data.

Wahl and Bolton calculated wave speed properties for dispersive and non-dispersive waves in a system using Wigner distributions [29]. By visualizing the amplitude of a pulse versus time and frequency, the arrival time of waves and the resulting speed of wave propagation can be determined. By filtering elements of the Wigner distribution, they were able to determine the energy carried by various wavetypes.

Bolton, Kim, and Song others have used a wavenumber domain representation of vibration to visualize wavetypes in a system [30, 31, 32]. By visualizing tire vibration in the wavenumber-frequency domain, the wavetypes specific to tire treadband vibration were isolated, and the damping in the treadband could be assessed.

In the previous research discussed here, phenomena evident in anomalous fluid-solid transmission has been identified. By further classifying these effects, there exists the possibility of controlling and utilizing them to deliver desired excitations to a multi-layer material. The combination of the previously-developed methodologies for simulating multi-layer acoustical propagation with the technique of wavenumber-frequency visualization will allow for isolation of particular wavetypes in the system. Incident evanescent can be created by expanding upon the techniques shown in previous research of wave front synthesis, considered next.

2.3 Generation of Arbitrary Pressure Distributions

Typical multi-source methods entail the use of an array of sources with selectively-phased outputs designed to produce an optimal amplitude output. For example, beamforming techniques [33, 34] are applied to source arrays with the goal of amplifying an output signal in a direction of interest. However, the present focus was on creating a specified pressure distribution, rather than amplifying a source.

In other multi-source methods the array of sources was often used to generate a plane wave: i.e., the sources were phased to generate a relatively large region of plane wavefront. Berkhout, De Vries, and Vogel looked at using multiple sources to generate plane waves in the far-field [35] by using a loudspeaker array. By selectively phasing the sources, a larger wavefront could be generated by combining the smaller wavefronts of the component sources. Their research was primarily focused on simulating large wavefronts at a particular location; such a method could not generally produce plane waves at an angle to an interface surface.

Chang, Choi and Kim looked at generating plane waves in free space using a spherical array of loudspeakers [36]. In his method, he generated a plane wave field using multiple sound sources, but the dependence on the spherical geometry surrounding the region of interest makes it unfeasible for our purposes.

Russell, Titlow and Bemmen [37] looked at the power output and directivity patterns for monopoles, dipoles, and quadrupoles and measured how the theoretical formulations of such sources match experimental approximations. He found that his experimental approximations matched theory reasonably well at low frequencies, but were limited by geometry and diffraction at higher frequencies.

Bolton, Beauvilain, and Gardner experimented with the generation of pressure distributions in a region by using simple sources, particularly dipoles and quadrupoles [38]. Through selective phasing of colocated simple sources, the radiation characteristics of the system could be varied, including variation of the angular pressure

distribution and reduction of the near-field intensity. These theories were verified in later work [39] using four uniquely-arranged sources.

Ahrens and Spors developed methods for reproduction of plane waves using circular [40] and linear arrays [41]. In their formulation, they discretized continuous sound sources to generate the desired plane wave field. By calculating a driving function for the continuous distribution that gave an exact answer for the pressure distribution, then discretizing that driving function into an array of point sources, they were able to approximate the sound field produced by the discrete source. They also studied driving function and discretization techniques to minimize the error associated with their linearization method. These theoretical formulations will be difficult to adapt to loud speaker arrays used in experimental testing due to the complexity of the driving functions; a methodology that allows for arbitrary angular variation of a discrete source would be more useful.

Robin, Berry, Moreau, and Dia [42] used multi-source methods to generate reproducible turbulent pressure fields for use in structural acoustics. In their approach they used both wavefront synthesis (as defined by Berkhout) and near-field holography theory (inverted from its typical use in sound source detection) to generate the wave field on a surface by using controllable sources. To simulate the turbulent boundary layer properties by using a limited array of variables, they used relationships between the desired wavelength of reproduction and the number of sources used.

Wang and Wu formulated a method for generating pressure distributions resulting from irregularly-shaped vibrating sources [43]. They generated a set of orthonormal functions from the modes of structure, then formed those equations into a least-squares solution to calculate the combination of modes that produced the measured pressure distribution. Wu expanded on this approach and applied it to a radiating structure in an enclosed vibrating space, and combined those principles with nearfield acoustical holography to create a computationally efficient method for sound field prediction [44, 45].

Kirkeby and Nelson formulated a method of generating a complex pressure distribution from a series of simple sources [46]. Their method consists of altering the amplitude and phase of a system of monopoles in a given geometry. They accomplished this by generating a series of linear equations, consisting of a matrix of Green's functions between the sources and pressure distribution at a point, multiplied by the unknown phase amplitudes of the sources, to equal the resulting pressure distribution at a series of discrete points. By finding a least-squares solution to this matrix, they were able to find a vector of source phases that approximated the pressure distribution. They also established error bounds for the solution for different geometry and frequency types.

2.4   Conclusions

The work described in this thesis on evanescent wave energy propagation into solid materials is an expansion of the theory developed by Brekhovskikh [3]; his work allows for evanescent incident waves as part of the general solution for fluid-solid transmission but does not consider the consequences of using such waves. By formulating evanescent waves incident on the surface by using complex angles, it can be shown that significant energy transmission across the fluid-solid interface is possible. Similiar propagation characteristics were shown in the near-field of a monopole by Godin [10, 11, 12, 13]; however, in the present work further classification is provided by using specifically generated evanescent waves rather than those already present in the near-field. In his research Godin also established the basis for the experimental portion of the research (reported here) on evanescent wave transmission into solid matrials.

The formulation of evanescent wave pressure distributions described in Chapter 4 is an extension of the work of Kirkeby et al [46]. By using their system of linear equations, an accounting for the effects of source geometry and desired pressure distribution can be made. Other work, such as that performed by Russell [37] on

experimental verification of monopole and dipole properties, were useful in assuring experimental reproductivity of the distribution produced.

The model for wave propagation through layers used in this research was initially developed by Brouard [21], who expanded the transfer matrix approach for wave propagation. His model, a system of linear equations, accounts for both forward- and backward-propagating waves in the system. The use of wave potentials as inputs to the system of equations is based on previous work by Jessop [26] (which itself is taken from the work of Thompson [27]) to account for wave potentials rather than material states, thus allowing for inter-layer state and intensity calculation.

CHAPTER 3. NEAR-FIELD EFFECTS ON SOLID-FLUID ACOUSTICAL TRANSPARENCY

The characteristics of evanescent pressure distributions can be used to enhance sound propagation through the air-solid interface. In typical air-solid propagation, the difference in density and wave speed across the interface results in very low energy transmission. The difference in wave speed also causes extreme refraction through the interface; pressure in the solid will then decay quickly and there will be little velocity propagation into the material. The region wherein refraction reduces energy propagation into the material is known as the subsonic region; it is characterized by the normal speed of sound of a wave into the material being less than the material's wave propagation speed. By inverting the typical near-field effects seen in the subsonic region of acoustical transmission and specifically generating evanescent pressure distributions, it will be a shown that a larger portion of the energy in the sound wave can be transmitted into the solid material.

Evanescent pressure distributions can be modeled by a plane wave propagating at a complex angle. As shown by Brekhovskikh [3], the complex angle represents decay or growth in the wave amplitude normal to the direction of propagation. Such distributions are typically seen as the result of subsonic acoustic transmission (i.e., at incidence angles larger than the critical angle); however, intentional generation of such a distribution may provide a means of controlling the angle of propagation and energy transfer across an interface.

This chapter begins with a description of evanescent pressure distributions made by the inclusion of complex wavenumbers and angles into the standard plane wave formulas. A discussion of the theory of acoustical transmission through an interface will lead to an exploration of the effects of evanescent pressure distributions in acous-

tical transmission. The evanescent pressure distributions generated by a monopole will also be discussed and verified experimentally.

3.1 Evanescent Plane Waves

3.1.1 Fundamentals of Wave Propagation

The pressure of a propagating plane wave at a point in space, $\vec{x}$, is:

$$p = Ae^{j\vec{k}\cdot\vec{x}}e^{-j\omega t} , \tag{3.1}$$

where A is the amplitude (and initial phase) of the wave, $\vec{k}$ is the wavenumber vector (the rate of change in phase per unit distance), and ω is the radian frequency (the rate of change in phase over time, equal to 2π times the frequency f in radians per second). The components of $\vec{k}$ specify a direction of propagation for the wave. For steady-state formulations, the phase change with time, $e^{-j\omega t}$, does not have an impact on the parameters discussed here, and is excluded from all future equations for brevity.

The material's wavenumber $k = |\vec{k}|$, which is the phase change per unit distance in the direction of wave propagation, is a unit inversely proportional to the wavelength of sound, λ, and is related to frequency by the speed of sound in the material c:

$$k = \frac{2\pi}{\lambda} = \frac{\omega}{c} . \tag{3.2}$$

A wave propagating over a plane surface will have a trace wavenumber (and wavelength) along the surface that is different from the material wavenumber. If a wave is incident on a surface oriented along the x-y plane at an angle θ from the normal, $\hat{z}$, as depicted in Figure 3.1, the effective wavenumber along the surface in the $\hat{x}$-direction is:

$$k_x = k \sin\theta . \tag{3.3}$$

At normal incidence, k_x is 0, representing a uniform phase over the entire incident plane. With increasing angle, k_x approaches the incident material wavenumber. Note that because the wavenumber is inversely proportional to the speed of sound, the trace sound speed on the surface is larger than the speed of sound in air for all non-grazing ($\theta < 90°$) angles.
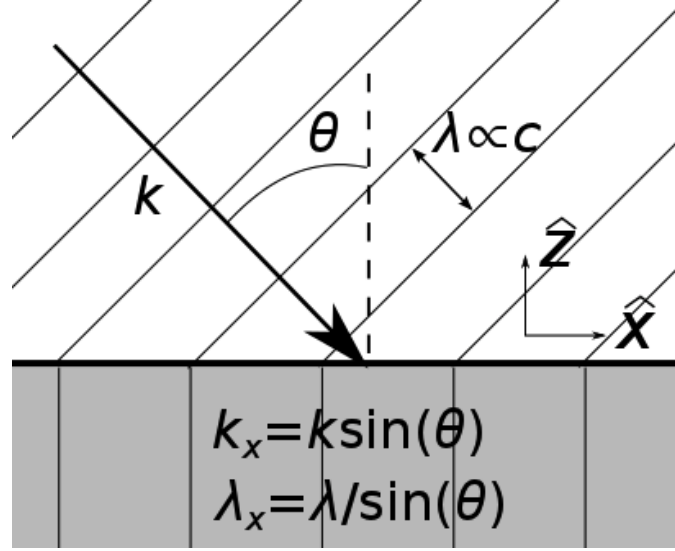
Figure 3.1. Plane wave incidence on a plane surface. An incoming wave with $k = \omega/c = 2\pi/\lambda$ at an angle θ will have a trace wavenumber on the surface of $k_x = k\sin(\theta)$.

A purely real value of k is typical of the wavenumber of a plane wave, thus representing simple phase change with distance. For a complex k value, represented as the sum of the real and imaginary components $\vec{k}_r + j\vec{k}_i$, the plane wave equation becomes:

$$p = Ae^{j(\vec{k}_r + j\vec{k}_i)\cdot\vec{x}} = Ae^{j\vec{k}_r\cdot\vec{x}}e^{-\vec{k}_i\cdot\vec{x}} , \qquad (3.4)$$

with the imaginary portion, $k_i = \Im(\vec{k})$, used to represent the exponential decay or growth of an evanescent wave. For these waves, the envelope of the pressure amplitude will be increasing or decreasing (for our purposes "decay/decrease" will henceforth be used in lieu of accounting for both possible signs of k_i) with distance (away from a defined origin) in the direction of propagation. The ratio of the imaginary component,

k_i, to the real component, k_r, defines how much decay occurs over each period of oscillation. Over a wavelength of $\lambda = 2\pi/k_r$ the phase increases by 2π; when the wavenumber is complex, the wave decays by a factor of $e^{-2\pi k_i/k_r}$ per wavelength (for a 1% ratio of imaginary to real component, a factor of 0.93 per wavelength).

A sample of a wavetype with complex wavenumbers, as viewed in the direction of propagation, is shown in Figure 3.2. For a negative value of k_i, the wave will decay with distance; a positive value of k_i will represent an increasing wave amplitude.
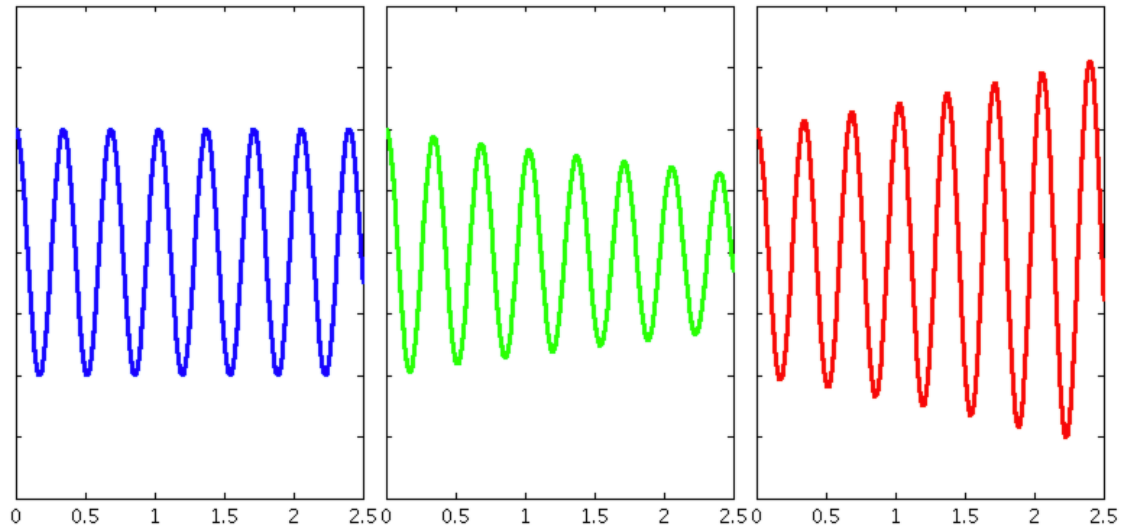
Figure 3.2. The effect of complex wavenumbers on waveform shape. The undamped wave is shown in the left plot. A 1% damping (center plot) will cause the amplitude to decrease over distance, while a 1% negative damping (right plot) will cause the amplitude to increase over distance.

3.1.2   Generation of Evanescent Waves Using Complex Angles

A complex angle of propagation can be used to represent another type of wave that satisfies the wave equation. The sine or cosine of this complex angle will result in complex wavenumber components, with the resulting wavenumber obeying the wave

equation. The complex directional wavenumbers $\tilde{k}_x$ and $\tilde{k}_z$, are determined by the sine and cosine of a complex angle $\tilde{\theta} = \theta_r + j\theta_i$:

$$
\begin{aligned}
\tilde{k}_x &= k\sin(\theta_r \pm j\theta_i) = k\sin\theta_r\cos(j\theta_i) \pm k\cos\theta_r\sin(j\theta_i) = \\
&\qquad k\sin\theta_r\cosh\theta_i \pm jk\cos\theta_r\sinh\theta_i \\
\tilde{k}_z &= k\cos(\theta_r \pm j\theta_i) = k\cos\theta_r\cos(j\theta_i) \mp k\sin\theta_r\sin(j\theta_i) = \\
&\qquad k\cos\theta_r\cosh\theta_i \mp jk\sin\theta_r\sinh\theta_i \ ,
\end{aligned}
\tag{3.5}
$$

yielding a real component in the direction of propagation and an imaginary component that is normal to the direction of propagation, as evidenced by the $\cos(\theta_r)$ component in the imaginary part of sine of the complex angle, and a similar $\sin(\theta_r)$ term in the cosine. For small imaginary angles, the hyperbolic cosine is close to 1; therefore, the resulting directional component of the angle (the real component of the cosine of the complex angle) will only deviate slightly from the direction of propagation for a purely real angle. The imaginary component of the sine or cosine of the complex angle specifies the direction of decay of the evanescent wave, with the hyperbolic sine of the imaginary component indicating the rate of decay.

Because the complex angle follows the standard trigonometric identity $\sin^2(\tilde{\theta}) + \cos^2(\tilde{\theta}) = 1$, the use of the complex angle allows the wave propagating at that angle to continue to obey the wave equation, which is satisfied by the resulting directional vectors being equal to the wavenumber in the material:

$$
\tilde{k}_x^2 + \tilde{k}_z^2 = k^2\sin^2(\tilde{\theta}) + k^2\cos^2(\tilde{\theta}) = k^2 \ ,
\tag{3.6}
$$

which is an essential component for integrating evanescent waves into existing theory. Note that a complex angle acting on a real wavenumber gives a very different result than a complex wavenumber; as shown in Figure 3.3, a complex angle results in a decay perpendicular to the direction of wave propagation, while a complex wavenumber (and a real angle) decays in the direction of propagation. For a complex value of the speed of sound, c, which is typically used to model damping in lossy materials, the

wave equation will be satisfied by a complex wavenumber value. When using complex angles, the imaginary component of the wavenumber transverse to the direction of propagation represents a decay per wavelength in the direction perpendicular to the propagation direction; higher wavenumber magnitudes will result in faster decay per distance than lower wavenumbers for the same complex angle (note that the wavenumber is proportional to frequency).
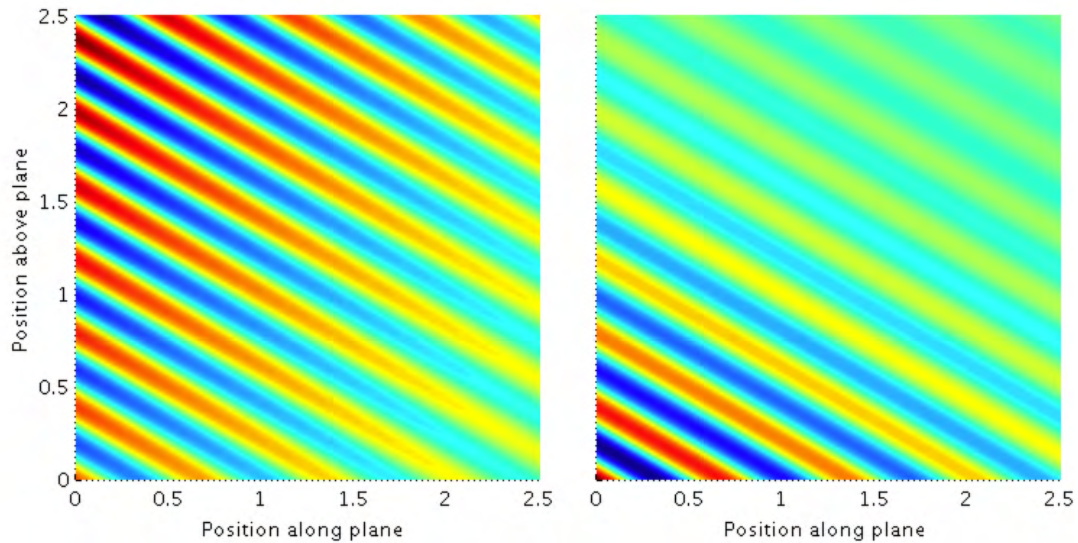
Figure 3.3. The effects of a complex angle of propagation (left) compared to complex wavenumber (right). The left pressure distribution is a real wavenumber with a complex angle, causing a decay normal to the direction of propagation. The right distribution shows a complex wavenumber propagating along a real angle; the decay is along the direction of propagation.

When incident upon a surface, an evanescent wave's trace pressure decays with distance over the surface. Figure 3.4 compares the resulting trace pressure distributions of conventional plane and evanescent plane wave fields. Since our concern is with interaction occuring at a material interface, generation of the pressure distribution through a volume of space is incidental; in Chapter 4 methods for generating these distributions on the surface using non-plane wave sources will be explored. The

use of complex angles is a convenient way to express how these pressure distributions behave through the interface.
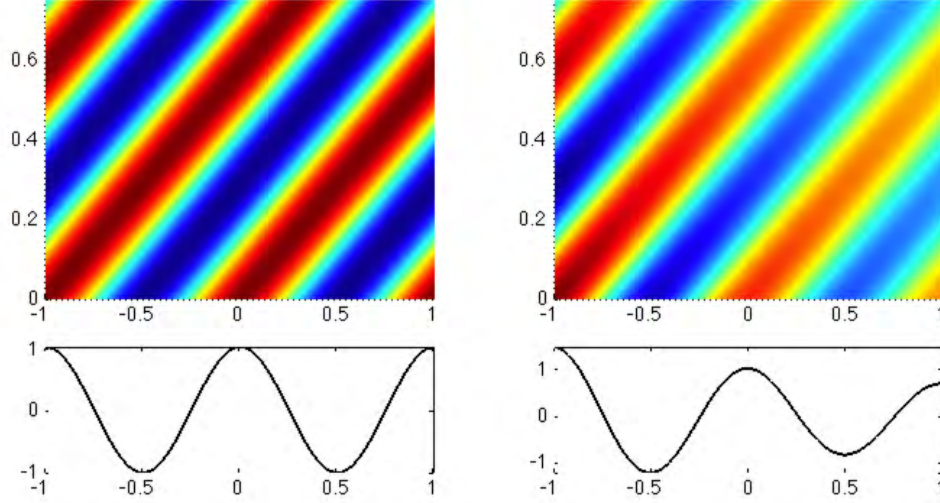
Figure 3.4. The resulting trace pressure generated by incident plane and evanescent waves upon a surface. The upper plots show propagation over two-dimensional space above the incident plane, while the bottom plots show the trace pressure distribution at the $z = 0$ surface. While the trace pressure of the 30 degree incident plane wave shown on the left does not decay over distance, the resulting trace pressure of the $30 + .1j$ degree incidence plot on the right decays along the plane surface.

3.1.3 Pressure and Velocity Phase Differences in Evanescent Waves

So far we have only discussed classification of evanescent waves by their change in amplitude over distance. However, evanescent waves can be discerned at a single point in space by the difference in phase between the wave's pressure and velocity. The velocity along the direction of propagation, v, of a plane wave is:

$$\vec{v} = \frac{1}{j\omega\rho} \frac{dp}{d\vec{x}} \; . \tag{3.7}$$

Given the plane wave pressure equation in Equation 3.1, the velocity along the direction of propagation will be:

$$v = \frac{\tilde{k}}{\omega \rho} p \ ,$$

(3.8)

and the difference in phase between p and v will be equivalent to the phase of the wavenumber, $\angle \tilde{k}$. For a complex wavenumber, $\tilde{k} = k_r + j k_i$, the resulting phase angle, ϕ, is equal to:

$$\phi = \angle \tilde{k} = \arctan\left(\frac{k_i}{k_r}\right) \ .$$

(3.9)

From this equation, it can be seen that there is no phase difference between the pressure and velocity of a classical plane wave with $\tilde{k} = k_r$, and a 90 degree difference for a purely imaginary angle of propagation $\tilde{k} = k_i$. For a complex angle of propagation, the phase difference between the velocity and pressure of a evanescent wave will vary between 0 and 90 degrees, with larger phase differences corresponding to a more signficantly-decaying wave.

The use of complex angles provides a way to simulate waves with evanescent propagation patterns, and can be used to express refraction characteristics, which is a key component of wave transmission across an interface.

3.2 Evanescent Wave Transmission Across An Interface

3.2.1 Theory and Principles

In a fluid, which cannot sustain shear stress, the only type of wave that can propagate is a longitudtinal wave, where the particle velocity of the wave is in the direction of propagation. Such waves are also known as compressional waves because the resulting pressure, p, causes compression and expansion as the wave propagates. A solid can sustain shear stress and has a stress vector, $\vec{\sigma}$, instead of a single pressure; therefore, an additional wavetype with speed of propagation, b, is added that accounts for

shear motion normal to the direction of propagation. In a three-dimensional analysis, the shear wave can have components of stress and velocity in independent directions normal to the direction of propagation; for our purposes in a two-dimensional formulation, the shear wave stress will only have a single amplitude, σ_t. The compressional wave will have a stress, σ_l, which is equivalent to the pressure p in a fluid. Both compressional and shear waves are present in a solid material, and both must be accounted for in fluid-solid propagation. There are additional wavetypes that may be present in solid materials, such as Lamb waves that cause flexural and dilitational motion; these waves result from the coupling of the pressure and shear waves in constrained materials. Because these are geometry-dependent, they are not considered in this formulation.

The acoustical impedance of a material is the ratio of stress σ (for fluids, the scalar $-p$ may be used to designate the pressure; note that σ is conventionally the negative of p) over the particle velocity, v, of a propagating wave in the material. For a solid or fluid, the characteristic impedance Z is:

$$Z = \frac{\sigma}{v} = \rho c, \tag{3.10}$$

where ρ is the density of the material (ρ_0 and c_0 will be used as the density and speed of sound of air, respectively, with the '0' subscript representing the material properties of incident acoustic waves in air throughout this document). A material that supports compressional and shear waves will have impedances for each wavetype, proportional to their propagation speeds. Table 3.1 shows the wave speed and density for several common materials.

Ideal energy transmission will occur between materials of equivalent impedance; for interfaces with a large impedance difference, most of the energy in a wave will reflect back into the incident material. For typical air-solid interaction, the impedance difference is several orders of magnitude, and a very small amount of the energy is propagated into the material even before accounting for refraction of the wave.

Table 3.1.   Density and wave speed of materials of interest for impedance calculation.

Material	Density ρ kg/m^3	Compressional wave speed c m/s	Shear wave speed b m/s
Air	1.2	343	N/A
Water	998	1,480	N/A
Aluminum	2,700	6,110	3,040
Steel	7,850	5,850	3,190
Polycarbonate	1,160	1,700	1,410

Similar to a material's wavenumber, the impedance is a scalar representing the properties in the material, which can be represented in a propagating wave as vector quantities oriented along the direction of propagation. The magnitude of a wave's impedance vector is the material impedance, and each component's amplitude is a function of the angle of propagation. In a fluid, the pressure is a scalar quantity, and the velocity of the wave is oriented along a vector; therefore, the wave impedance's components will be oriented similarly to the velocity's. For a surface in the $x - y$ plane with a normal vector oriented along the $\hat{z}$ axis (as will be considered in the rest of this formulation), the impedance normal to the material is:

$$Z_z = \frac{p}{v_z} = \frac{p}{|\vec{v}| \cos\theta} = \frac{Z}{\cos\theta} \ . \tag{3.11}$$

Impedance-matching between an incident wave and a larger-impedance material can therefore be performed by changing the angle of the incidence of the wave. However, for most air-solid interfaces with large material impedance differences, the angle that will match the normal impedances is extremely close to grazing, making it physically impractical to implement. Even with the ideal angle of incidence required to obtain

an impedance-matched system, the angle of propagation for the transmitted wave due to refraction at the interface can reduce the effective energy propagation into the material.

A difference in the speed of sound between two materials causes refraction across the interface. The speed of any propagating waves will be constant parallel to the surface: i.e., the trace wave speed is common between the incident and transmitted media. Therefore, for a wave incident at an angle to the surface: the resulting angles of the compressional and shear waves can be calculated from Snell's law:

$$\frac{c_0}{\sin(\theta_0)} = \frac{c_1}{\sin(\theta_1)} = \frac{b_1}{\sin(\gamma_1)} \ , \tag{3.12}$$

where c_1 and θ_1 are the compressional wave speed and propagation angle of the transmitted wave, respectively, and b_1 and γ_1 are their shear equivalents. The effect of refraction across the surface is that the angle of propagation into a higher-speed material will be a larger than that of the incident wave.

For a wave incident upon a plane surface, the angle of incidence determines the k_x component on the surface; this component is the same for both the incident and transmitted waves, so $k_x = k_{1x} = k_{0x}$: i.e.,

$$k_0 \sin \theta_0 = k_1 \sin \theta_1 = \kappa_1 \sin \gamma_1 \ . \tag{3.13}$$

The resulting k_{1z} of the transmitted wave is determined by calculating the remaining component of the wavenumber vector:

$$k_{1z} = \sqrt{k_1^2 - k_x^2} = k_1 \cos \theta_1 \ , \tag{3.14}$$

and the reduction in k_z due to the wavenumber changes across an interface can be seen as another aspect of refraction.

The formulation of k_z as the remaining component after removing the trace wavenumber is helpful to understand subsonic propagation. When the trace wavenumber is higher than the material wavenumber, the trace speed of sound on the surface

is lower than the material wave speed. In this case, the wave component propagating into the material is supersonic (faster than the material wave speed), and will propagate like a conventional plane wave. If the trace wavenumber exceeds the material wavenumber, the resulting wave into the material is subsonic; the wave will propagate parallel to the interface, but will be evanescent and create a near-field pressure distribution along the interface. A subsonic wave producing an evanescent pressure distribution will not propagate energy into the material. In the supersonic region, the angle of propagation is entirely real; the shift from supersonic to subsonic propagation is the shift from a real to complex angle (where the real component of the angle will always equal 90°). The critical angle, θ_{0c}, for an incident wave where the resulting wave into the material becomes subsonic is:

$$\theta_{0c} = \arcsin \frac{c_0}{c_1} . \tag{3.15}$$

For air-solid interfaces, this angle is very small; for example, for a ratio of wave speeds $c_1/c_0 = 10$, the critical angle is 5.7 degrees. For angles greater than the critical angle, the transmitted angle into the material is complex, and the resulting normal wavenumber into the transmitted material will be imaginary.

The evanescent waves generated by complex angles increase energy propagation by decreasing the refracted real angle and allowing for wave propagation at angles higher than the critical angle. Figure 3.5 shows the change in both real and complex components of a refracted angle, θ_1, from a complex incident angle, θ_0, across an interface with $c_1/c_0 = 10$. The addition of an imaginary component to the angle eliminates the critical angle criterion. The refraction of a complex angle will asymptote towards 90°; adding only a small imaginary component to the complex angle causes significant motion away from grazing. For example, an $\Im(\theta_1)$ value of 1 causes the refracted angle at 30° to shift from grazing to 37°. However, the imaginary component increases with refraction as well; the addition of the imaginary component to the angle causes an increase in the imaginary component of the propagating angle from 1.3 (which occured at grazing) to 1.8.
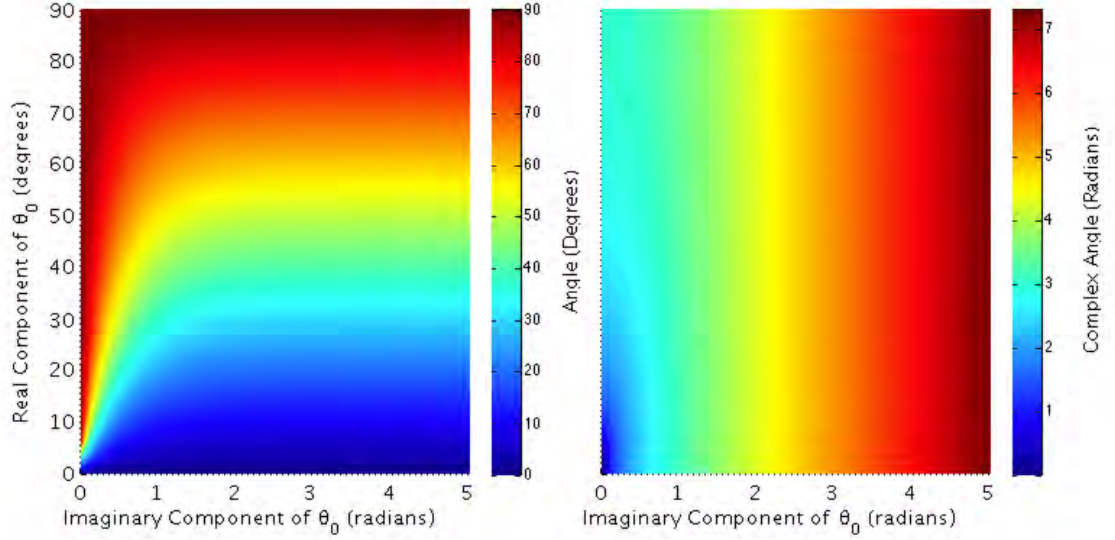
Figure 3.5. Complex angle refraction of the transmitted wave $\tilde{\theta}_1 = \theta_r - j\theta_i$ across an interface with $c_1/c_0 = 10$. The left plot is $\Re(\arcsin(c_1/c_0 \sin \tilde{\theta}_0))$, while the right plot is $\Im(c_1/c_0 \arcsin(\sin \tilde{\theta}_0))$.

Even with a reduction in the refracted angle due to the use of complex incident angles, the increase of imaginary components will create additional decay in the propagating wave. By calculating the energy decay with distance across the interface, we can more accurately see the effects of the evanescent wave. The calculation of intensity would include both the pressure transmission coefficient and the effect of the complex angle in wave transmission.

The calculated intensity transmission coefficients are functions of the material impedances and incoming angles of the wavetypes in the system. Considering both of these factors will yield a full accounting of the effects of evanescent waves on energy transmission across an interface.

3.2.2 Fluid-Fluid Interface

We will begin by considering a fluid-fluid interface, since it is a simpler system with only one wavetype in each material. Our example system will be an air-fluid interface where the theoretical fluid has speed of sound $c_1 = 10c_0$ and density $\rho_1 = 1000\rho_0$.

At the fluid-fluid interface there are three waves to consider: the incident wave incoming at an angle $\tilde{\theta}_0$ of unit amplitude, the reflected wave in the incident fluid at an angle $-\tilde{\theta}_0$ with amplitude R, and the transmitted wave at angle $\tilde{\theta}_1$, computed from Snell's law as a function of the incoming angle and two fluids' speed of sound, and amplitude T. For an interface in the $x - y$ plane with a normal $\hat{z}$, the material states across the interface remain constant:

$$p_1(0) = p_0(0) \; ; \; v_{1z}(0) = v_{0z} \; . \tag{3.16}$$

Considering the incident, reflected, and transmitted waves in these formulations yields:

$$T = 1 + R \; ; \; \frac{T}{Z_1/\cos(\tilde{\theta}_1)} = \frac{R - 1}{Z_0/\cos(\tilde{\theta}_0)} \; , \tag{3.17}$$

and these two boundary conditions can be used to solve for the transmitted wave amplitude T:

$$T = \frac{2Z_1/\cos(\tilde{\theta}_1)}{Z_1/\cos(\tilde{\theta}_1) + Z_0/\cos(\tilde{\theta}_0)} \; . \tag{3.18}$$

Note that each additive term in the equation is equivalent to the normal impedance in the fluids. The amplitude of T with incident angle in a classical system, as shown in Figure 3.6, is nearly 2 for all incident angles due to the dominance of the impedance of water. Above the critical angle, T is equal to 2, but the transmitted angle will be imaginary and no energy will propagate. At incident angles extremely close to grazing, the influence of the incident impedance will reduce the transmission coefficient; however, there is still no energy propagation into the material.
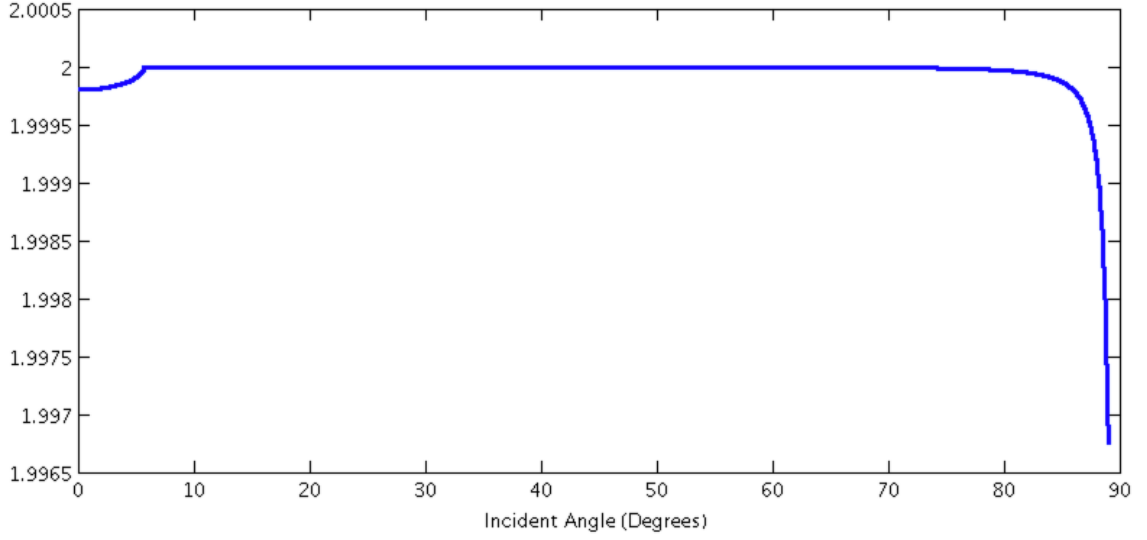
Figure 3.6. Pressure transmission coefficient T for plane wave propagation into a fluid.

For complex θ_0, the pressure transmission coefficient will decrease with increasing imaginary angle component. A plot of the transmitted pressure amplitude is shown in Figure 3.7, which shows that the maximum values of transmission occur at real, grazing angles.

The pressure transmission coefficient does not account for the resulting velocity of the transmitted wave, which is necessary to discern the energy propagating into the system. Development of an intensity transmission coefficient, which will properly account for the energy transmitting across the interface due to both the pressure transmission coefficient and the complex angle of propagation, is therefore necessary to compute the sound power transmitted.

The intensity of a wave is computed from the pressure and velocity at that point:

$$\vec{I} = \frac{1}{2}\Re(p(\vec{x})\vec{v}^*(\vec{x})) \, , \tag{3.19}$$
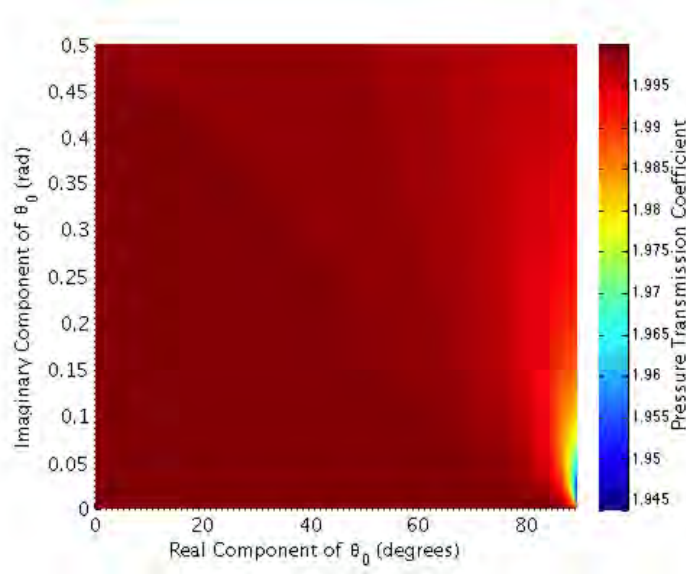
Figure 3.7. Pressure transmission coefficient T for fluid-fluid system.

where $\vec{v^*}$ is the complex conjugate of the velocity. This relationship accounts for both the pressure and velocity amplitudes (which are related by the impedance) as well as the phase relationship between the pressure and velocity.

The velocity in the $\hat{z}$ direction of a plane wave is given by Equation 3.7; for a plane wave with the pressure distribution shown in Equation 3.1 (note that the wavenumber vector has been expanded to it's component terms), the resulting velocity is:

$$v_z = \frac{k_z}{\omega \rho} p \ , \tag{3.20}$$

and the resulting general equation for intensity in the plane wave normal to the surface is:

$$I_z = \frac{1}{2} \Re \left(\frac{k_z}{\omega \rho} pp^* \right) \ . \tag{3.21}$$

For a real incident angle, the intensity equation simplifies to the ratio of the mean square pressure over the material impedance:

$$I_z = \frac{|A|^2}{2\rho c} \cos\theta \; ; \; \theta = \Re(\theta) \; , \tag{3.22}$$

where $|A|^2$ is the magnitude squared of the complex amplitude, $|A|^2 = AA^*$. For subsonic wave propagation (a complex angle with a 90 degree real component), the wavenumber, k_z, in the $\hat{z}$ direction will be purely imaginary, and the intensity in the wave will be equal to zero. For a complex angle of incidence, $\tilde{\theta}_0 = \theta_{0r} + j\theta_{0i}$, the resulting intensity in the wave will be:

$$I_z = \frac{|A|^2 \Re(k_z)}{2\omega\rho} e^{2\Im(k_z z - 2k_x x)} \; . \tag{3.23}$$

The intensity transmission coefficient across an interface in the $\hat{z}$ direction, I_T, resulting from a unit incident pressure amplitude is:

$$I_T = \frac{I_1(z_1)}{I_0(z_0)} = \frac{|T|^2 \Re(k_{1z})\rho_0}{\Re(k_{0z})\rho_1} e^{2\Im(k_{0z} z_0 - k_{1z} z_1)} \; , \tag{3.24}$$

and for the intensity transmission directly across the interface, $z_0 = z_1 = 0$, the intensity transmission coefficient can be simplified to:

$$I_T = \frac{I_1(0)}{I_0(0)} = \frac{|T|^2 \Im(k_{1z})\rho_0}{\Im(k_{0z})\rho_1} \; , \tag{3.25}$$

with the transmission coefficient TC in decibels equal to:

$$TC = 10\log(I_T) \; , \tag{3.26}$$

which is the inverse of the transmission loss.

The inclusion of an imaginary angle component become beneficial when considering intensity transmission across the interface. The intensity transmission coefficient as a function of real and complex angle is plotted in Figure 3.8. The plot shows increased intensity transmission with increasing imaginary angle component; for example, an increase in imaginary angle component from 0.001 to 0.3 causes 23.6 dB of increase to the transmission coefficient at a 30 degree incident angle.
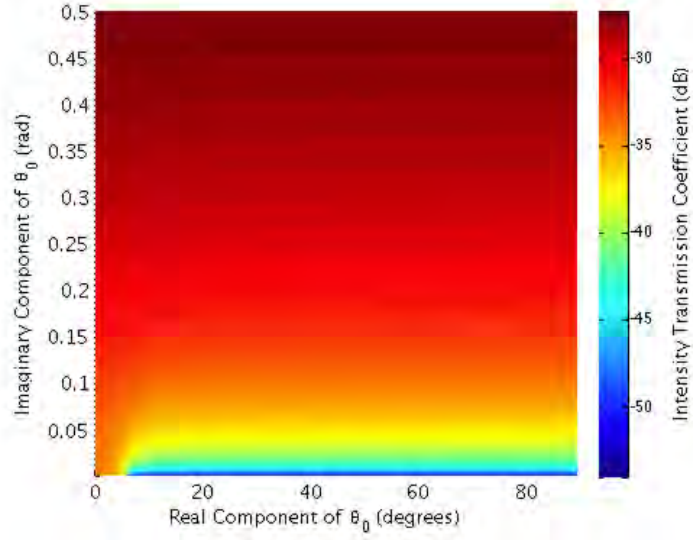
Figure 3.8. Intensity transmission coefficient TC variation for a fluid-fluid system with a complex angle of incidence.

3.2.3 Fluid-Solid Interface

Wave propagation at a fluid-solid interface will generate a reflected pressure wave in the incident fluid and transmitted shear and pressure waves in the transmitted solid, with the shear amplitude B and a wavenumber κ. At the fluid-solid material interface, pressure and velocity are conserved across the boundary. Because a fluid wave cannot sustain shear, the shear stress on the surface is zero. Note that this does not mean the shear wave amplitude is zero; the compressional wave will induce a shear stress on the surface when propagating at a non-normal angle and the shear wave stress is generated to cancel out this surface stress. The three state relationships at the interface are:

$$p_0(0) = -\sigma_z(0) \ , \ \ 0 = \sigma_x(0) \ , \ \ v_{0z}(0) = v_z(0) \ . \tag{3.27}$$

For an incident wave with unit pressure amplitude, the resulting transmitted pressure amplitudes into the material (as calculated by Brekhoshovikh [3]) is proportional to the angles of propagation and the normal impedances at the surface:

$$Z_z = \frac{\rho c}{\cos(\theta_0)} \ ; \ Z_{1z} = \frac{\rho_1 c_1}{\cos(\theta_1)} \ ; \ Z_{1x} = \frac{\rho_1 b_1}{\cos(\gamma_1)} \ . \tag{3.28}$$

For a unit amplitude incident wave, the amplitude of the normal stress propagating into the material is the transmission coefficient T_L:

$$T_L = \frac{2Z_{1z} \cos(2\gamma_1)}{Z_{1z} \cos^2(2\gamma_1) + Z_{1x} \sin^2(2\gamma_1) + Z_z} \ , \tag{3.29}$$

while the resulting shear wave transmission coefficient T_S is:

$$T_S = -\frac{2Z_{1x} \sin(2\gamma_1)}{Z_{1z} \cos^2(2\gamma_1) + Z_{1x} \sin^2(2\gamma_1) + Z_z} \ . \tag{3.30}$$

The pressure transmission coefficient for a real angle has several distinct characteristics due to the interplay of the compressional and shear waves. Figure 3.9 shows the pressure transmission coefficient in logarithmic form ($TC = 20 \log(T_{L,S})$ for an interface with $c_1/c_0 = 10$, $b_1/c_0 = 7$ and density ratio $\rho_1/\rho_0 = 1000$. There are several peaks in the values that would appear to indicate avenues of energy transmission. The small spike in T_L at 5.7 degrees is due to the critical angle of the compressional wave,which causes a maxima in the numerator of T_L. The dip at 5.8 degrees is caused by a minima in the numerator when $cos(2\gamma_1)$ is equal to zero. The critical angle for the shear wave is 8.2 degrees, where there is a discontinuity in both the T_L and T_S value. The peak near 9.4 degrees is due to impedance cancellation (which occurs after the critical angle and γ_1 is complex) between the transmitted pressure and shear wave, minimizing the denominator common to both terms. However, most of these features are at angles beyond the critical angles for both the compressional and shear waves, and there is very small velocity into the material.

Intensity in the solid is calculated in a way similar to Equation 3.23, with the appropriate wave amplitude and wavenumber in place for the compressional or shear wave:

$$I_{L,z} = \frac{|A|^2 \Re(k_z)}{2\omega\rho} e^{2\Im(k_z z - 2k_x x)} \ . \tag{3.31}$$
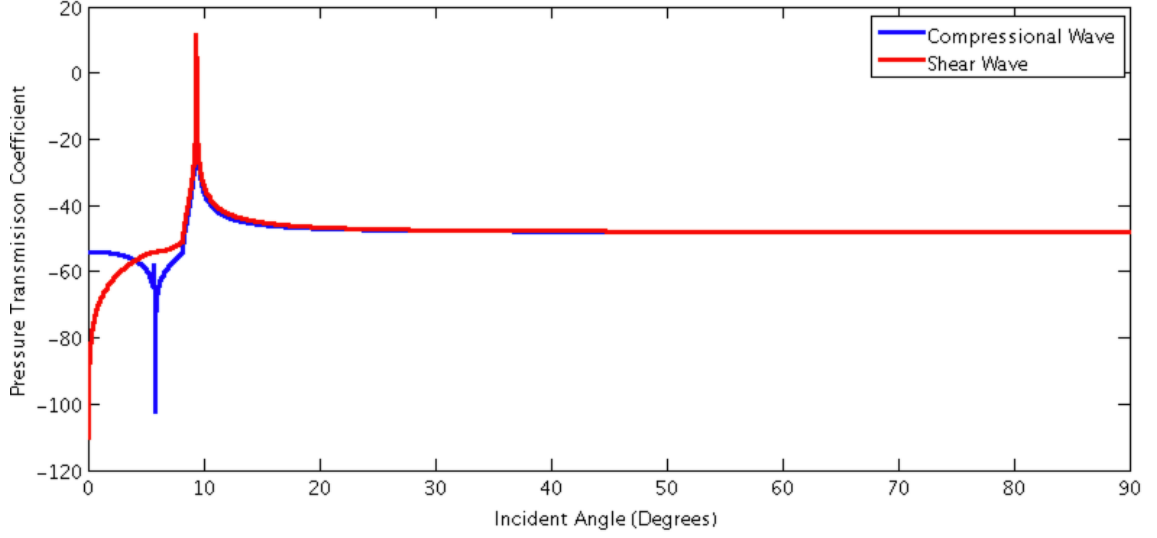
Figure 3.9. Transmission coefficients, $20\log(T_L)$ and $20\log(T_S)$, for a system with wave speed ratio $c_1/c_0 = 10$ and density ratio $\rho_1/\rho_0 = 1000$.

$$I_{S,z} = \frac{|B|^2 \Re(\kappa_z)}{2\omega\rho} e^{2\Im(\kappa_z z - 2\kappa_x x)} \ . \tag{3.32}$$

Because intensity is a measure of energy, it should balance across the interface: i.e., the total power incident on the surface minus the intensity reflected above the surface should equal the intensity transmitted below the surface in longitudinal and shear waves. The model above can be verified by accounting for this intensity. The magnitude of the reflected wave component, R, is calculated as:

$$R = \frac{Z_{1z}\cos^2(2\gamma_1) + Z_{1x}\sin^2(2\gamma_1) - Z_z}{Z_{1z}\cos^2(2\gamma_1) + Z_{1x}\sin^2(2\gamma_1) + Z_z} \ . \tag{3.33}$$

The reflected intensity travels away from the interface; therefore, the net intensity above the interface will be the intensity of the incident wave minus the intensity of the reflected wave. Figure 3.10 shows the total intensity above and below the fluid interface for both a classical and evanescent wave. That the intensity is the same

above and below the interface across the incident angle range serves as verification that the model is properly accounting for energy in the system.
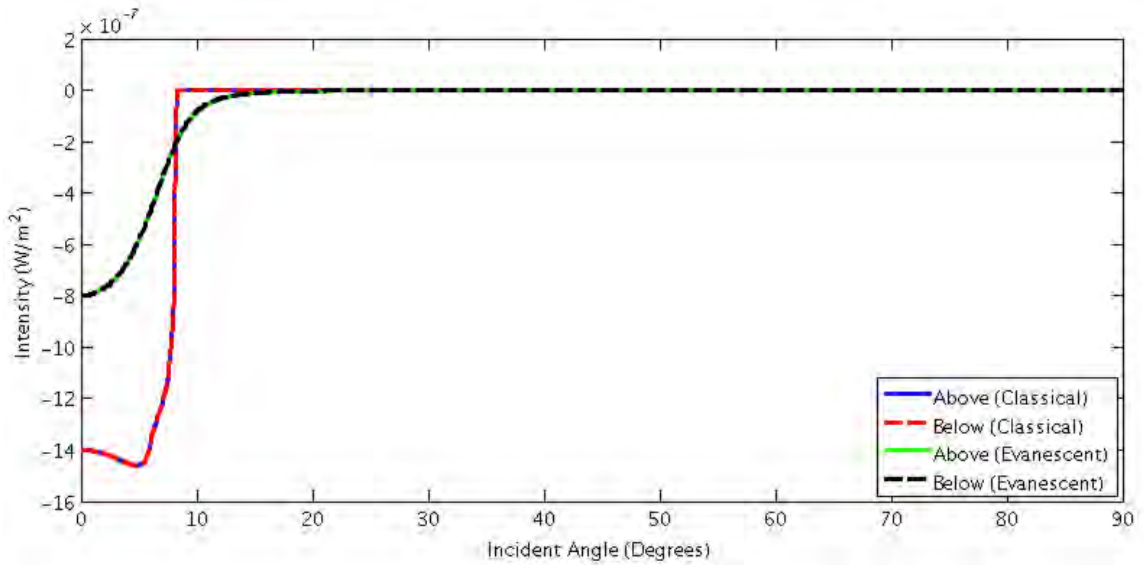
Figure 3.10. Net normal intensity above and below the fluid-solid interface, with the incident and reflected waves contributing to the intensity above the interface and the longitudinal and shear transmitted waves contributing to energy below the interface.

The intensity transmission coefficient across the material interface used previously ($c_1/c_0 = 10$, $b_1/c_0 = 7$ and $\rho_1/\rho_0 = 1000$) is shown below in Figure 3.11. This intensity transmission is that immediately across the interface, and will not represent the effect of the evanescent component penetrating further into the material. The lowest complex incidence angle value shown is 0.001, as a purely real value will be equal to zero beyond the critical angle. The use of complex angles expands the transmission peaks (such as those at 10 Hz) while allowing for energy transmission across the entire spectrum. While the complex angle does not provide a substantial benefit below the critical frequency (the warm area to the far left of the plot), expansion of the realm of intensity transmission beyond the near-normal angles will allow for more varied sources of excitation.
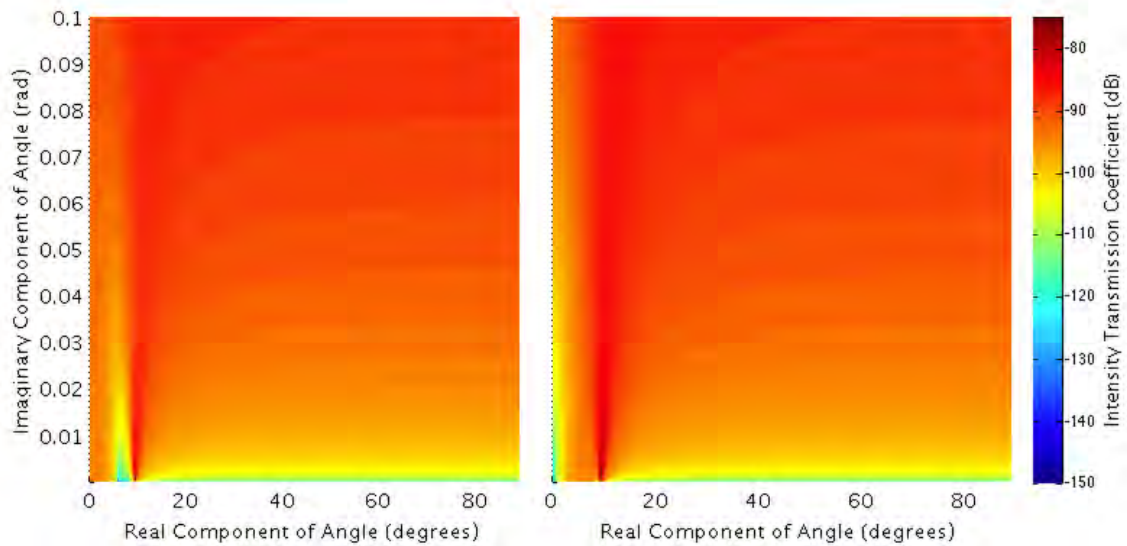
Figure 3.11. Intensity transmission coefficients at 1000 Hertz across the interface for the compressional (left) and shear (right) waves due to a complex angle of the incident wave.

The intensity transmission coefficient calculated at a depth of one meter below the material interface is shown in Figure 3.12. This transmission coefficient shows the negative effects associated with the imaginary angle of refraction. There is significant intensity lost into the system, particularly above the critical angle, and options for ideal intensity transmission are limited to smaller angles. However, there is still transmission above the critical angle, and the pressure transmission peak near 10 degrees provides significant transmission.

The use of complex angles to generate evanescent waves has been shown, in theory, to increase energy transmission across the air-solid interface. While using complex angles introduces additional imaginary components to the refracted angle of the propagating wave, the change in real angle of propagation will cause energy to propagate further into the material. An approach for intensity propagation taking into account the pressure transmission and the resulting intensity due to the angle of transmission must be formulated to allow for a means to see the effect of complex angles on energy transmission across the interface.
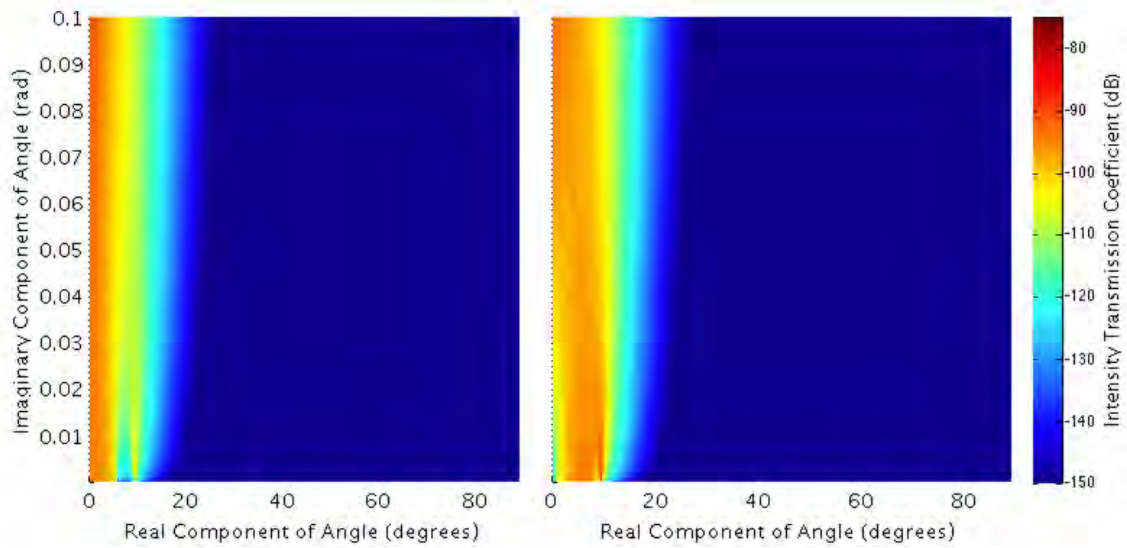
Figure 3.12. Intensity transmission coefficients for a depth of 1 meter into the material for the compressional and shear waves due to complex angles.

The use of complex angles can increase intensity transmission at a high-impedance interface, particularly beyond the critical angle of sound transmission. By using the evanescent components of a monopole, we can show that these theoretical considerations can be seen in experimental verification.

3.3   The Monopole as an Evanescent Wave Source

Evanescent pressure distributions with well-defined characteristics are not generated by typical sound sources. While some sources may generate evanescent waves, they will be unique to the source and difficult to control. Therefore, it is helpful to explore evanescent wave properties of a simple source, the acoustic monopole, to provide a basis for experimental exploration of the theory of evanescent wave transmission.

3.3.1 Theory

An acoustic monopole is a fundamental source, in which pressure generation from a single point radiates equally in all directions. The pressure at a distance R from the source is equal to:

$$p = \frac{e^{jk_0 R}}{R} , \qquad (3.34)$$

which shows a $1/R$ decay in pressure over distance. Figure 3.13 shows the pressure of a monopole in space and along the radius from the monopole.
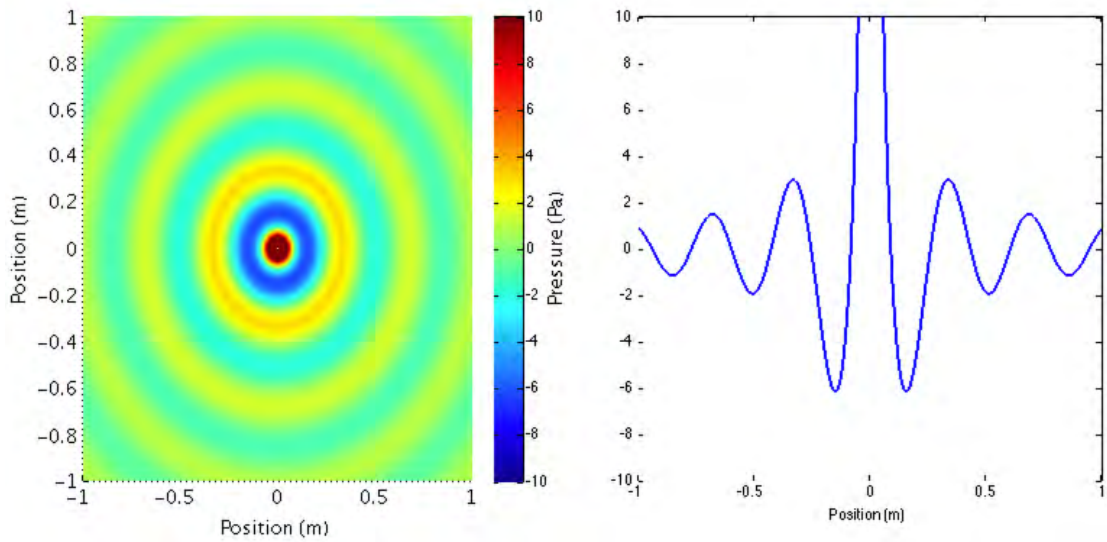
Figure 3.13. Monopole pressure distribution in the plane containing the monopole, showing the real component of the pressure for a 1000 Hz monopole in air (a wavenumber of 18.3 radians per meter), in two-dimensional (left) and in one-dimensional space (right) along the radius. The maximum pressure peak at $r = 0$ has been cut off at 10 Pa to show detail.

When the radiated pressure distribution is projected onto a plane offset at a distance z_0, the resulting distance from the origin R will be:

$$R = \sqrt{x^2 + y^2 + z_0^2} , \qquad (3.35)$$

and the radius will increase from a minimum value of z_0 along the plane. A larger z_0 value will cause a reduced increase in R per length along the plane, which will reduce the amount of decay per distance in the trace pressure distribution. Furthermore, the trace wavelength along the plane will decrease to the material wavelength $2\pi/k$ as R increases; a higher z_0 value will cause less variation in the trace wavelength. The result of the decrease in decay rate and trace wavelength will cause the monopole to approximate a plane wave. Sample trace pressure distributions for both a small and large standoff distance are shown in Figure 3.14. The 10 centimeter standoff has significant decay near the origin and shorter wavelengths, while the 2 meter standoff has less decay and the initial wavelengths are closer to the material wavelength.
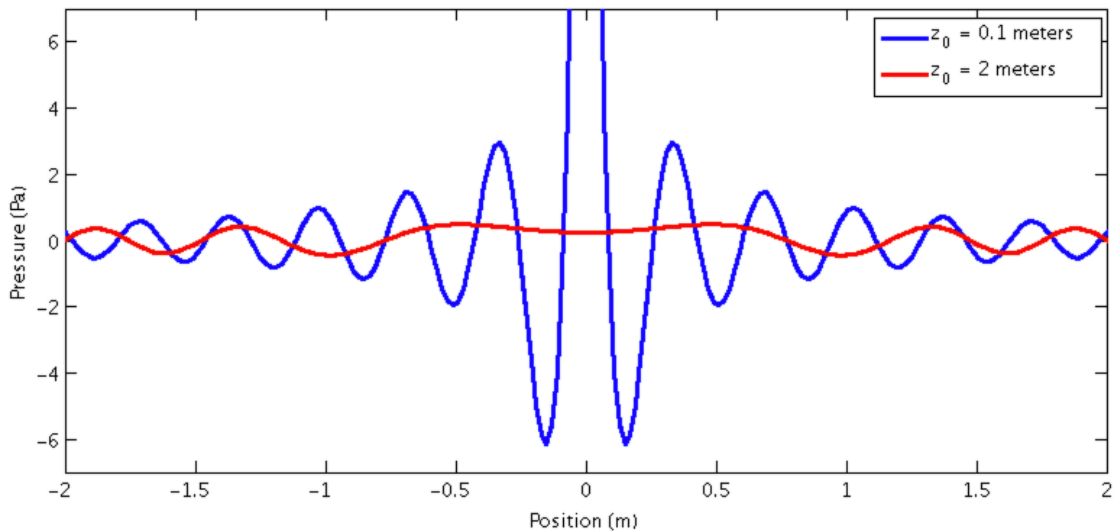
Figure 3.14.   Trace pressure distributions (real component of pressure) of a monopole at a z_0 distance of 10 and 200 centimeters for a wavenumber of 18.3 radians per meter. The shorter standoff distance displays similar properties to an evanescent wave.

Due to the $1/R$ decay (compared to an exponential decay) and the change in wavelength, a monopole pressure distribution is not equivalent to an evanescent plane wave. However, it does display evanescent properties.

The wavenumber spectrum, which can be calculated by the Fourier transform of the spatial pressure distribution:

$$P(k) = \mathcal{F}(p(x));,$$ (3.36)

of a monopole's trace pressure distribution consists of distinct regions of evanescent and non-evanescent waves. The energy in the wavenumber region below k_0 is supersonic, while the energy above k_0 is subsonic and generates evanescent waves. Figure 3.15 shows the wavenumber spectrum for the two pressure distributions shown in Figure 3.14. With increasing standoff distance, the resulting WN spectra has less energy in the evanescent region. Figure 3.16 shows Q, the ratio of evanescent component to non-evanescent component in the trace pressure distribution as a function of normalized standoff distance:

$$Q(kz_0) = \frac{\int_{k_0}^{\infty} P^2(k, z_0)}{\int_0^{k_0} P^2(k, z_0)}$$ (3.37)

A monopole produces significant evanescent components, and these components can be decreased by increasing the standoff distance between the monopole and the incident plane. Using these properties of the monopole, the effects of evanescent waves on transmission of energy into the plate can be seen.

3.4 Experimental Measurement of Monopole Evanescent Components

The monopole provides a source of evanescent waves, which may propagate additional energy into higher impedance materials. The pressure distribution of a simulated monopole source was inspected for the presence of evanescent waves using acoustical holography. Once the evanescent waves were verified, the distribution was used incident upon a panel to see the effects of the evanescent wave transmission into the solid material.
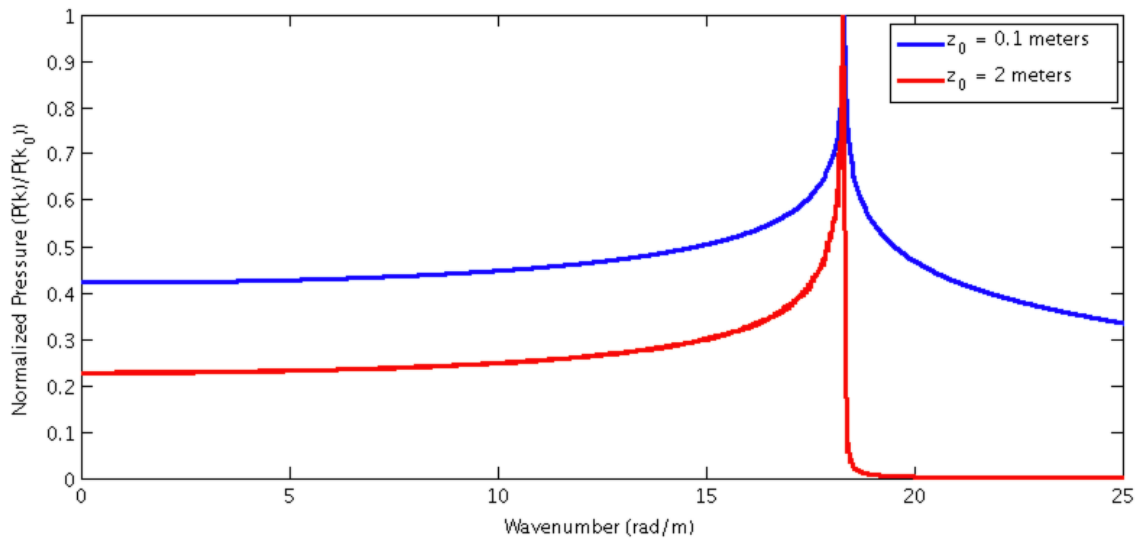
Figure 3.15. Wavenumber spectra of the trace pressure distribution from a monopole radiating at 100 Hz for standoff distances of 10 and 200 centimeters. The peak in the plot is at k_0; energy above this peak is subsonic, with the closer standoff having more subsonic energy than the further standoff.

3.4.1 Test Setup and Methodology

The panel used for testing was a 9.4 millimeter (nominally 0.375 inch) thick poly-carbonate panel. The panel was 60 centimeters long by 50 centimeters high, with holes drilled in each corner at 12.7 millimeters (0.5 inch) from the edges. These holes were used to suspend the plate in a 113 centimeter square wooden frame. This mounting method was used to minimize the effects of mounting on the vibration of the plate, as well as to minimize reflections from the mounting. The plate was sanded on one side to produce an opaque surface for improved laser vibrometer focusing and measurement.

Vibration properties for the plate were measured by exciting the panel with a PCB 712A02 stack actuator equipped with a 100 gram add-on mass. The resulting force into the system was measured with a PCB 208A02 force transducer mounted between the actuator and the panel surface, and was recorded using the data acqui-
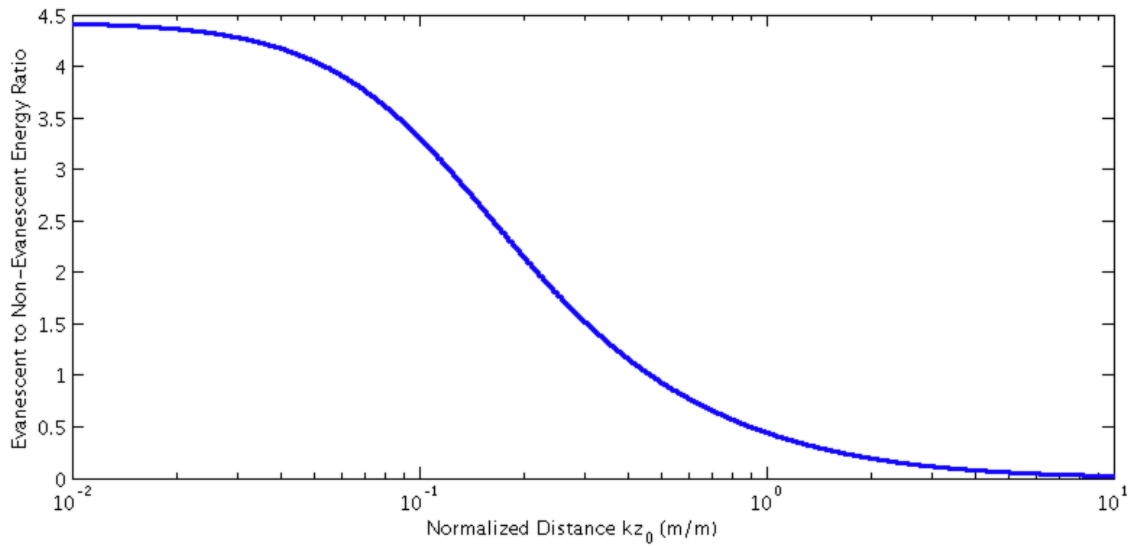
Figure 3.16.   Ratio Q of evanescent to subsonic to supersonic components in the trace pressure distribution of a monopole incident on a plane as a function of normalized monopole standoff distance. The increase in standoff causes a reduction in evanescent energy.

sition system from the laser vibrometer. This actuactor-transducer arrangement was mounted in the corner of the panel during vibration measurements to classify modes and wavetypes in the panel.

Vibration was measured using the Polytec PSV 400 scanning laser vibrometer and data acquisition system. The vibrometer allows for automated scanning of points along a surface. Vibration was recorded from 0 to 4 kilohertz, along with the output from either the force transducer or microphone near the source (depending on the test).

The vibrometer data acquisition, which was used for all vibration measurements, measured a bandwidth of 4,000 Hertz at 2.5 Hz resolution, with 50 averages per point. A total of 221 points were measured, constituting 13 rows and 17 columns across a 54 by 42 centimeter rectangle on the panel. The resulting measurement parameters allow for a wavenumber resolution of 11.63 radians per meter (rad/m) from -69.81 rad/m to 58.18 rad/m in the horizontal direction and a resolution of 15.14 rad/m

from -121.12 to 105.98 rad/m in the vertical direction. More information about wavenumber decomposition and analysis can be found in Section 5.2.

The monopole pressure distribution was generated using the Herrick Laboratories half-monopole source. This source is a 1 meter long, 2.54 cm (1 inch) diameter copper-lined PVC pipe attached to a CIE PD30T 30W compression driver with a 2.54 cm (1 inch) speaker diameter. The length of PVC pipe ensures plane wave propagation in the tube, that, when radiating from the open end of the pipe, produces a near-monopole-like pressure distribution in the hemispherical space centered at the pipe opening. The validity of the resulting pressure distribution will be discussed in the following section. While this source will produce significant harmonics at the half-wavelength frequencies of the pipe, it is suitable for single-frequency analysis. The source was driven using a General Radio 1381 Random-Noise Generator at 5 kHz and a QSC 1100 amplifier.

Measurement of sound radiation from the half-monopole source was performed using a Brüel and Kjær 4189 microphone placed immediately behind the pipe opening, approximately 2 centimeters from the surface. While this location is less-than-ideal for measuring the output spectra of the monopole, it was chosen so as not interfere with the radiation pattern. Additional testing showed that the spectra obtained from this location matched closely with the spectra obtained from the pipe opening. The microphone was connected to a Brüel and Kjær 2169 preamp and 5935 power supply, and into the data acquisition system for the vibrometer.

For classification of the monopole's sound radiation, the pressure distribution was measured with a 64 microphone holography array, consisting of TMS T130C21 ICP microphones in an 8 by 8 square pattern, with each microphone separated from its neighbors by 10 centimeters. The array provides wavenumber resolution of 8.97 radians per meter from -35.90 rad/m to 26.93 rad/m. In air, 35.9 radians per meter occurs at 1,960 Hertz; the array should provide sufficient range to properly visualize wavenumber spectra at frequencies below that. The array output was recorded using

a VXI data acquisition system with custom MATLAB software for measurement and analysis.

Testing was performed at distances between 35 and 145 millimeters from microphone number 43, located in the 6th row (from the top) and 3rd column (from the left) of the array. The source was measured off-center to allow for additional distance to measure the decay in the sound field; a centered microphone would not have the same range of distance data. A schematic of the setup is shown in Figure 3.17.
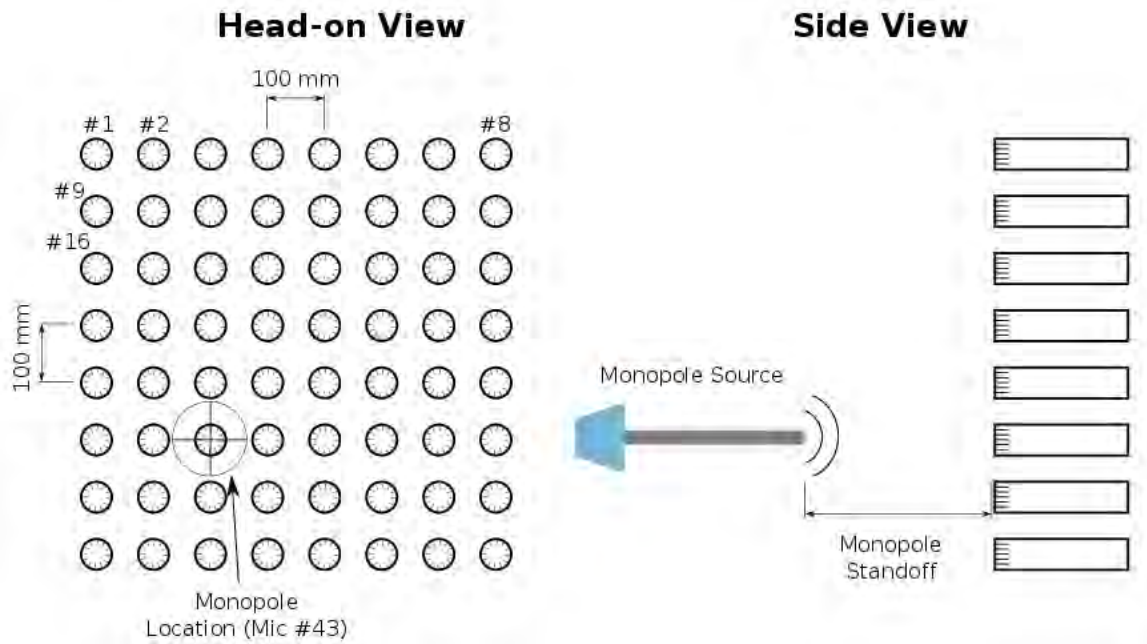
Figure 3.17. Setup and geometry for the monopole pressure radiation using the holography array.

A schematic of the setup for measuring acoustical excitation of the panel is shown in Figure 3.18, and a photo of the experimental setup is shown in Figure 3.19. The monopole was positioned at the center of the panel and tested at various distances from 2.2 centimeters to 20.2 centimeters. The resulting vibration was recorded using the vibrometer, and the resulting sound propagation was measured using the microphones.
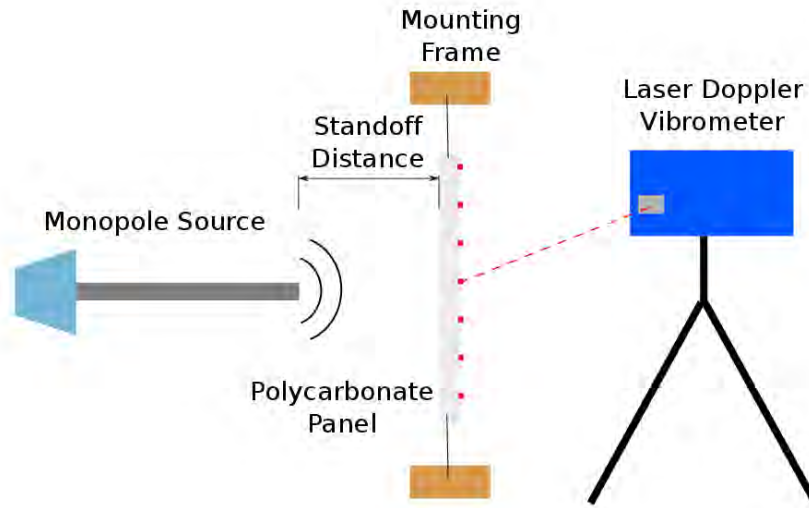
Figure 3.18. Setup for panel excitation from a monopole. The monopole produces a pressure distribution on the panel, and the resulting vibration is measured using the laser vibrometer.

3.4.2 Results

For the purposes of brevity and clarity, all results will be presented at 1,000 Hertz. This frequency is appropriate because it does not correspond to a mode of vibration in the plate, and is representative of many other regions of plate vibration.

Two "slices" of the wavenumber-frequency data, at the center of the horizontal (left) and vertical (right) wavenumber domains, are shown in Figure 3.20. The vibration of the plate is dominated by a dispersive wave with a wave speed of approximately 200 m/s at 1000 Hz; this wave will be subsonic in air. The wavenumber spectrum of vibration is shown in Figure 3.21, showing the concentration of energy in an oval with major axes at 45.42 and 34.91 radians/meter (although the precise locations of these peaks are within the resolution of the wavenumber measurement).
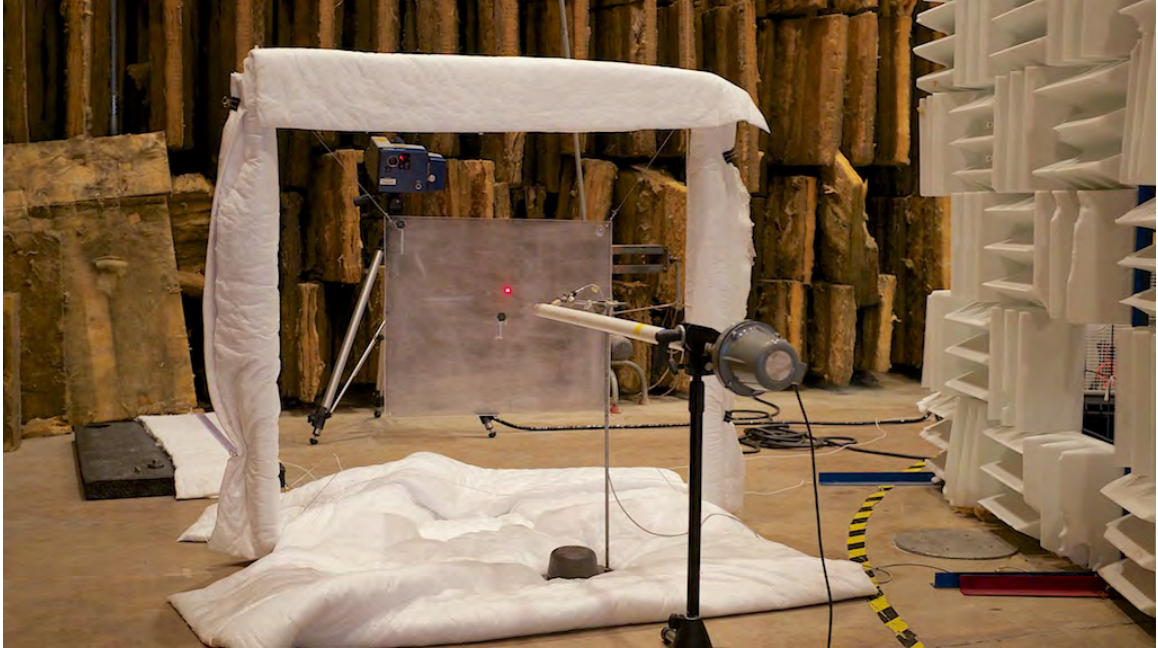
Figure 3.19. Experimental setup for monopole-excited panel. The monopole source is the forefront object, with the driver (light blue) closest to the camera. The panel is mounted in the wooden frame; the white surrounding material is Thinsulate, which is wrapped around the frame to reduce reflections from the frame. The experiment took place in the hemianechoic chamber, which reduces reflections from other sources.

The pressure spectrum of the monopole shows a $1/R$ decay with distance (from the monopole location), as seen by comparing the pressure at each measured point as a function of the radius in Figure 3.22. The wavenumber spectrum of the monopole pressure, shown in Figure 3.23 shows energy in a circle with radius of approximately 18 radians per meter, coinciding with theory. In addition, the pressure and intensity from the monopole decay with the radius (from the monopole) and radius squared, respectively.

The ratio of evanescent component to non-evanescent component (similar to what is shown in Figure 3.16 for Equation 3.37) for the half-monopole source is shown in Figure 3.24. Similar to a theoretical monopole, the half-monopole source shows a reduction in evanescent component with increasing distance from the plane.
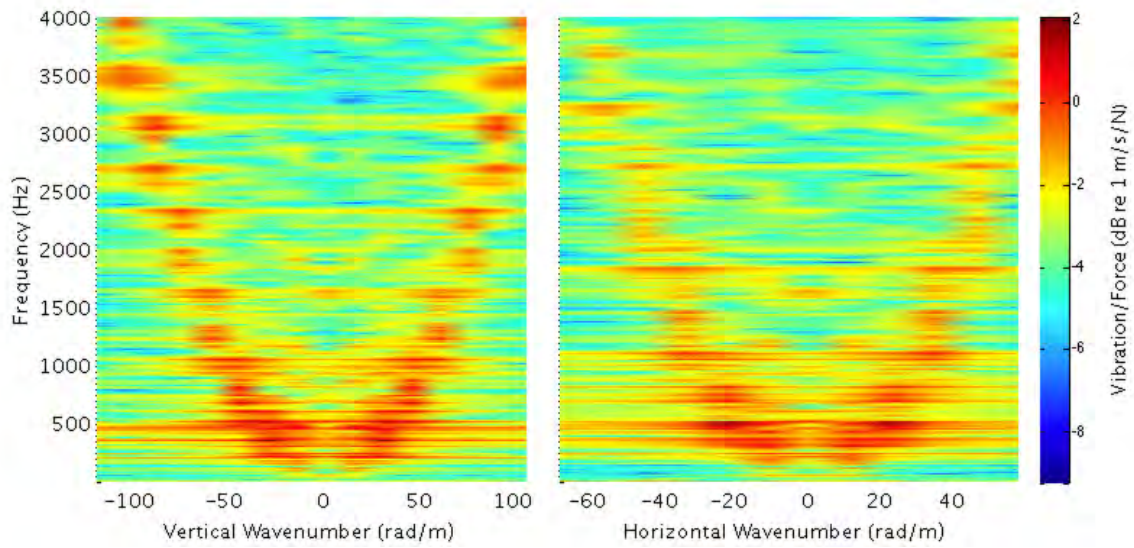
Figure 3.20. Wavenumber-frequency plots of panel vibration at $k_x = 0$ (left) and $k_y = 0$ (right).
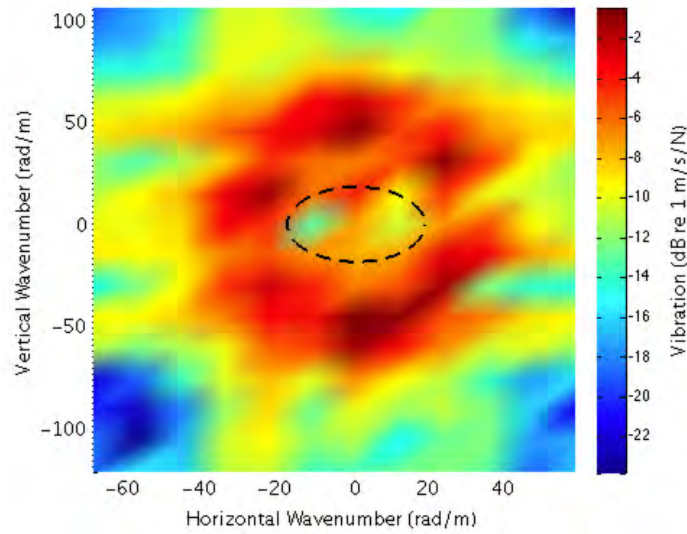
Figure 3.21. Two-dimensional wavenumber spectrum of panel vibration at 1000 Hz. Note that the scales for the k_x and k_y dimensions are not equal. Note that the x and y axes are not equal.

The half-monopole source is therefore thought to be a resonable approximation of a monopole for testing. While the evanescent componenets displayed by the
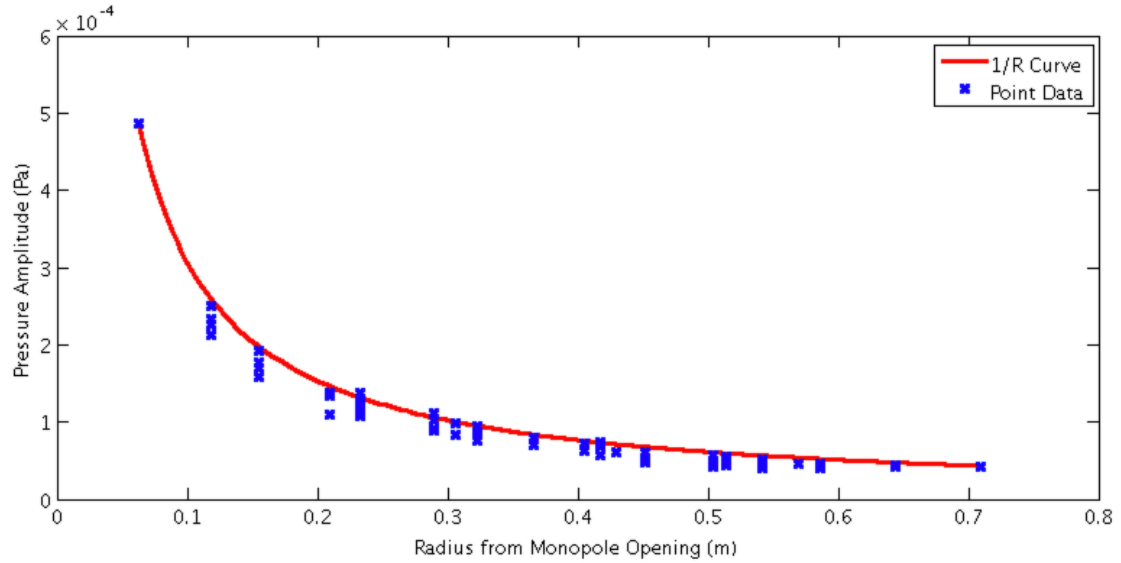
Figure 3.22. Monopole pressure amplitude at the distances measured by the holography array. The 1/R decay in pressure is clearly evident.

monopole cannot be represent a broad spectrum of complex angle components rather than a single plane wave, they exhibit similar decay over distance, properties that allow them to be an experimental stand-in for evanescent plane waves.

The resulting panel vibration due to acoustic excitation from the monopole source is shown in Figure 3.25 for standoff distances of 22 and 202 millimeters. The 22 millimeter standoff shows significant vibration in wavenumber components above the material wavenumber in air. While supersonic components in air would be able to excite the panel vibration due to the presence of the slow flexural waves, such excitation would be seen across a range of standoff distances, as the energy in the supersonic domain does not decay as dramatically. However, the 202 millimeter standoff does not exhibit these same characteristics. This is indicative of evanescent wave propagation into the material.
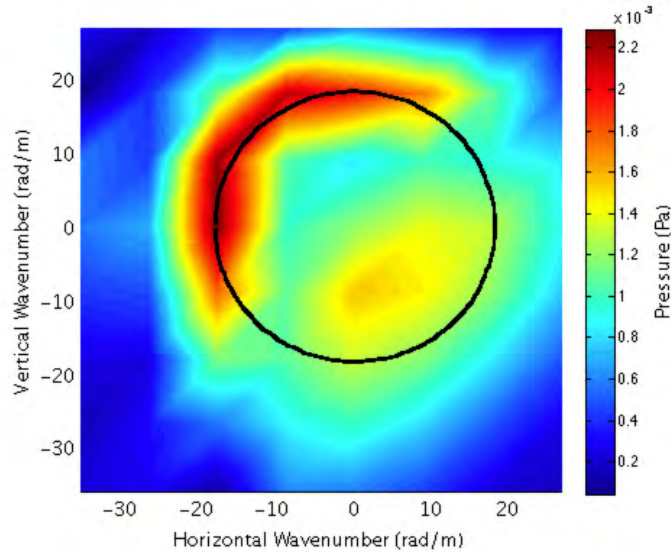
Figure 3.23.   Wavenumber spectrum of the monopole sound radiation at 63 millimeter offset. The assymetric nature of the wavenumber spectrum is due to the offset measurement of sound pressure radiation. The black circle indicates the material wavenumber in air of 18.3 rad/m; the wavenumber spectrum is clearly highest in this wavenumber bin.

3.5   Conclusions

The use of evanescent waves has been shown, in theory, to increase energy transmission across the air-solid interface. By representing evanescent waves using complex angles, these waves can be input into classical formulations for energy transmission across the air-fluid and air-solid interfaces. The evanescent wave will overcome the critical angle that typically limits energy propagation, and allow for transmission across a wider range of angles.

Beyond the critical angle, a plane wave's intensity does not propagate into the system, existing only as a surface pressure that rapidly decays. The use of the evanescent angle does not increase the pressure transmission coefficient, but reduces the refracted angle, allowing for propagation of energy into the system. The use of complex angles introduces an imaginary component to the refracted angle of the propagating
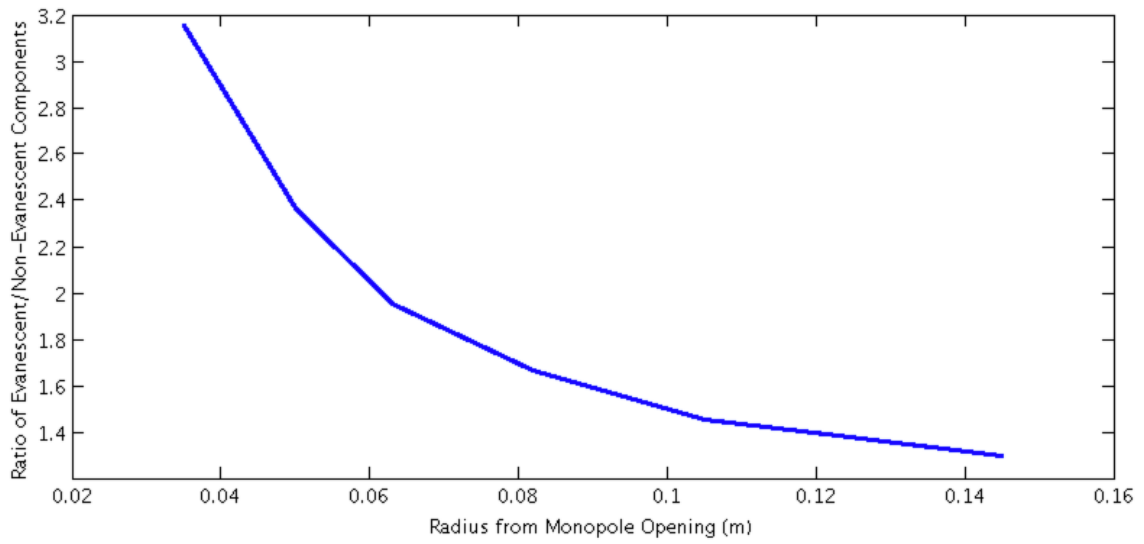
Figure 3.24. Measured ratio of evanescent to non-evanescent components for the monopole source at 1000 Hertz.
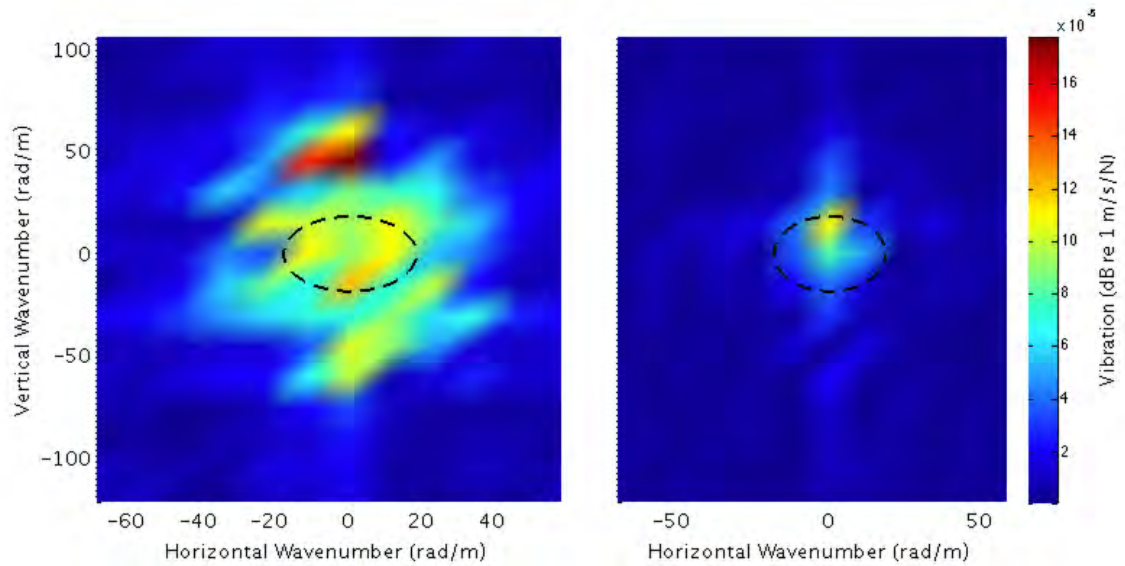
Figure 3.25. Wavenumber spectrum of monopole excitation for stand-off distances of 22 millimeters (left) and 202 millimeters (right). The decreasing energy in the system, particularly at subsonic wavenumbers (which is demarcated by the dashed black line), shows the effectiveness of

wave; this will cause additional decay into the system which should be accounted for by measuring the intensity propagating into the system. An approach for intensity propagation taking into account the pressure transmission and the resulting intensity due to the angle of transmission must be formulated to allow for a means to see the effect of complex angles on energy transmission across the interface.

A monopole's trace pressure distribution along a surface has significant evanescent wave components; these components decrease with standoff distance between the monopole and the plane (relative to the supersonic components typically seen). However, a monopole source used to excite a high-impedance solid object will exhibit these evanescent components in the resulting vibration of the solid object.

CHAPTER 4. GENERATION OF NEAR-FIELD PRESSURE DISTRIBUTIONS

The use of plane waves is convenient in theoretical formulations of fluid-solid transmission because their trace pressure along a plane surface is a steady-state, fixed-wavelength acoustical interaction. An evanescent wave, formed by incorporating an imaginary component into the angle of incidence, will have a fixed decay that can be used in theoretical formulations.

However, plane waves are impossible to generate from a simple sound source in a free-field environment. While plane waves can be generated in confined spaces such as tubes, or in certain conditions such as locally in the far-field of a monopole, such cases are limited by the geometries and frequencies involved in the system. In order to utilize typical sound sources in general cases, we need to be able to generate plane waves to use as inputs to the material interface.

The focus of the work described in this chapter was on generating plane waves, particularly evanescent waves, by using simple sources in a phased array. By adapting a previous model for the least-square fit of pressure distributions, an approximate pressure distribution can be created by the phased array. An exploration of the factors affecting the generation of pressure distributions, including the incident wave parameters, source geometry, and amount of decay in evanescent waves, will be explored here.

The model developed and analyzed here is for a two-dimensional sound pressure distribution and array. While this does not provide a simulation of a true physical setup, it will provide an overview of the geometric properties of the array and characteristics of incident waves to produce pressure distributions on the surface. For a simulation used in construction of an experimental array, a three-dimensional model

should be created, which would incorporate the polar angle of the incident wave as well as a length and number of sources along the additional coordinate. However, construction of an experimental array should also take into account the possibility of additional geometries and the angular dependence of physical speakers. The model here is two-dimensional to reduce the complexity and allow for ease of analysis of the simpler parameters.

4.1 Properties of Waves and Sources

In order to approximate a plane wave incident upon a surface and maintain its relationships with a material interface, both the pressure and normal velocity of the plane wave need to be preserved in the generated pressure distribution. Accurately modeling these states, as well as the pressure generated by monopole and dipole sources, for example, will allow for the development of a model to approximate plane wave pressure distributions created by using multiple monopoles or dipoles.

4.1.1 Properties of Plane Waves

The properties of a plane wave that define the interaction at a material interface are the pressure at the interface and the velocity normal to the interface. These quantities must be constructed on the surface so as to simulate plane-wave interaction with the surface.

A plane wave incident on a surface at an angle θ has a pressure distribution in $x - z$ space of:

$$p = Ae^{jk_x x - jk_z z} \; , \tag{4.1}$$

where A is the pressure amplitude and $k_x = k\sin(\theta)$ and $k_z = k\cos(\theta)$ are the directional wavenumbers derived from the material wavenumber k. The resulting normal velocity can be derived from the pressure-velocity relationship:

$$\vec{v}_z = \frac{1}{j\omega\rho}\frac{\partial P}{\partial z}\vec{z} = -\frac{k_z}{\omega\rho}Ae^{jk_x x - jk_z z}\vec{z} = -\frac{\cos(\theta)}{c\rho}Ae^{jk_x x - jk_z z}\vec{z} \,. \tag{4.2}$$

For the purposes of our model, $z = 0$ and the variation of p and $\vec{v}_z$ will be only dependent on x.

If the trace pressure distribution is specified by a frequency and angle of incidence, the resulting normal velocity into the surface is unique to that pressure distribution. Therefore, the pressure distribution can be modeled, and the velocity should match what is expected from an incident plane wave for that pressure distribution.

4.1.2 Properties of the Acoustic Monopole

The simplest acoustical source is the monopole, a point source of acoustic pressure consisting of a dilating sphere (of diameter much smaller than a wavelength) with a volume output of Q cubic meters per second. The pressure distribution from such a monopole is:

$$p = -j\rho_0 c_0 \frac{kQ}{4\pi}\frac{e^{jkr}}{r} \,, \tag{4.3}$$

where ρ_0 and c_0 are the density and speed of sound in air, respectively, k is the wavenumber, and r is the distance between the source and the field point. The pressure therefore has solely a radial dependence, and decreases from the origin by $1/r$. The velocity resulting from a monopole is:

$$\vec{v}_r = \frac{1}{j\omega\rho}\frac{dP}{dr}\vec{r} = -j\frac{kQ}{4\pi}(1 - \frac{1}{jkr})\frac{e^{jkr}}{r}\vec{r} \,, \tag{4.4}$$

where $\vec{v}_r$ is oriented along the radial axis from the monopole. If the monopole is located above the plane, the resulting normal velocity into the plane will be $\vec{v}_z(x) = -|\vec{v}_r|\cos(\phi)\vec{z}$, where ϕ is the angle between the normal to the plane and the line between the monopole location and the point of incidence.

The trace pressure distribution along a plane surface resulting from a monopole varies significantly depending on the standoff distance between the plane surface

and the source. In the far-field where the $1/r$ decay of the sources is small, the monopole's pressure distribution looks like a non-evanescent plane wave - the trace pressure distribution has a wavelength approximately equal to the wavelength of a plane wave in air, and there is very little decay. However, in the near-field, the $1/r$ decay creates an evanescent pressure distribution, though not one that conforms to an exponential decay or that has a constant wavelength. The effective wavelength also changes along the surface, becoming shorter with increasing distance from the source. As a result, a monopole outputs a spectrum of wavelengths and amplitudes which vary according to the position of the point of incidence relative to the monopole.

4.1.3 Properties of the Acoustic Dipole

An acoustic dipole consists of two monopoles, 180 degrees out-of-phase, located in close proximity. While two such monopoles occupying the same location would result in complete cancellation, the monopoles forming a dipole are a short distance apart, with the line between the two dipoles forming the "dipole axis". The effect of this formulation is to produce angular variance of the output pressure, with a minima of zero radiation normal to the dipole axis.

The dipole pressure, as calculated from an approximation of two monopole sources seperated by a distance that is small compared to a wavelength, is:

$$p = -\rho_0 c_0 \frac{k^2 Q s}{4\pi} \frac{e^{jkr}}{r} \cos(\zeta) \, , \tag{4.5}$$

where ζ is the angle relative to the dipole axis and s is the distance between the two dipoles (each monopole in the dipole has a source with amplitude Q). In this formulation, the dipole axis will be oriented normal to the plane containing the pressure distribution. For the purposes of these calculations, s will be equal to 1/10th of a wavelength or less. The output of a dipole is cylindrically symmetric about the dipole axis, with positive and negative pressure regions to the front and back. The

maximum radiated pressure is along the dipole axis, reducing with angle to zero at the normal to the dipole axis.

The velocity created by the dipole is calculated in the same fashion as Equation 4.4, and shows the same relationship to the monopole's velocity as the monopole-dipole pressure relationship: i.e.,

$$v_r = -j\frac{k^2 Q s}{4\pi}(1 - \frac{1}{jkr})\frac{e^{jkr}}{r}\cos(\zeta)\vec{r}. \tag{4.6}$$

Because a dipole is dependent on the cancellation between two monopole sources, the efficiency of the dipole radiation is much lower than that of a monopole by a factor of $sk\cos(\zeta)$; for s equal to 1/10th of a wavelength, this number has a maximum value of 0.63 and the dipole will always be a less-efficient radiator than a monopole.

The dipole is useful for analysis because it is a closer approximation of a real source than a monopole. An unbaffled speaker, for example, will exhibit dipole-like behavior due to the alternating dilation and expansion of air on each side of the speaker.

While a single monopole or dipole cannot generate plane waves, a phased combination of sources can be used to approximate an incident wave on a surface. By adding pressure from multiple sources, we can approximate a desired pressure distribution.

4.2 Least-Squares Approximation of Pressure Distributions using Multiple Sources

By phasing and amplifying each source in an array appropriately, the array can be used to create an approximation of a plane wave on a surface. The quality of the fit between the ideal and generated pressure distributions depends on many variables, including the position and spacing of the sources, the type of sources used, and the amount of decay in an evanescent wave.

A schematic of the situation modeled here is shown in Figure 4.1. A pressure distribution along a plane is sampled along the surface over a distance L_x (1,024 points

were sampled in this model), thus creating an array of points, $P(x_i)$, representing an incident wave of a particular frequency, f, and angle of incidence, $\theta_r + j\theta_i$. The source array is centered over the center of the target distribution, with N sources along a line of length L located at Z_0 above the plane.
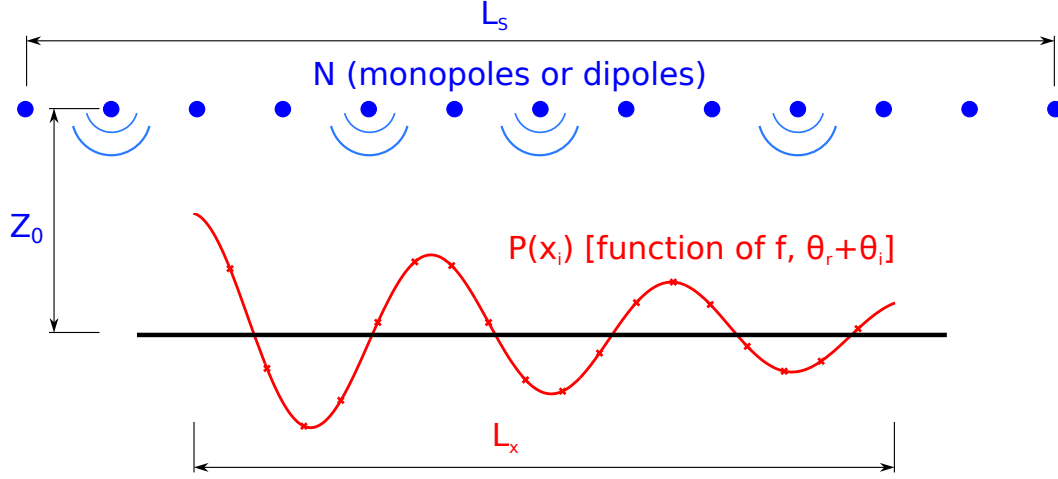
Figure 4.1. Schematic of multi-source array used to fit pressure distributions, showing variables L_x, f, $\theta_r + j\theta_i$, Z_0, L_s, and N.

The method for generating pressure distributions from multiple monopole sources that is used as the basis for this calculation was first presented by Kirkeby and Nelson [46]. Their formulation uses monopole sources; expansion of this model to allow for dipoles sources may provide a more efficient fit to the desired pressure distribution.

The Kirkeby and Nelson model comprises a system of linear equations of the form:

$$[P]_i = [H]_{ij}[q]_j \, , \tag{4.7}$$

where q_j is the complex amplitude (which incorporates a phase as well as a magnitude) of the source located at $\vec{x}_j$, P_i is the value of the desired pressure distribution at points $\vec{y}_i$, and $[H]$ is a matrix that relates the pressure $P(x_i)$ and the monopole strength q_j. The elements of the matrix are:

$$H_{ij} = \frac{e^{jkr_{ij}}}{r_{ij}} \; ; r_{ij} = |\vec{x}_i - \vec{y}_j| \; . \tag{4.8}$$

The solution for $[q]$ yields the monopole phase and amplitude for a least-squared-error with the pressure distribution. The resulting pressure approximation could be calculated from the $[q]$ vector by summing the resulting pressure of all the monopoles. The monopole source strength, Q, as used in Equations 4.3 and 4.4 is:

$$Q_j = j\frac{4\pi}{\rho_0 c_0 k} q_j \; . \tag{4.9}$$

For a dipole, a similar formulation is possible, with a slight modification in terms of $[H]$ to reflect the radiation properties of a dipole: i.e.,

$$H_{ij} = \frac{e^{jkr_{ij}}}{r_{ij}} \cos(\zeta_{ij}) \; , \tag{4.10}$$

where ζ_{ij} is the angle between $\vec{x}_i$ and $\vec{y}_j$ (i.e., the polar angle from the dipole axis). Once q_j has been defined as the monopole amplitude, the source strength, Q_j, of the dipole is:

$$Q_j = j\frac{4\pi}{\rho_0 c_0 s k^2} q_j \; . \tag{4.11}$$

In order to determine the degree to which the generated pressure and velocity distributions fit the desired incident wave, fit coefficients R_P and R_V are calculated from the sum of the residual values at each x_i point between the desired pressure P (or V for R_V) and the approximate pressure $\tilde{P}$ and the RMS value of the signal:

$$R_P = 1 - \sqrt{\frac{\sum_i (P(x_i) - \tilde{P}(x_i))^2}{\sum_i P(x_i)^2}} \; . \tag{4.12}$$

This fit coefficient value is different from the coefficient of determination in that the sum of the squared value is always taken with respect to zero, the sum of a complete period of a sine wave. For an oscillating value, the sum of the squares will yield a value of R_P that has a maximum value of 1, indicating that $\tilde{P}(x_i) = P(x_i)$ at all x_i values. A value of 0.98 or higher would indicate a good fit of the pressure distribution.

A value of 0 would be the theoretical minimum value obtained during a least-squares curve fit.

Figure 4.2 shows example pressure distribution fits for a generic trace pressure distribution. While the fit coefficient 0.883 approximates the pressure distribution well, the 0.999 fit is indistinguishable from the ideal pressure; the maximum difference among the 1024 point in that case is 0.0015, less than 0.2% of the wave amplitude.
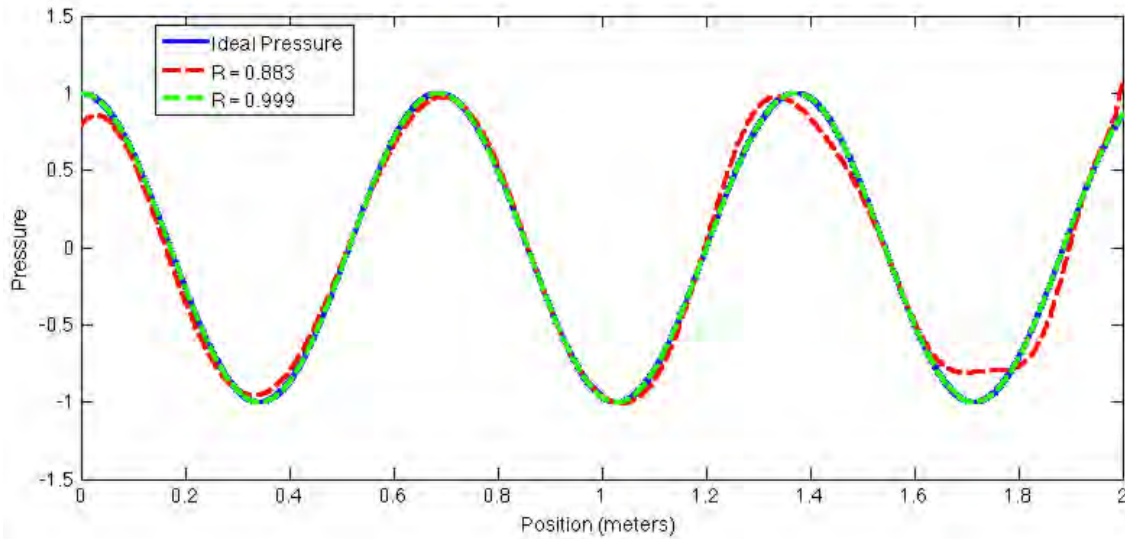
Figure 4.2. Sample approximate pressure distribution for a plane wave pressure distribution; approximate pressure distributions with a fit of 0.883 and 0.999 are shown.

In simulating incident plane waves and the required multi-source generation, seven variables come into play. The length of the pressure distribution, L_x, will affect the distance that needs to be modeled, as well as accounting for the variance of in the overall signal. The frequency, f, and angle, $\theta_r + j\theta_i$, of the incident wave will determine the surface wavenumber, with higher wavenumbers having more variation along the surface and therefore being harder to approximate. An imaginary component of the incident angle also determines the relationship between pressure and velocity. There are N sources located at a height Z_0 above the plane, and along a line of length L_s centered above the pressure distribution. Table 4.1 summarizes these variables. Each

of these variables affects the resulting fit of the equation (expressed by R_P and R_V), and should be considered.

Table 4.1. Table of variables applicable to multi-source arrays and the desired pressure distribution.

Variable Name	Variable	Units
Length of Distribution	L_x	meters
Frequency of Wave	f	Hertz
Angle of Incidence (Real)	θ_r	radians
Angle of Incidence (Imaginary)	θ_i	radians
Number of Sources	N	(none)
Array Standoff	Z_0	meters
Array Length	L_s	meters

4.3   Input Parameter Effects on Plane Wave Fit Using Multi-Source Arrays

Variations in the seven variables determining the fit of an incident plane wave using a multiple source array effect the fit quality of the resulting pressure and velocity approximations. By restricting these variables to the important factors and relevant values it is more easily possible to analyze a complex problem.

In order to reduce the number of variables modeled, we will assume that the pressure distribution to be modeled, L_x, is always 50 centimeters in length. Clearly, greater lengths will be more difficult to fit (depending on the complexity of the pressure distribution), requiring more sources or a longer array; however, this is a reasonable approximation for the size of a suspicious package.

Since the interest in our study is the linear region of wave propagation in air, our analysis will be limited to frequencies below 20 KHz. The incident angle can vary

between 0 and 90 degrees; however, previous analysis has shown that the significant contributions of evanescent waves lie at lower angles of incidence.

The number of sources used will vary from 1 to 64; 64 channels would be allow 8x8-channel output cards to generate the array signals. It is unknown what stand-off distance will be requested; a maximum of 100 meters is assumed. Similarly, a maximum source length of 15 meters will be used.

4.3.1   Incident Wave Parameters

Of primary importance is whether or not the trace pressure distribution generated is properly modeling the normal velocity inherent in the incident plane wave. The trace pressure distribution is a unique function of the angle of incidence and frequency, and the appropriate velocity should follow if the pressure is fit correctly. However, approximating the trace pressure from multiple sources will not necessarily yield the appropriate velocity relationship.

For a plane wave distribution generated by 64 sources with a source offset 5 meters from the plane and a span of 4 meters, the resulting fit coefficient variation with angle and frequency is given in Figure 4.3. While the pressure has a gradual transition in the quality of the fit, the velocity transitions suddenly, with the good fit region of velocity matching the good fit of the pressure. This correlation between matching pressure and velocity at better regions of fit shows that fitting the pressure will allow for accurate approximation of the normal velocity. However, poor fit of the pressure will led to a lower-quality fit of the velocity. Therefore, only a high quality of fit of the desired pressure will produce the proper chracteristics of an incident wave.

Figure 4.3 also shows the effect of frequency and incidence angle on the ability of the multi-source array to fit a desired pressure distribution. An increase of either the frequency or angle of incidence will increase the variation across the desired region, thus making a fit more difficult. The border constituting the region of good fit coefficient appears to be defined by an inverse relationship between the sine of the

incident angle and the frequency, $\sin(\theta) \propto 1/f$. This would seem to indicate that the trace wavelength $\lambda_x = c/(f \sin(\theta))$ could serve as an indicator of correct fit; however, Figure 4.4 shows the border plotted against a line of constant wavelength fit. The wavelength plotted has been chosen to minimize the least-squares error across the entire frequency range; it can be clearly seen that the border of good fit does not follow the constant wavelength curve precisely. Because the wavelength of the monopole varies with f, the fit coefficient is not solely dependent on the trace wavelength. For example, a 1 kilohertz wave with an incident angle of 20 degrees ($\lambda_x = 1$ meter) will not have similar fit coefficient properties (with respect to the geometry of the system) as a wave of 500 Hertz with an incident angle of 43 degrees (which has the same equivalent wavelength), because the resulting wavelength of radiated sound from the monopole sources at 1 kilohertz are half the length of those radiated by 500 Hertz sources.
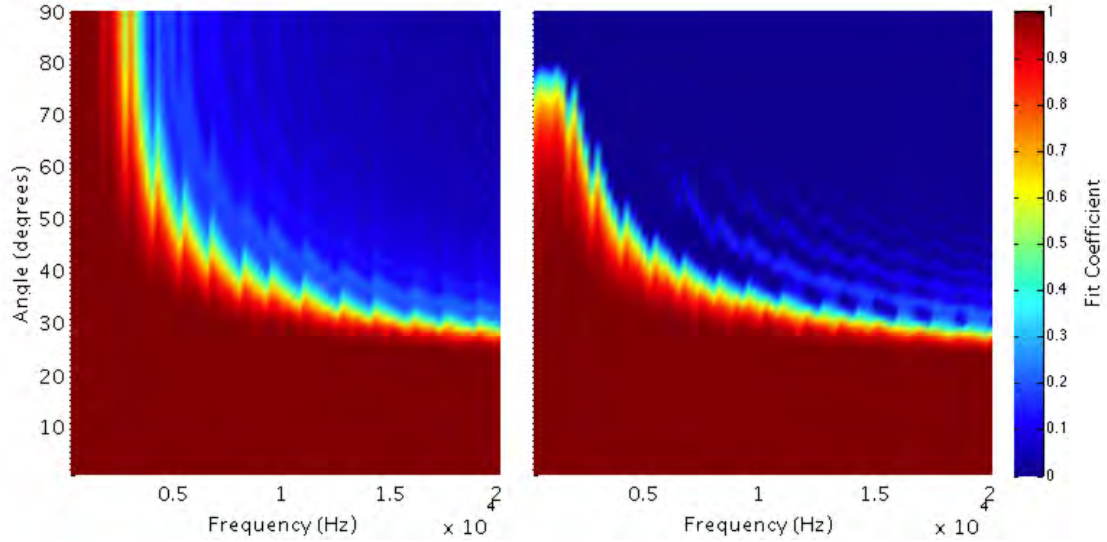
Figure 4.3. Fit coefficient variation for the pressure (left) and normal velocity (right) with angle and frequency for a source array 5 meters from the plane, with 64 sources spanning 4 meters.

An increase of the length of the source array will increase the quality of the fit, as seen in Figure 4.5 for the geometry of Figure 4.3 except with a source span of 10
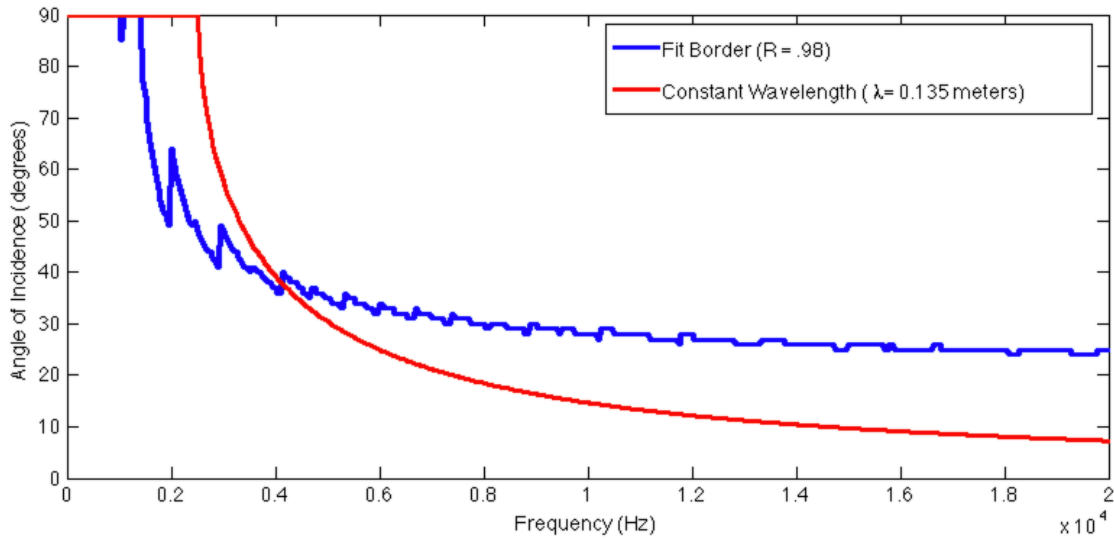
Figure 4.4. Border of $R = 0.98$ fit plotted with best-fit line of trace wavelength, $\lambda_x = c/(f \sin(\theta)) = 0.135$. The fit of the trace wavelength curve shows that the trace wavelength is only an approximate indicator of the good fit region.

meters. The increase in the quality of fit is possibly due to the additional sources further out, which will produce more plane-wave-like behavior. The additional length of the source array reduces the source density, but provides improved fit at higher angles, which have a lower trace wavelength. This would indicate that there isn't a proportional relationship between source density and the trace wavelength that can be fit by the array.

Increasing the standoff distance will reduce the quality of the fit; Figure 4.6 shows the fit for a source array with a length of 10 meters and a standoff of 30 meters. The same relationsip between the incident angle and frequency are present; however, the fit coefficients are much lower for similar angles and frequencies. The "spikes" in angle for good fit, which were present but not as prominent in the previous simulations, are due to the poor fit of non-integer wavelengths in the simulation. An increase of the pressure distribution length can shift these if needed.
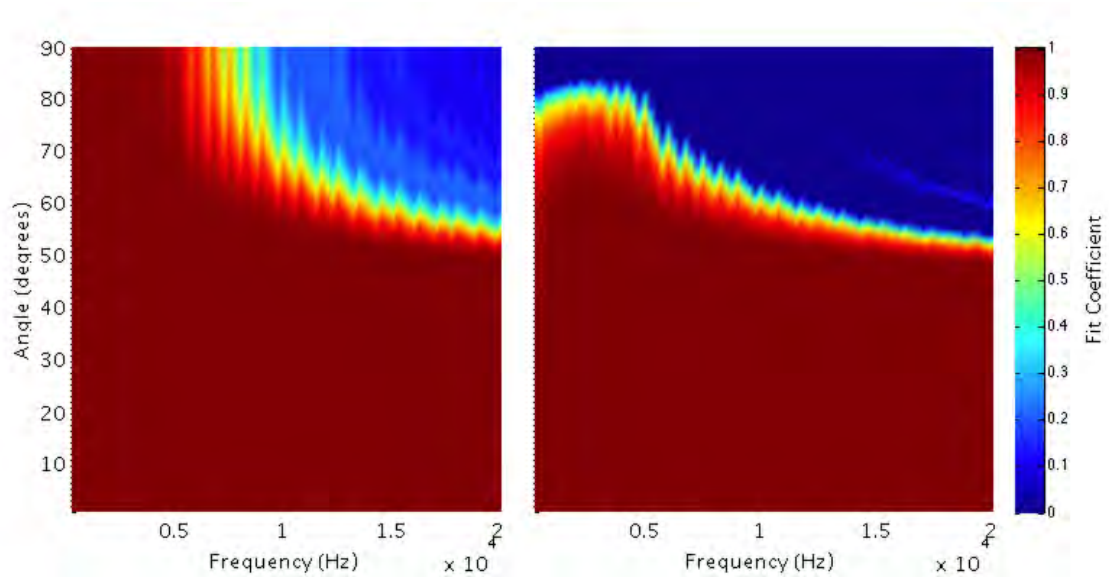
Figure 4.5. Fit coefficient variation for the pressure (left) and normal velocity (right) with angle and frequency for a source array 5 meters from the plane, with 64 sources spanning 10 meters.
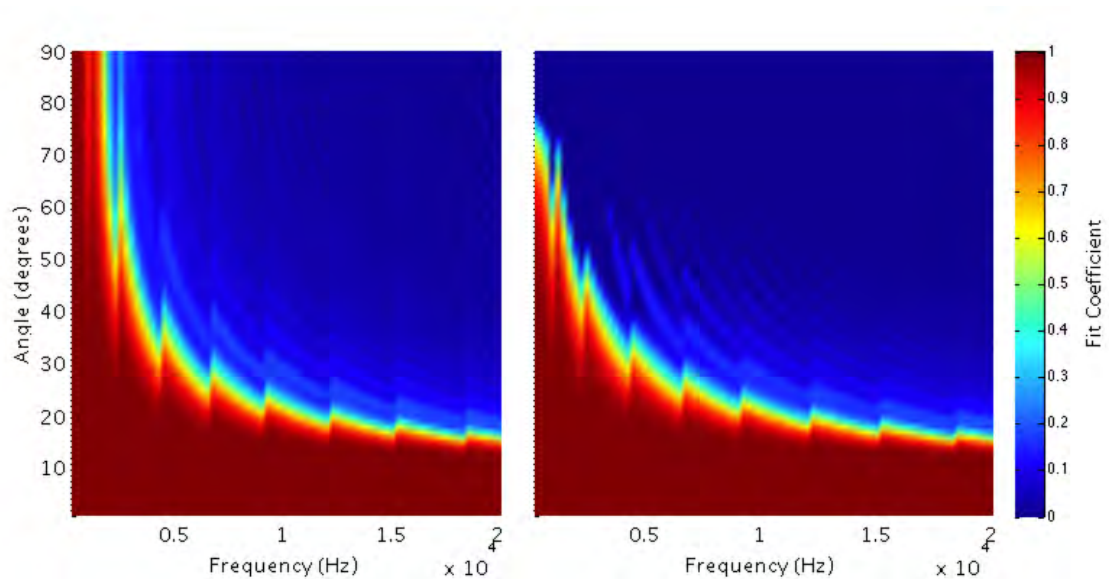
Figure 4.6. Fit coefficient variation for the pressure (left) and normal velocity (right) with angle and frequency for a source array 30 meters from the plane, with 64 sources spanning 10 meters.

The plots of fit coefficient show the difficulty in fitting high frequency and high angle-of-incidence waves. While additional geometry and source parameters may improve the fit of pressure and velocity, the angle of incidence is a limiting parameter.

4.3.2 Geometry Parameters

As seen in the previous section, by decreasing the standoff distance or increasing the source length, the quality of the fit can be improved. Fit coefficient variation with these parameters is shown in Figure 4.7 for an incident wave of 2 kilohertz at a 20 degree incidence angle, as modeled using 64 sources. There is a linear relationship between the standoff distance and the source length for the border of fit coefficients, although significantly more source length is required to obtain an improved fit.
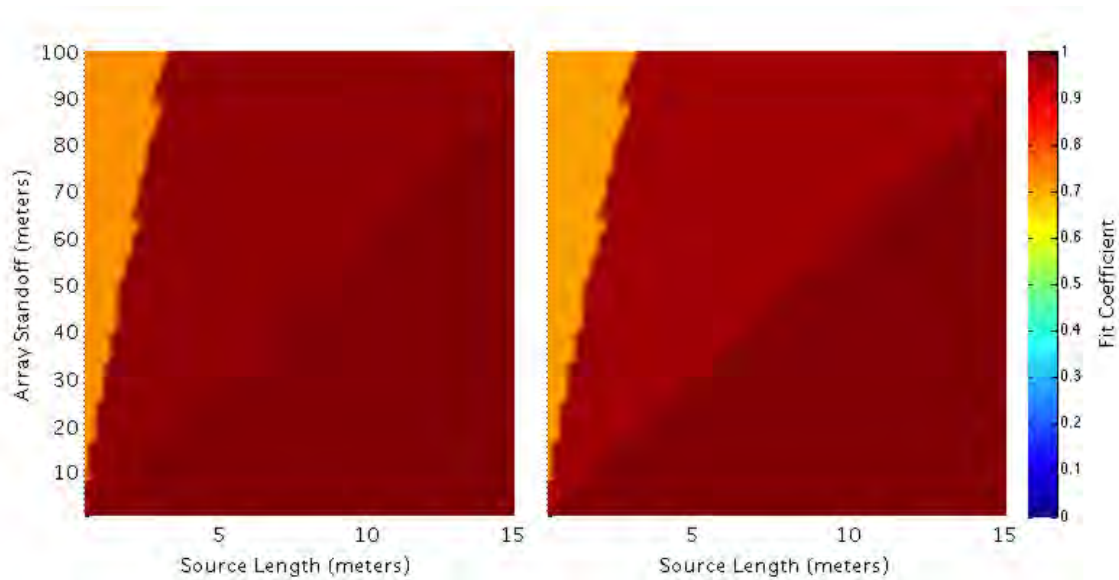
Figure 4.7. Fit coefficient variation for the pressure (left) and normal velocity (right) with standoff and source length for an incident wave of 2 kilohertz at an incident angle of 20 degrees modeled using 64 sources.

For a higher frequencies, a substantially longer source length must be used to approximate a plane wave, as seen in Figure 4.8. The lower slope of the good fit

border equates the to need for a greater source length at increased standoffs. For a higher incidence angle, the quality of the fit decreases further, as seen in Figure 4.9.
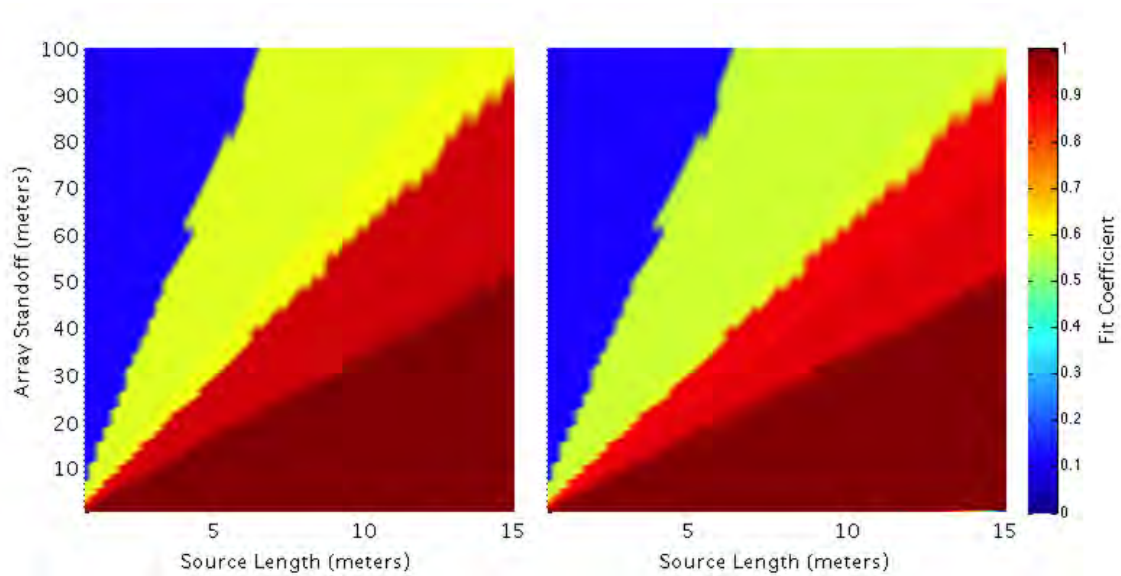
Figure 4.8. Fit coefficient variation for the pressure (left) and normal velocity (right) with standoff and source length for an incident wave of 5 kilohertz at an incident angle of 20 degrees modeled using 64 sources.

A study of the source geometry shows that source length and standoff distance need to increase in tandem in order to maintain a good fit of the pressure distribution. For higher frequencies and incidence angles, the proportional source length increase with standoff becomes greater; that is, a greater source length is needed for an equivalent standoff distance in harder-to-fit plane waves.

4.3.3 Source Length and Density

Previous examples have been based on the assumption that the maximum number of sources was used; a reduction of the number of sources in the array would allow for a lower-power solution to obtain evanescent waves.
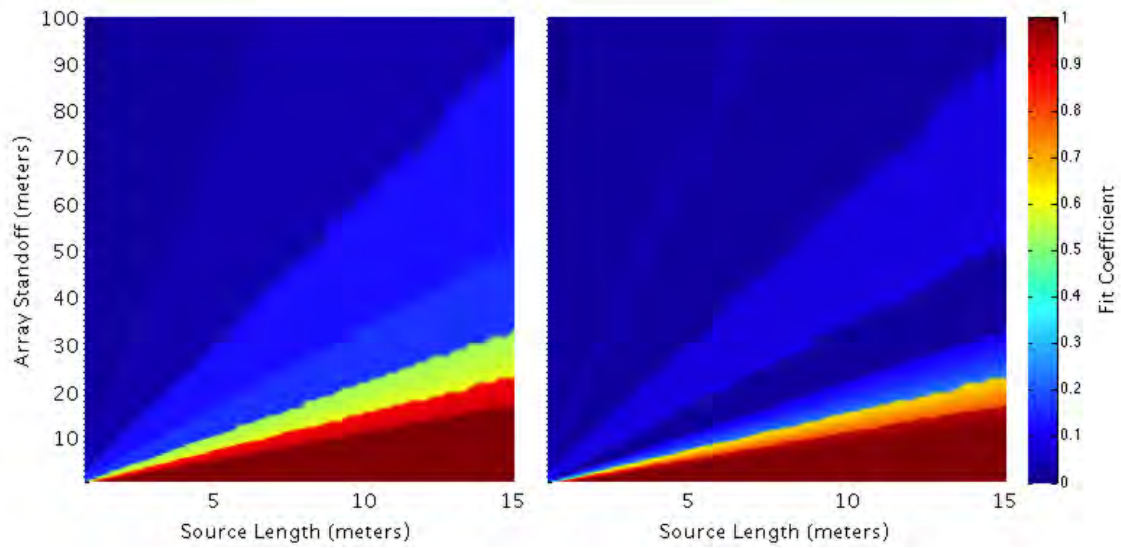
Figure 4.9. Fit coefficient variation for the pressure (left) and normal velocity (right) with standoff and source length for an incident wave of 5 kilohertz at an incident angle of 40 degrees modeled using 64 sources.

Figure 4.10 shows the typical variation of fit coefficient with source number and length, using an incident wave of 2 kilohertz at 20 degrees and a linear array 30 meters from the surface. The region of good fit is defined by a horizontal border on the lower end and a high-slope vertical boundary. The horizontal slope suggest a minimum number of sources needed to approximate the incident wave; for the current situation, this is 8 sources, far fewer than the 64 in modeling efforts with a fixed number of sources. The vertical line shows a slight slope, indicating a decrease in source number with additional length required to maintain fit.

For higher frequencies, as shown in Figure 4.11, the minimum number of sources is increased; this would suggest that the number of sources is a function of the frequency and incidence angle. There is a small slope at the bottom edge of the good fit region, thus showing the need for increased source numbers with additional length; this is indicative of a minimum source density needed to accurately model the incident wave. Otherwise, the higher frequency plot mirrors the trend seen in the previous figure,
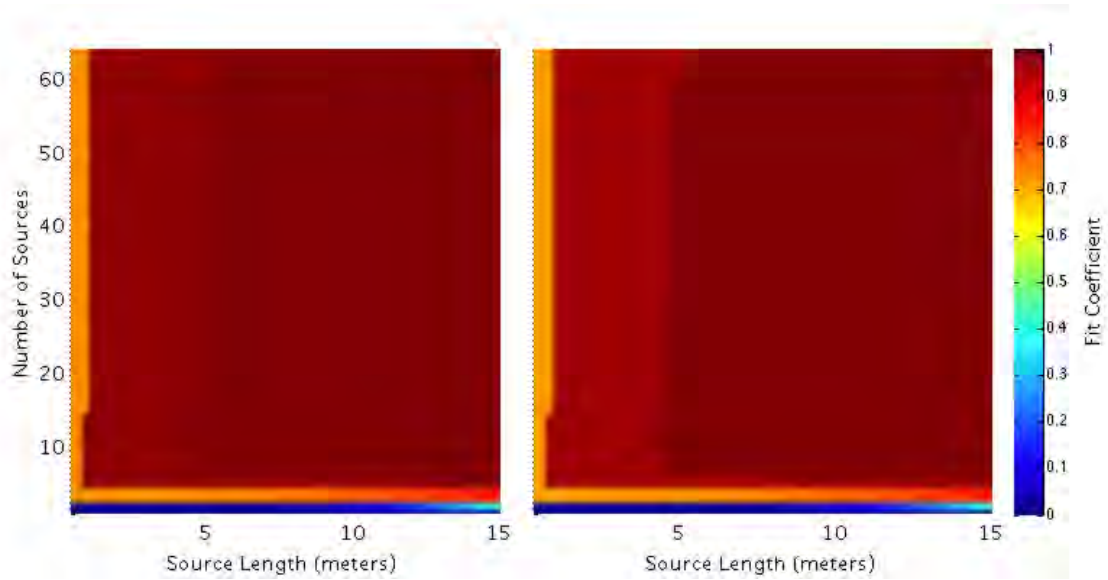
Figure 4.10. Fit coefficient variation for the pressure (left) and normal velocity (right) with source length and number of sources for an incident wave of 2 kilohertz at an incident angle of 20 degrees and a source standoff of 30 meters.

where this is very little variance once a minimum source length and number have been achieved.

4.3.4 Modeling Evanescent Waves

By treating the incident angle as a complex angle and separating its real and imaginary components into separate variables, the effect of evanescent waves can be introduced into the model. The use of complex angles will introduce a pressure decay into the system and a phase difference between the pressure and velocity that are not seen when modeling conventional plane waves.

The addition of an imaginary component to the angle, which is shown in Figure 4.12 for variation with real and imaginary angle for a 2 kilohertz incident plane wave, has only a slight effect on the fit of the pressure, reducing the angle of good fit by 9 degrees from a complex angle of 0 to 0.1 radians. The quality of the velocity
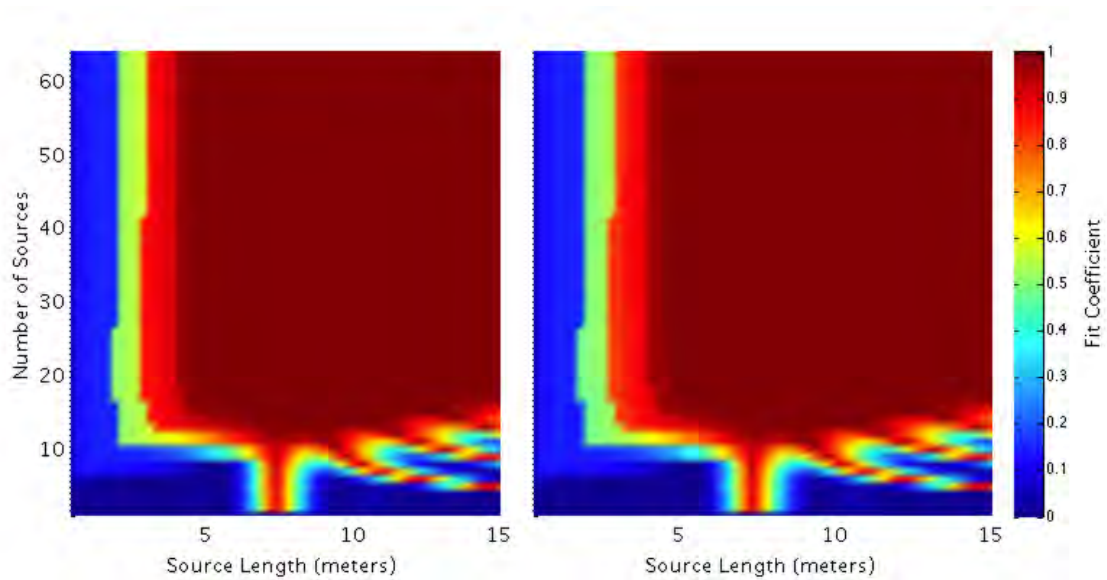
Figure 4.11. Fit coefficient variation for the pressure (left) and normal velocity (right) with source length and number of sources for an incident wave of 8 kilohertz at an incident angle of 20 degrees and a source standoff of 10 meters.

fit, however, decreases significantly with increasing evanescent angle. This is due to the phase difference that the evanescent angle imposes on the velocity; a greater imaginary component pushes the phase difference between the pressure and velocity towards 90 degrees. While a monopole has properties similar to an evanescent wave in its near-field, these are dependent on geometry, and relying on far-field properties of a monopole will not produce evanescent components.

4.3.5 Dipole Multi-Source Arrays

The use of dipole sources in the array has little effect on any of the parameters or the quality of fit shown for monopoles. All the previously presented results show no appreciable difference when modeled using dipoles in place of monopoles. For example, Figure 4.13 shows the improvement in fit coefficient for a dipole array compared to the monopole array for the angle and frequency variation shown in Figure 4.5.
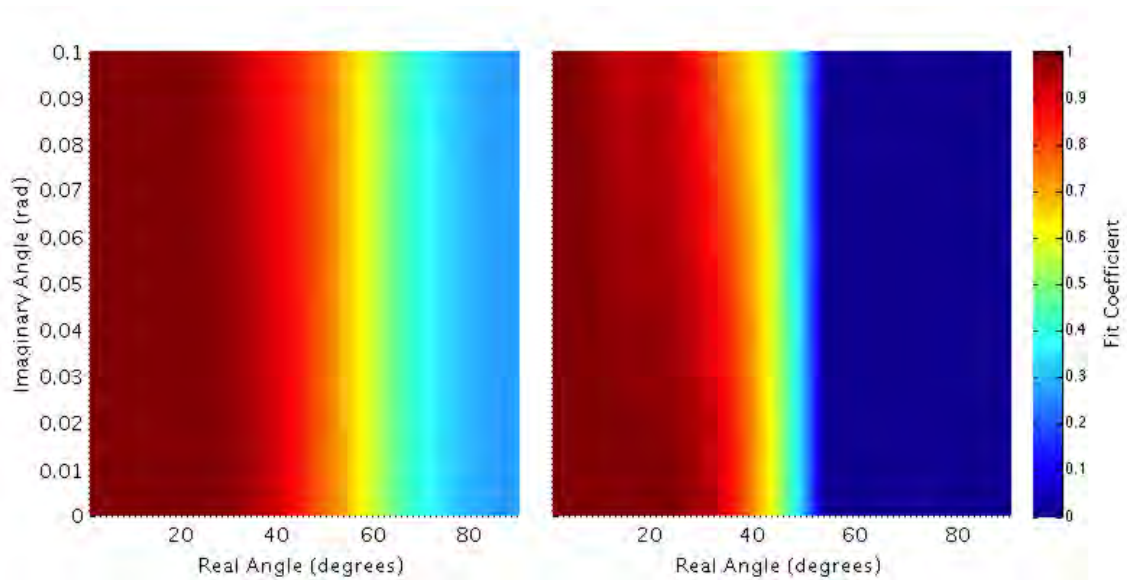
Figure 4.12. Fit coefficient variation for the pressure (left) and normal velocity (right) with real and imaginary angle components for an incident evanescent wave of 2 kilohertz and a source geometry of 4 meters with a standoff of 20 meters.

While there are small regions of fit with an increase of 0.25, all these regions occur where the monopole distributions provide a poor fit, with the highest fit being 0.83.

Figure 4.14 shows the improvement in fit coefficient when using a dipole array for the same data shown in Figure 4.10. The use of a dipole array has a negligible effect on fit coefficient, with a maximum improvement of 0.01 in small regions, and change of less than 0.001 in most regions.

That the dipole and monopole arrays have such close fit and similar parameters is indicative of the local effect of each individual source. A dipole differs from a monopole by the cosine of the angle to the dipole axis; the acoustical output near the axis will be similar to the monopole. Because the dipole and monopole outputs from the array are similar, this suggests that the effects of each source are localized near the dipole axis (which, in this case, is normal to the plane). There may be an additional benefit to using dipole sources if the orientation of each source can be
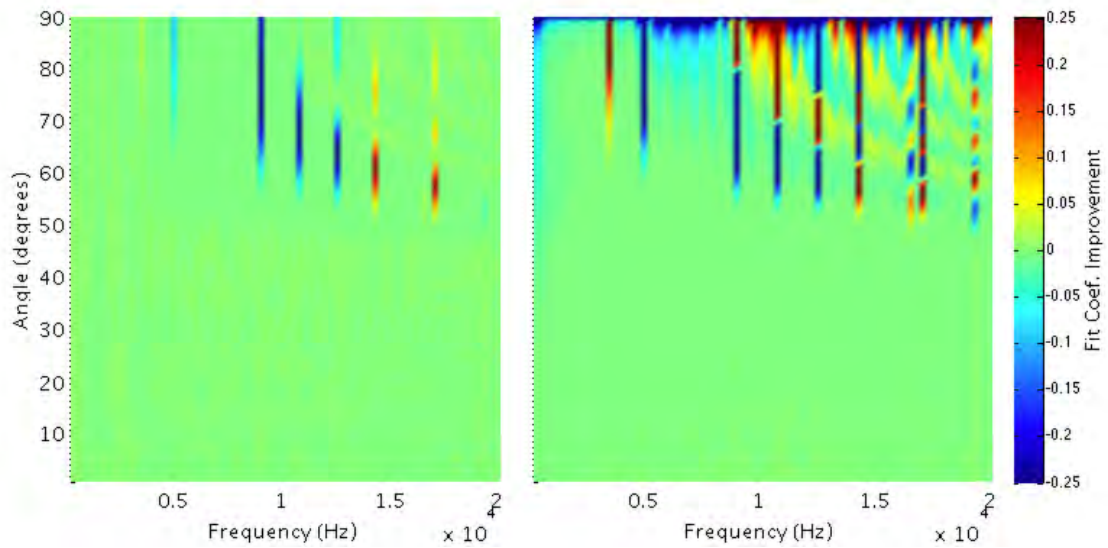
Figure 4.13.   Fit coefficient improved between the dipole and monopole arrays for a source array 5 meters from the plane, with 64 sources spanning 10 meters.
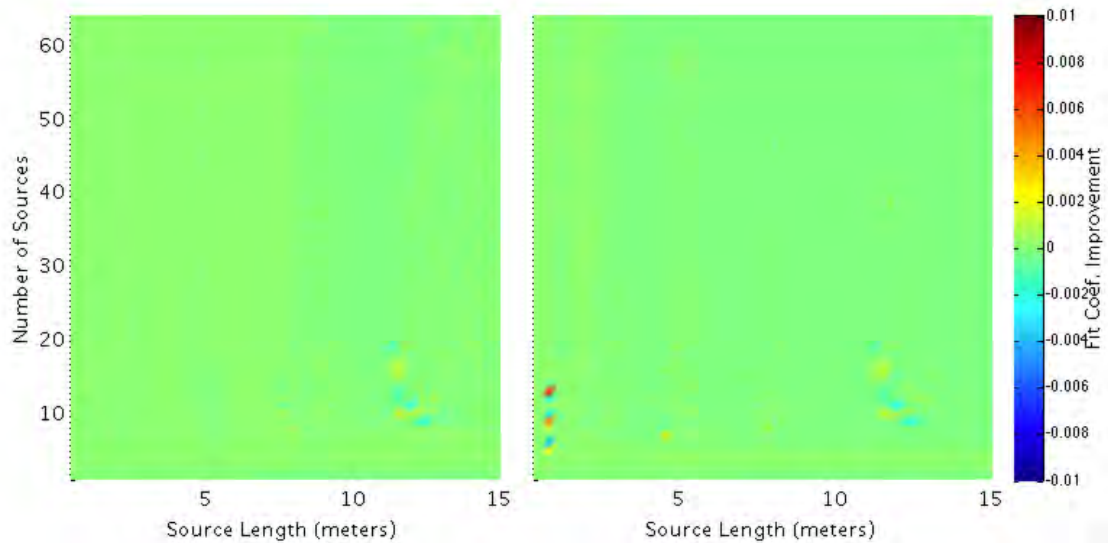
Figure 4.14.   Fit coefficient improved between the dipole and monopole arrays for an incident wave of 2 kilohertz at an incident angle of 20 degrees and a source standoff of 30 meters.

optimized as part of the model; however, the addition of dipole orientation to the model will form a nonlinear system of equations.

A dipole is a much less efficient radiator than a monopole; therefore, for an equivalent source array with dipoles that have the same pressure output as monopoles, the array will be less efficient by the same factor, $sk\cos(\zeta)$, that a dipole is less efficient than a monopole.

4.4   Conclusions

Multi-source arrays have been shown to be a viable option for constructing trace pressure distributions on a plane. The model constructed here shows the influence of incident wave, source geometry, and evanescent wave parameters on the fit of the desired waves, for both monopoles and dipoles.

While monopoles and dipoles have characteristics distinct from a plane wave, a multi-source array can be modeled using a least squares formulation to produce an approximation of the desired incident pressure and velocity. The quality of the fit of the approximation is judged by comparing the desired pressure and velocity to their approximations.

The fit of the multi-source system is heavily dependent on the incident wave parameters; beyond an angle dependent on the geometry of the source array, the fit is poor, with further and smaller arrays being able to fit fewer angles of incidence. Frequency plays a role as well, with a decrease in the quality of the fit with increasing frequency.

In the geometry of the source array, the standoff distance decreases the quality of the fit, but additional length can be added to the array to improve the quality of the fit. There is a minimum source density that must be achieved, but beyond this there is little variation in the quality of the fit.

Evanescent waves adversely affect the fit of the system, possibly due to the phase difference between the pressure and velocity in the system. While the pressure fit

varies only slightly with evanescent components, the velocity will fit will be worse due to phase conditions imposed on the wave that cannot easily be fulfilled.

A dipole array provides similar fit as a monopole array, with all parameters maintaing similar variation to their monopole counterparts.

CHAPTER 5. WAVE PROPAGATION IN MULTI-LAYER MATERIALS

The amplitude and phase of a wave propagating through an infinite homogeneous material change only due to the phase change with distance and possibly the damping in the material. For layered materials each component layer has its own propagation characteristics, the combination of which causes the resulting multi-layer material to have a distinct susceptibility to acoustic excitation. By modeling the wave propagation characteristics of the overall material, we can accurately design waveforms that excite the components of the material that are of interest.

In this chapter, a model for wave propagation through layered materials is presented and verified. Applications for the model and analysis techniques in the wavenumber-frequency domain are presented. A discussion of the effects of evanescent waves on layered materials concludes the chapter.

5.1 Multi-Layer Wave Propagation Model

The multi-layer propagation model used here is based on a formulation by Brouard [21], which combines the previous models for transfer matrix calculation of waves in a solid (by Folds [19]) and a fluid (Pierce [20]) by developing these transfer matrices into a system of equations. Another major innovation in Brouard's formulation was the use of a fluid-solid coupling matrix, which would transfer the material states in a fluid into those in a solid (and vice-versa). In these models, the material states at each interface are unknowns and propagation characteristics through each layer are assumed to relate states on each side of a layer of material. The transfer matrices, which Pierce and Folds used in series but which Brouard uses as a component for developing a system of equations, propagate the pressure and velocity through a region

of material accounting for the phase change over a length L in the material layer. For example, the relationship between the pressure and normal velocity amplitude vector $[P]$ in a fluid from a z_0 to z_L span is (for an $e^{-j\omega t}$ time convention):

$$[P]_{z=0} = \begin{bmatrix} p \\ v_z \end{bmatrix}_{z=0} = \begin{bmatrix} \cos(k_z L) & j\frac{\omega\rho}{k_z}\sin(k_z L) \\ j\frac{k_z}{\omega\rho}\sin(k_z L) & \cos(k_z L) \end{bmatrix} \begin{bmatrix} p \\ v_z \end{bmatrix}_{z=L} , \qquad (5.1)$$

where k_z is the wavenumber in the direction normal to material surface. A solid material will have an equivalent $[P]$ vector containing pressure and velocity amplitudes for both longitudinal (σ_z, v_z) and shear waves (σ_x, v_x), and a 4-by-4 transfer matrix relating pressure and velocity relationships over distance.

Transfer-matrix methods of simulating wave propagation through multi-layer materials relate the material states between layer 1 and layer N as a series of these matrices that reflect propagation through each layer:

$$[P_1] = [T_1][T_2] \cdots [T_{N-1}][T_N][P_N] . \qquad (5.2)$$

The Brouard model expands upon this transfer-matrix approach to develop a system of linear equations (a similar formulation will be expanded upon in the following section):

$$\begin{bmatrix} -[I] & [T_1] & & & \\ & -[I] & [T_2] & & \\ & & -[I] & [T_3] & \\ & & & \ddots & \\ & & & & -[I] & [T_N] \end{bmatrix} \begin{bmatrix} [P_1] \\ [P_2] \\ [P_3] \\ \vdots \\ [P_N] \end{bmatrix} = [0] . \qquad (5.3)$$

The resulting matrix is an $N-1$ by N system; the transfer function between the incident pressure amplitude p_1 and the m-th pressure or velocity amplitude in the matrix formulation is related to the derivative of a subset of the matrix with the first and m-th row removed:

$$H_{1m} = (1 + R_1)\frac{|D'_m|}{|D'_1|} \; .$$

$$(5.4)$$

While this type of formulation allows for calculation of multiple states in the system, the drawbacks are that it does not distinguish between forward- and backward-going waves in the system, and that inter-layer material states cannot be discerned. Both of the latter quantities are important for calculating the intensity transmitted through layers, which would be a true indicator of energy propagation into the system. Furthermore, the use of a wave-based method would allow for evanescent wave inputs in order to model their effectiveness in energy propagation. The model described here modifies a formulation by Jessop et al. [26], which uses the wave potentials in each layer to simulate propagation. The resulting system of equations for the multi-layer system are generated by equating the states at each interface.

5.1.1 Wave Potential Model Formulation

The multi-layer material modeled consists of $(N-2)$ layers of fluid or solid bounded by semi-infinite fluid layers on each side, with the incident fluid numbered layer 1 and the transmitted bounding fluid layer N. An incident wave in the semi-infinite first layer is incident at an angle θ_1. The trace wavenumber on the surface $k_x = k_{1x} = k_1 \sin(\theta_1)$ is constant throughout all layers, while the normal wavenumber $k_{1z} = k_1 \cos(\theta_1)$ will change in each layer, causing refraction in each subsequent θ_i. A schematic of the setup is shown in Figure 5.1.

The system of equations governing wave propagation in the multi-layer material is formulated by equating the states at each of the $(N-1)$ interfaces in the system. The forward- and backward-going pressure and shear wave amplitudes are four unknowns in each layer; for a fluid, the shear wave amplitudes are set to zero. The material states are calculated as follows.

A wave propagating in the negative z-direction through a fluid or solid at an angle θ can be represented by a wave potential of:
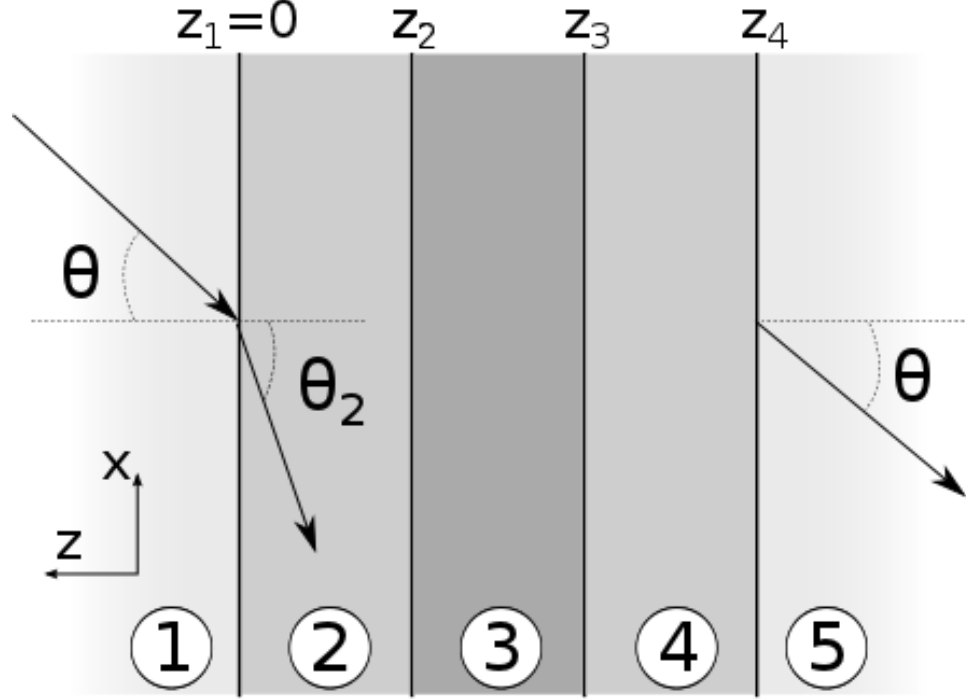
Figure 5.1. Schematic diagram of a sample $N = 5$ multi-layer material. A semi-infinite fluid exists on each side of the three-component material.

$$\phi = Ae^{jk_x x - jk_z z} \,, \tag{5.5}$$

(The time constant $e^{-j\omega t}$ is excluded for brevity). Note that this potential is similar to the pressure equation for a propagating wave; however, the amplitude A of the wave potential is not equivalent to the pressure amplitude.

A single wave potential equation is used to represent longitudinal (pressure) waves, and another wave potential ψ (which is similar to the equation for ϕ but propagates at an angle γ with wavenumber κ) is used to represent transverse (shear) waves in the system:

$$\psi = Be^{j\kappa_x x - j\kappa_z z} \,. \tag{5.6}$$
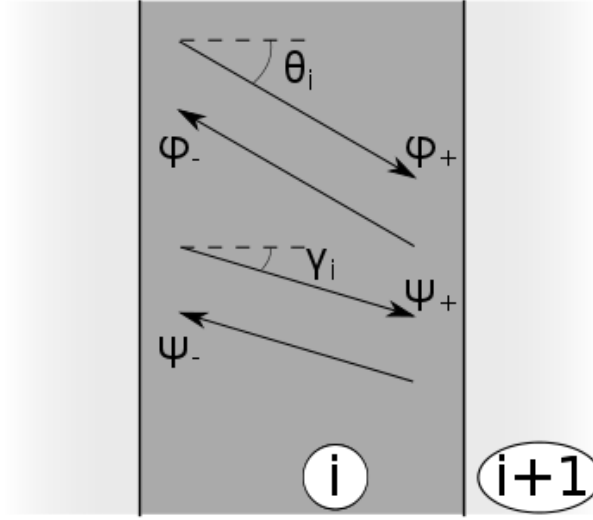
Figure 5.2. Wave propagation characteristics and geometry, showing the four waves in a solid system: two forward-going waves, both longitudinal and shear, and their companion backward-going waves.

At a material interface, a wave incident in one material will generate a reflected wave in the incident material and transmitted waves in the other material. The reflected wave travels in the positive z direction and is expressed as:

$$\phi = A_R e^{jk_x x + jk_z z} \; , \tag{5.7}$$

with an equivalent expression for shear waves in a solid material. The transmitted waves travel in the negative z direction and have the expected form with amplitude A_T.

A solid material will be defined by a density ρ and longitudinal and shear wave speeds c and b. The wave speeds can be calculated from other material properties; for example, if given the Lamé constants λ and μ, the wave speeds c and b can be calculated as:

$$c = \sqrt{\frac{\lambda + 2\mu}{\rho}} \; , \tag{5.8}$$

$$b = \sqrt{\frac{\mu}{\rho}} \ . \tag{5.9}$$

The stresses in a solid consist of the normal stress σ_z and tangential stress σ_x, which can be computed from the wave potentials as:

$$\sigma_z = \frac{j}{\omega} \left[\lambda \nabla^2 \phi + 2\mu \left(\frac{\partial^2 \phi}{\partial z^2} + \frac{\partial^2 \psi}{\partial x \partial z} \right) \right] \ , \tag{5.10}$$

$$\sigma_x = \frac{j}{\omega} \left[\mu \left(2 \frac{\partial^2 \phi}{\partial x \partial z} + \frac{\partial^2 \psi}{\partial x^2} - \frac{\partial^2 \psi}{\partial z^2} \right) \right] \ . \tag{5.11}$$

A fluid cannot sustain shear; therefore $\psi = 0$, $\mu = 0$, and $\sigma_x = 0$, and the pressure in the fluid simplifies to:

$$p = -\lambda \nabla^2 \phi = -i\omega\rho\phi \ . \tag{5.12}$$

The velocity in fluid or solid materials can be computed from the wave potentials as:

$$\vec{v} = \nabla\phi + \nabla \times \psi \ , \tag{5.13}$$

which can be simplified into its constituent parts:

$$v_z = \frac{\partial \phi}{\partial z} + \frac{\partial \psi}{\partial x} \ , \tag{5.14}$$

$$v_x = \frac{\partial \phi}{\partial x} - \frac{\partial \psi}{\partial z} \ . \tag{5.15}$$

In a multi-layer material the model is formulated by using all the boundary conditions to create a system of linear equations in the wave amplitude coefficients.

Each constrained layer (layers 2 through $N - 1$) has forward-going (into the material, traveling in the negative z direction) and backward-going (traveling in the positive z direction) waves that are the product of transmission and reflection at each interface, labeled as ϕ_{i+} and ϕ_{i-}, respectively (with equivalent ψ_{i+} and ψ_{i-} for shear waves in a fluid). The total longitudinal potential ϕ_i in a layer represents the

combined effects of both forward- and backward-going waves; the material states in Equations 5.10-5.15 are calculated using the sum of both waves. The wave amplitudes are represented in a vector P_i for each layer.

At the interface between the i-th and $(i+1)$-th layers, located at a depth of z_i, the relationships between the material states form a system of equations that constitute several rows of the system of equations for the material. For solid-solid or fluid-fluid layer interfaces, the pressure and velocity in each direction is equal across each interface, and the pressure and velocity amplitude $[P]_i$ at the right side of the i-th layer is equal to the pressure and velocity at the left side of the $(i+1)$-th layer.

For example, the states across a fluid-fluid interface can be equated by applying equations 5.10 and 5.14 to yield two equations:

$$- j\omega\rho_i\phi_i(z_i) - (-j\omega\rho_{i+1})\phi_{i+1}(z_i) = 0 \ , \tag{5.16}$$

$$\frac{\delta\phi_i(z_i)}{\delta z} - \frac{\delta\phi_{i+1}(z_i)}{\delta z} = 0 \ . \tag{5.17}$$

Substituting the wave potential equations into 5.16 for the forward- and backward-going waves gives:

$$- j\omega\rho_i(A_{i+}e^{-jk_{z,i}z_i} + A_{i-}e^{jk_{z,i}z_i}) = -j\omega\rho_{i+1}(A_{(i+1)+}e^{-jk_{z,i+1}z_i} + A_{(i+1)-}e^{jk_{z,i+1}z_i}) \ , \tag{5.18}$$

and equation 5.17 will simplify to:

$$\begin{aligned} (-jk_{z,i})A_{i+}e^{-jk_{z,i}z_i} + (jk_{z,i})A_{i-}e^{jk_{z,i}z_i} = \\ -jk_{z,i+1}A_{(i+1)+}e^{-jk_{z,i+1}z_i} + jk_{z,i+1}A_{(i+1)-}e^{jk_{z,i+1}z_i} = 0 \ . \end{aligned} \tag{5.19}$$

The resulting system of equations for the interface are:

$$
\begin{bmatrix}
-\rho_i e^{-jk_{z,i}z_i} & -\rho_i e^{jk_{z,i}z_i} & \rho_{i+1} e^{-jk_{z,i+1}z_i} & \rho_{i+1} e^{jk_{z,i+1}z_i} \\
-k_{z,i} e^{-jk_{z,i}z_i} & k_{z,i} e^{jk_{z,i}z_i} & k_{z,i+1} e^{-jk_{z,i+1}z_i} & -k_{z,i+1} e^{jk_{z,i+1}z_i}
\end{bmatrix}
\begin{bmatrix}
A_{i+} \\
A_{i-} \\
A_{(i+1)+} \\
A_{(i+1)-}
\end{bmatrix}
=
\begin{bmatrix}
0 \\
0
\end{bmatrix}
$$

(5.20)

For a solid-solid interface, the four equations for continuous longitudinal and shear stress and velocity form four equations:

$$
(\lambda_i(-k_{x,i}^2 - k_{z,i}^2) - 2\mu_i k_{z,i}^2)(A_{i+}e^{-jk_{z,i}z_i} + A_{i-}e^{jk_{z,i}z_i})
$$
$$
+2\mu_i \kappa_{x,i}\kappa_{z,i}(B_{i+}e^{-j\kappa_{z,i}z_i} - B_{i-}e^{j\kappa_{z,i}z_i}) =
$$
$$
(\lambda_{i+1}(-k_{x,i+1}^2 - k_{z,i+1}^2) - 2\mu_{i+1}k_{z,i+1}^2)(A_{(i+1)+}e^{-jk_{z,i+1}z_i} + A_{(i+1)-}e^{jk_{z,i+1}z_i})
$$
$$
+2\mu_{i+1}\kappa_{x,i+1}\kappa_{z,i+1}(B_{(i+1)+}e^{-j\kappa_{z,i+1}z_i} - B_{(i+1)-}e^{j\kappa_{z,i+1}z_i})
$$

(5.21a)

$$
2\mu_i k_{x,i}k_{z,i}(A_{i+}e^{-jk_{z,i}z_i} - A_{i-}e^{jk_{z,i}z_i})
$$
$$
+\mu_i(-\kappa_{x,i}^2 + \kappa_{z,i}^2)(B_{i+}e^{-j\kappa_{z,i}z_i} + B_{i-}e^{j\kappa_{z,i}z_i}) =
$$
$$
2\mu_{i+1}k_{x,i+1}k_{z,i+1}(A_{(i+1)+}e^{-jk_{z,i+1}z_i} - A_{(i+1)-}e^{jk_{z,i+1}z_i})
$$
$$
+\mu_{i+1}(-\kappa_{x,i+1}^2 + \kappa_{z,i+1}^2)(B_{(i+1)+}e^{-j\kappa_{z,i+1}z_i} + B_{(i+1)-}e^{j\kappa_{z,i+1}z_i})
$$

(5.21b)

$$
jk_{z,i}(-A_{i+}e^{-jk_{z,i}z_i} + A_{i-}e^{jk_{z,i}z_i})
$$
$$
+j\kappa_{x,i}(B_{i+}e^{-j\kappa_{z,i}z_i} + B_{i-}e^{j\kappa_{z,i}z_i}) =
$$
$$
jk_{z,i+1}(-A_{(i+1)+}e^{-jk_{z,i+1}z_i} + A_{(i+1)-}e^{jk_{z,i+1}z_i})
$$
$$
+j\kappa_{x,i+1}(B_{(i+1)+}e^{-j\kappa_{z,i+1}z_i} + B_{(i+1)-}e^{j\kappa_{z,i+1}z_i})
$$

(5.21c)

$$
jk_{x,i}(A_{i+}e^{-jk_{z,i}z_i} + A_{i-}e^{jk_{z,i}z_i})
$$
$$
+j\kappa_{z,i}(B_{i+}e^{-j\kappa_{z,i}z_i} - B_{i-}e^{j\kappa_{z,i}z_i}) =
$$
$$
jk_{x,i+1}(A_{(i+1)+}e^{-jk_{z,i+1}z_i} + A_{(i+1)-}e^{jk_{z,i+1}z_i})
$$
$$
+j\kappa_{z,i+1}(B_{(i+1)+}e^{-j\kappa_{z,i+1}z_i} - B_{(i+1)-}e^{j\kappa_{z,i+1}z_i}) ,
$$

(5.21d)

which can be easily manipulated into a system of linear equations similar to 5.20.

At a fluid-solid interface, the normal stresses (equivalent to pressure in the fluid) and normal velocities are equal. The fluid layer cannot sustain shear stress, so the shear stress in the solid at the interface is zero. There is no equation relating the shear velocity at the interface. The resulting material states at an i-th layer of fluid and an $(i+1)$-th layer of solid are:

$$- p_i = \sigma_{z,i+1} \ , \ 0 = \sigma_{x,i+1} \ , \ v_i = v_{z,i+1} \ . \tag{5.22}$$

and the resulting equations will be:

$$j\omega\rho_i(A_{i+}e^{-jk_{z,i}z_i} + A_{i-}e^{jk_{z,i}z_i}) =$$

$$\frac{j}{\omega}((\lambda_{i+1}(-k_{x,i+1}^2 - k_{z,i+1}^2) - 2\mu_{i+1}k_{z,i+1}^2)(A_{(i+1)+}e^{-jk_{z,i+1}z_i} + A_{(i+1)-}e^{jk_{z,i+1}z_i}) \tag{5.23a}$$

$$+2\mu_{i+1}(\kappa_{x,i+1}\kappa_{z,i+1})(B_{(i+1)+}e^{-j\kappa_{z,i+1}z_i} - B_{(i+1)-}e^{j\kappa_{z,i+1}z_i}))$$

$$0 = 2\mu_{i+1}2k_{x,i+1}k_{z,i+1}(A_{(i+1)+}e^{-jk_{z,i+1}z_i} - A_{(i+1)-}e^{jk_{z,i+1}z_i})$$

$$+\mu_{i+1}(-\kappa_{x,i+1}^2 + \kappa_{z,i+1}^2)(B_{(i+1)+}e^{-j\kappa_{z,i+1}z_i} + B_{(i+1)-}e^{j\kappa_{z,i+1}z_i}) \tag{5.23b}$$

$$jk_{z,i}(-A_{i+}e^{-jk_{z,i}z_i} + A_{i-}e^{jk_{z,i}z_i}) =$$

$$jk_{z,i+1}(-A_{(i+1)+}e^{-jk_{z,i+1}z_i} + A_{(i+1)-}e^{jk_{z,i+1}z_i}) \tag{5.23c}$$

$$+j\kappa_{x,i+1}(B_{(i+1)+}e^{-j\kappa_{z,i+1}z_i} + B_{(i+1)-}e^{j\kappa_{z,i+1}z_i}) \ .$$

The interface between the first two layers involves the incoming wave with unit amplitude; the resulting equations differ from other interface equations in that they form an inhomogeneous system of equations due to the forcing of the incident wave. Only the reflected wave is an unknown coefficient in the first layer; the amplitude of the incident wave is a constant. For example, at a fluid-fluid interface between the incident layer and the second layer at $z = 0$, the resulting state equations will be:

$$- j\omega\rho_1 A_{1-} - (-j\omega\rho_i(A_{2+} + A_{2-})) = -(-j\omega\rho_1) \ , \tag{5.24}$$

$$jk_{z,1}A_{1-} - (-jk_{z,2}A_{2+} + jk_{z,2}A_{2-}) = -(-jk_{z,1}) \ . \tag{5.25}$$

On the final layer N (which must be a fluid in order to create a consistent system of linear equations), only the outgoing wave is allowed for. Because the fluid is semi-infinite, there will be no backward-traveling component.

The systems of equations for each interface can be summarized as the relationships between coefficients for each layer $[S_i]$, a vector of wave amplitudes $[P_i]$, and the resulting constants $[C_i]$ (which will be zero for all interfaces except the first one):

$$\left[S_i\right]\left[P_i\right] - \left[S_{i+1}\right]\left[P_{i+1}\right] = -\left[C_i\right] , \tag{5.26}$$

and these constituent parts for each layer can be combined into a multi-layer system of the form:

$$\begin{bmatrix} \left[S_1\right] & -\left[S_2\right] & & & \\ & \left[S_2\right] & -\left[S_3\right] & & \\ & & \left[S_3\right] & -\left[S_4\right] & \\ & & & \vdots & \\ & & & \left[S_{N-1}\right] & -\left[S_N\right] \end{bmatrix}\begin{bmatrix} \left[P_1\right] \\ \left[P_2\right] \\ \left[P_3\right] \\ \vdots \\ \left[P_N\right] \end{bmatrix} = \begin{bmatrix} -\left[C_1\right] \\ 0 \\ 0 \\ \vdots \\ 0 \end{bmatrix} , \tag{5.27}$$

$$\tag{5.28}$$

or, in simplified form:

$$\left[S\right]\left[P\right] = \left[C\right] , \tag{5.29}$$

and the resulting coefficients $[P]$ can be solved as:

$$\left[P\right] = \left[S\right]^{-1}\left[C\right] . \tag{5.30}$$

Once the coefficients in the system have been found, the amplitudes of each wave can be input into their respective equations, and the steady-state material states can

be found at all points z by summing the results from the forward- and backward-going waves in the appropriate layer. These material states are transfer functions between the state and the unit input wave amplitude; to obtain a transfer function for incoming pressure, the material states should be divided by $-j\omega\rho_1$.

Intensity in the system can be found from the stress and velocity (we will use the generic σ and v to correspond to either the longitudinal or shear values) at any state:

$$I(z) = \frac{1}{2}\Re(\sigma(z)v^*(z)) ,\tag{5.31}$$

where $v^*(z)$ is the complex conjugate of the velocity $v(z)$. In a fluid, the intensity in the i-th layer (the i subscript will be excluded from material properties and wavenumbers for clarity; note that z is a position) is:

$$
\begin{aligned}
I(z) = \frac{1}{2}\Re(pv_z^*) = &\frac{1}{2}\Re(-j\omega\rho(A_+e^{-jk_zz} + A_-e^{jk_zz})(jk_z(-A_+e^{-jk_zz} + A_-e^{jk_zz})^*) = \\
&\frac{1}{2}\Re(-j\omega\rho(A_+e^{-jk_zz} + A_-e^{jk_zz})(-jk_z^*(-A_+^*e^{jk_zz} + A_-^*e^{-jk_zz})) = \\
&\frac{\omega\rho}{2}\Re(-k_z^*(-A_+A_+^* - A_-A_+^*e^{2jk_zz} + A_+A_-^*e^{-2jk_zz} + A_-A_-^*)) .
\end{aligned}
\tag{5.32}
$$

The center two terms, which contain phase components, create a purely imaginary term that will not contribute to the intensity; therefore, intensity is constant across a fluid layer.

In a solid layer, the intensities in the longitudinal and shear waves both consists of 16 terms, obtained from multiplying the 4 terms constituting stress by the four terms constituting velocity. The longitudinal intensity is:

$$I_z(z) = \frac{1}{2}\Re(\frac{j}{\omega}$$

$$((\lambda(-k_x^2 - k_z^2) - 2\mu k_z^2)A_+ e^{-jk_z z} + 2\mu\kappa_x\kappa_z B_+ e^{-j\kappa_z z} +$$

$$(\lambda(-k_x^2 - k_z^2) - 2\mu k_z^2)A_- e^{jk_z z} - 2\mu\kappa_x\kappa_z B_- e^{j\kappa_z z})$$

$$(jk_z^* A_+^* e^{jk_z z} - j\kappa_x^* B_+^* e^{j\kappa_z z} - jk_z^* A_-^* e^{-jk_z z} - j\kappa_x^* B_-^* e^{-j\kappa_z z})) =$$

$$\frac{1}{2\omega}\Re(-k_z^*(\lambda(-k_x^2 - k_z^2) - 2\mu k_z^2)A_+ A_+^*$$

$$+\kappa_x^*(\lambda(-k_x^2 - k_z^2) - 2\mu k_z^2)\tilde{A_+}\tilde{B_+}^* e^{j(-k_z+\kappa_z)z}$$

$$+k_z^*(\lambda(-k_x^2 - k_z^2) - 2\mu k_z^2)\tilde{A_+}\tilde{A_-}^* e^{-2jk_z z}$$

$$+\kappa_x^*(\lambda(-k_x^2 - k_z^2) - 2\mu k_z^2)\tilde{A_+}\tilde{B_-}^* e^{j(-k_z-\kappa_z)z}$$

$$-k_z^* 2\mu\kappa_x\kappa_z\tilde{B_+}\tilde{A_+}^* e^{j(-\kappa_z+k_z)z}$$

$$+\kappa_x^* 2\mu\kappa_x\kappa_z\tilde{B_+}\tilde{B_+}^*$$

$$+k_z^* 2\mu\kappa_x\kappa_z\tilde{B_+}\tilde{A_-}^* e^{j(-\kappa_z-k_z)z}$$

$$+\kappa_x^* 2\mu\kappa_x\kappa_z\tilde{B_+}\tilde{B_-}^* e^{-2j\kappa_z z}$$

$$-k_z^*(\lambda(-k_x^2 - k_z^2) - 2\mu k_z^2)\tilde{A_-}\tilde{A_+}^* e^{2jk_z z}$$

$$+\kappa_x^*(\lambda(-k_x^2 - k_z^2) - 2\mu k_z^2)\tilde{A_-}\tilde{B_+}^* e^{j(k_z+\kappa_z)z}$$

$$+k_z^*(\lambda(-k_x^2 - k_z^2) - 2\mu k_z^2)\tilde{A_-}\tilde{A_-}^*$$

$$+\kappa_x^*(\lambda(-k_x^2 - k_z^2) - 2\mu k_z^2)\tilde{A_-}\tilde{B_-}^* e^{j(k_z-\kappa_z)z}$$

$$+k_z^* 2\mu\kappa_x\kappa_z\tilde{B_-}\tilde{A_+}^* e^{j(\kappa_z+k_z)z}$$

$$-\kappa_x^* 2\mu\kappa_x\kappa_z\tilde{B_-}\tilde{B_+}^* e^{2j\kappa_z z}$$

$$-k_z^* 2\mu\kappa_x\kappa_z\tilde{B_-}\tilde{A_-}^* e^{j(\kappa_z-k_z)z}$$

$$-\kappa_x^* 2\mu\kappa_x\kappa_z\tilde{B_-}\tilde{B_-}^*)\,,$$

$$(5.33)$$

while the shear intensity is:

$$I_x(z) = \frac{1}{2}\Re(\frac{j}{\omega}$$

$$(2\mu k_x k_z A_+ e^{-jk_z z} + \mu(-\kappa_x^2 + \kappa_z^2)B_+ e^{-j\kappa_z z}$$

$$-2\mu k_x k_z A_- e^{jk_z z} + \mu(-\kappa_x^2 + \kappa_z^2)B_- e^{j\kappa_z z})$$

$$(-jk_x^* A_+^* e^{jk_z z} - j\kappa_z^* B_+^* e^{j\kappa_z z}$$

$$-jk_x^* A_-^* e^{-jk_z z} + j\kappa_z^* B_-^* e^{-j\kappa_z z})) =$$

$$\frac{1}{2\omega}\Re($$

$$2\mu k_x^* k_x k_z A_+ A_+^*$$

$$-2\kappa_z^* \mu k_x k_z A_+ B_+^* e^{j(-k_z + \kappa_z)z}$$

$$+k_x^* 2\mu k_x k_z A_+ A_-^* e^{-2jk_z z}$$

$$-2\kappa_z^* \mu k_x k_z A_+ B_-^* e^{-j(k_z + \kappa_z)z}$$

$$+k_x^* \mu(-\kappa_x^2 + \kappa_z^2)B_+ A_+^* e^{j(-\kappa_z + k_z)z}$$

$$-\kappa_z^* \mu(-\kappa_x^2 + \kappa_z^2)B_+ B_+^*$$

$$+k_x^* \mu(-\kappa_x^2 + \kappa_z^2)B_+ A_-^* e^{-j(\kappa_z + k_z)z}$$

$$-\kappa_z^* \mu(-\kappa_x^2 + \kappa_z^2)B_+ B_-^* e^{-2j\kappa_z z}$$

$$-k_x^* 2\mu k_x k_z A_- A_+^* e^{2jk_z z}$$

$$+\kappa_z^* 2\mu k_x k_z A_- B_+^* e^{j(k_z + \kappa_z)z}$$

$$-k_x^* 2\mu k_x k_z A_- A_-^*$$

$$+\kappa_z^* 2\mu k_x k_z A_- B_-^* e^{j(k_z - \kappa_z)z}$$

$$+k_x^* \mu(-\kappa_x^2 + \kappa_z^2)B_- A_+^* e^{j(\kappa_z + k_z)z})$$

$$-\kappa_z^* \mu(-\kappa_x^2 + \kappa_z^2)B_- B_+^* e^{2j\kappa_z z})$$

$$+k_x^* \mu(-\kappa_x^2 + \kappa_z^2)B_- A_-^* e^{j(\kappa_z - k_z)z})$$

$$-\kappa_z^* \mu(-\kappa_x^2 + \kappa_z^2)B_- B_-^*) .$$

(5.34)

In a solid, The individual intensity terms are not constant across the layer; the cross-terms of the multiplication yield two position-dependent terms. However, the overall intensity $I = I_z + I_x$ in either direction will be constant in the layer.

Due to conservation of energy, the total intensity in each material layer is constant across the system, and equal to the outgoing intensity in the final layer I_N:

$$I_1 = I_2 = I_n = I_N \ . \tag{5.35}$$

While the intensity is constant with position across each layer, it will vary as a function of frequency and incident angle.

5.1.2 Model Verification

Initial verification of the model was performed by matching the results to closed-form fluid-fluid and fluid-solid interface solutions (which were presented in Chapter 3), which matched for all test cases, as seen in Figure 5.3.

Another test of the viability of this multi-layer model will be to compare the model results to other models for transmission through a simple plate. The transmission loss for a plate calculated using Bernoulli-Euler or Timoshenko beam theory relies on flexural wave motion in the beam; this motion is simulated in the wave potential model by coupling longitudinal and shear stresses. The transmission loss across the panel is:

$$T = 10 \log \left| 1 + \frac{Z \cos(\theta)}{2\rho c_{pl}} \right|^2 , \tag{5.36}$$

where the impedance Z_{pl} is calculated from the plate flexural wave velocity c_{pl}:

$$Z_{pl} = j\omega m_{pl} \left(1 - \left(\frac{c_{pl}}{v_{tr}} \right)^4 \right) . \tag{5.37}$$

For Bernoulli-Euler beam theory, the flexural wave velocity can be calculated using the mass per unit area m_{pl} and bending stiffness B_{pl}:
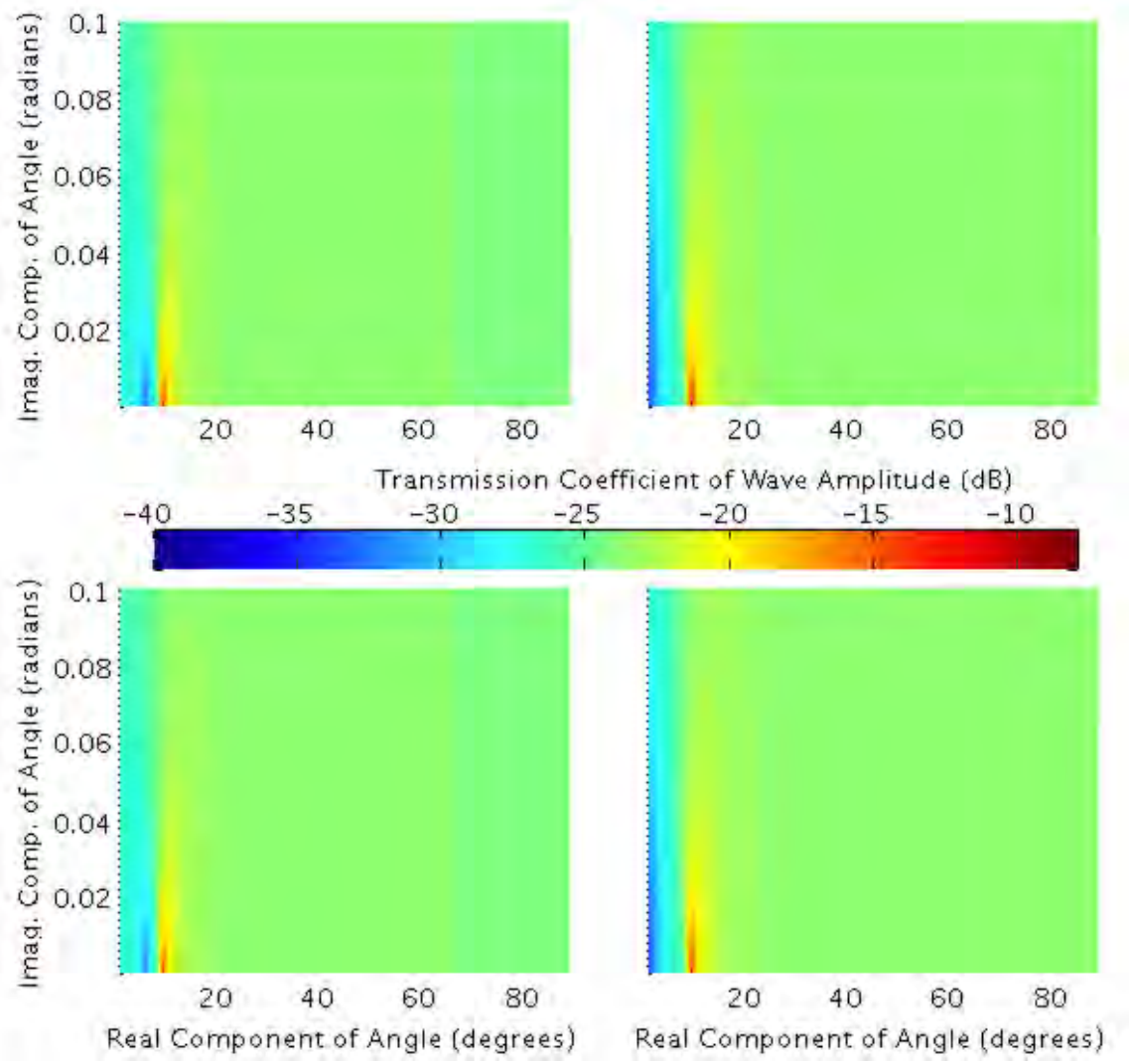
Figure 5.3. Comparison of the longitudinal (left) and shear (right) transmission coefficients for the fluid-solid interface obtained using the model in Chapter 3 (top row) compared to that using the multi-layer model (bottom row). That the plots along each column match is indicative of similar results between both models.

$$c_{pl,BE} = \sqrt{\omega}\sqrt[4]{\frac{B_{pl}}{m_{pl}}} \ . \tag{5.38}$$

Calculation of the Timoshenko beam theory transmission loss uses a different value of c_{pl}, which can be found (as detailed can be found in Graff's book [47]) by solving for

the positive root of the frequency equation of the governing equations for Timoshenko beam motion:

$$\frac{EI}{m_{pl}}\left(\frac{1}{c_{pl,T}}\right)^2 - \frac{I}{t}\left(1 + \frac{E}{G}\right)\omega^2\left(\frac{1}{c_{pl,T}}\right) - \omega^2 + \frac{\rho I}{Gt}\omega^4 = 0 \ , \qquad (5.39)$$

where E, G, and ρ are material properties of the plate, $I = t^3/12$ is the bending stiffness of the plate, and t is the thickness of the plate.

The plate modeled is a 3 centimeter thick steel plate, with an acoustic wave incident at a 30 degree angle. A plot showing the transmission loss variation with frequency for the wave potential model, the Bernoulli-Euler, and Timoshenko beam theories is shown in Figure 5.4. Differences in the transmission loss are due to the assumptions in each beam theory that limit the type of wave propagation in the beam. The wave potential model matches the prior theories well across most frequencies. The model estimates the transmission loss minima near 2,000 Hertz at a frequency above the Bernoulli-Euler beam theory model and below the Timoshenko theory model. Above the TL minima, the models agree to within several dB, with the wave potential model more closely matching the Timoshenko beam theory that would allow for less-constrained motion in the beam. Comparison to previously-verified TL calculations shows that the wave potential model is accurate for modeling acoustical propagation through materials. In addition to a single layer of the model, Figure 5.4 shows two additional lines, comprising the same panel modeled using two and three sublayers. These lines lie atop the single-layer model, showing the robustness of the model.

5.2 Wavenumber-Frequency Decomposition of Vibration

Wavenumber-frequency displays of vibration can be useful for visualizing wavetypes that can propagate through a material. By representing the vibration spectrum in the wavenumber domain as well as the frequency domain, properties of waves in the materal can be determined in a way that is not intuitive in the spatio-frequency domain.
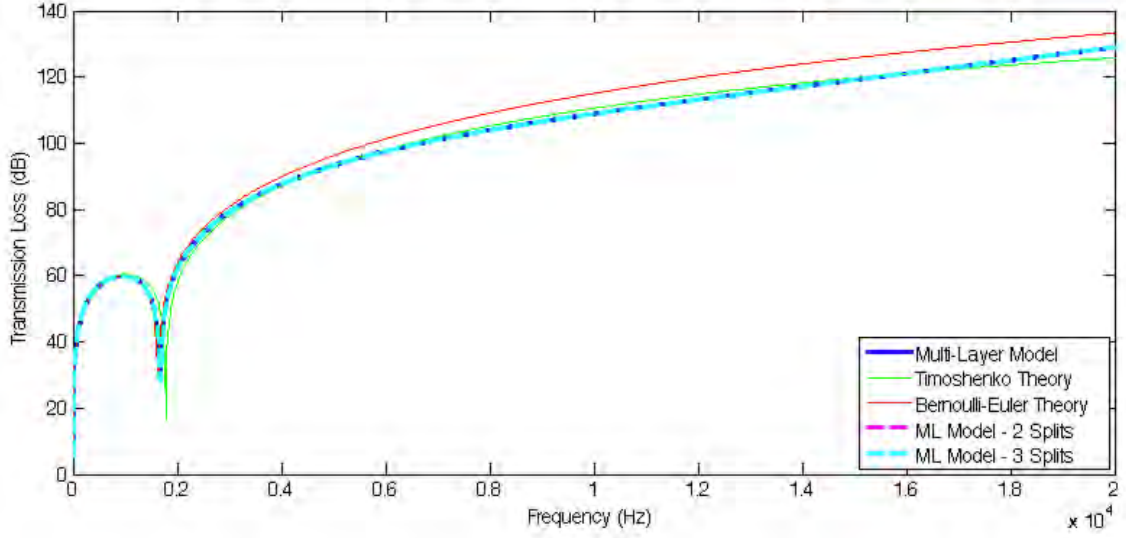
Figure 5.4.   Transmission loss comparison of Wave Potential, Bernoulli-Euler and Timoshenko theories, and a split Wave Potential model for 2 and 3 sublayers comprising the panel, for a 2cm panel with 30 degree acoustic incidence.

Spatio-frequency vibration data $V(x, f)$ along a straight line of length L, where x is the position along the line from 0 to L and f is the frequency, can be transformed into wavenumber-frequency data $V(k, f)$ by applying a Fourier transform to the spatial dimension. For the case of discrete data along equally-spaced acquisition points, x_i, limitations on the Fourier transform (as implemented using the Discrete Fourier Transform) are similar to those imposed in the case of time-sampled data being converted to frequency. The wavenumber resolution, Δk, of a set of discretely sampled points along a length L will be:

$$\Delta k = 2\pi \left(\frac{1}{L} \right), \tag{5.40}$$

and the maximum wavenumber k_{max} is proportional to the spatial sampling rate Δx:

$$k_{max} = 2\pi \frac{1}{\Delta x} . \tag{5.41}$$

The resulting wavenumber-frequency data allows analysis of vibration in a domain in which wavetypes are more clearly visible. High-amplitude features that lie along lines (either straight lines or curved) in the wavenumber-frequency domain are indicative of wavetypes that are propagating in the material. The phase speed of a feature located at (k, ω) is $c = \omega/k = 2\pi f/k$, and the group speed is $c_g = \delta\omega/\delta k$. For non-dispersive waves which have a speed invariant with frequency, including compressional and shear waves in a material, the phase speed will be constant and equal to the group speed, and the line will be straight in the wavenumber-frequency domain. For dispersive waves, such as flexural waves in a structure, the phase and group speed will vary with frequency and the resulting line representing the wave will have a variable slope. A wavetype feature originating from a $f \neq 0$ frequency indicates that the wave has a cut-on frequency; typically, these waves have geometry constraint along a non-propagation direction that must be fulfilled before the wave can propagate. Single points of high amplitude are indicative of standing waves and mode shapes in the system (although mode shapes made from reflecting wavetypes will show up as higher-amplitude sections of an existing wavetype feature). A schematic diagram showing these relationships on a simplified wavenumber-frequency plot is shown in Figure 5.5.

The wavenumber-frequency decomposition technique can be applied to both experimental measurements and theoretical models. We will use this technique in displaying the results of our model to more easily distinguish the characteristics in the system.

5.3 Modeling of Wave Propagation

Modeling several representative multi-layer systems can simulate the effects of coupling different materials together. Here, we build upon the fluid-fluid and fluid-solid interaction by adding additional complexities, including a single thick solid layer, the effects of higher-impedance bounding, and the effects of fluid gaps between the
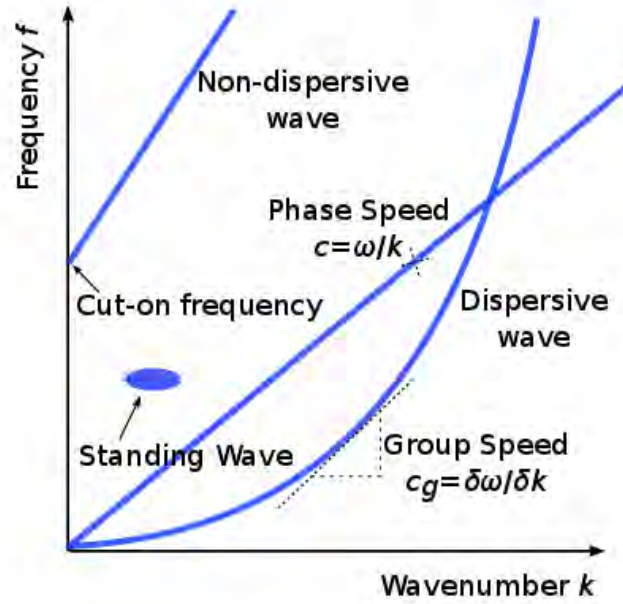
Figure 5.5. Wavenumber-frequency schematic showing phase speed, group speed, cut-on frequency relationshpis, and standing waves.

bounding and target layer. The model used here allows for visualization of energy within each layer, which is useful for judging the effectiveness of difference incident wave frequencies and incident angles.

Results from the model are a function of the frequency f and the incident angle of wave propagation, θ. The trace wavenumber on the surface k_x, which is constant throughout each layer of the material, can be related to the angle of incidence by:

$$k_x = k \sin(\theta) , \tag{5.42}$$

thus allowing for a method to input a surface wavenumber into the model using the angle θ. The use of the surface wavenumber as a reference is advantageous because vibration scans of the surface will more closely correlate in that case. The nature of surface wavenumbers is such that they will vary from 0 at normal incidence to the incident region material wavenumber k_0 at 90 degrees. Figure 5.6 shows equal-angle lines on a frequency-angle plot and on a wavenumber-frequency plot. Each angle

corresponds to a trace wave speed of $c/\sin(\theta)$; the decrease of trace wave speed with increasing angle can clearly be seen in the wavenumber-frequency plot.
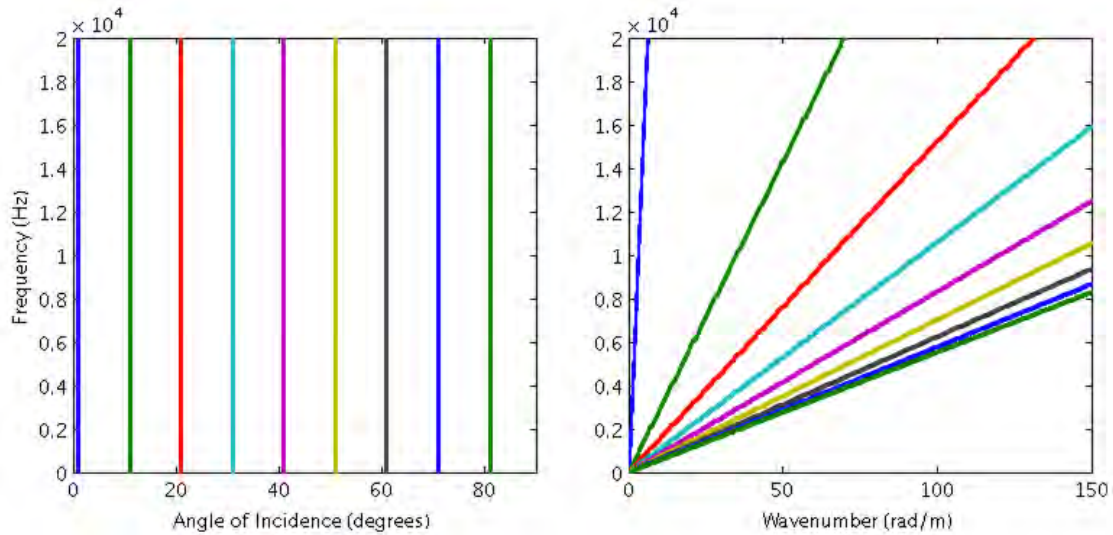
Figure 5.6.   Representation of incident angles of propagation in wavenumber-frequency plots. Lines of equal angle are shown in both the frequency-angle plot (left) and frequency-wavenumber plot (right).

Because the surface wavenumber is a function of frequency, the variables in the wavenumber frequency plot are not independent. This leads to compression of some regions in the plot, particularly at lower wavenumbers, where the entire angle is compressed into a much smaller section than the equivalent angle range at higher frequencies.

Several materials will be simulated in the model which are close analogues to the materials of interest in our testing and research. These properties were arrived at through a combination of existing data and wave propagation testing on the material (as detailed in Section 6), and are adjusted to yield properties that can be clearly distinguished in analysis when coupled to other materials.

Our primary concern is a low-wave speed material that approximates an energetic material. The material is question is a composite polymer of ammonium chloride in a hydroxyl-terminated polybutadiene (HTPB) resin binder, with the ammonium chlo-

ride consisting of 75% of the polymer by weight. Further details of the material will be given in Chapter 6; for our purposes now, we approximate the material properties as longitudinal and shear wave speeds of 700 and 500 meters per second, respectively, and a density of 1,200 kilograms per cubic meter. Because our primary goal is to excite this energetic material, results of the system will be shown in terms of energy deliverance (the sum of both longitudinal and shear intensity) into the target layer of surrogate material.

Polycarbonate is used as a bounding material, with a longitudinal wave speed of 1,300 meters per second, a shear wave speed of 900 meters per second, and a density of 1,000 kilograms per cubic meter. The fluid in the model is air, with a wave speed of 343 meters per second and a density of 1.2 kilograms per cubic meter. The properties used in all models are shown in Table 5.1.

Table 5.1.   Table of material properties used in multi-layer wave propagation model.

Material	Density ρ kg/m^3	Compressional wave speed c m/s	Shear wave speed b m/s
Air	1.2	343	N/A
Surrogate	1,200	700	500
Polycarbonate	1,000	1,300	900

To limit the effect of resonances in the layers, a 1% damping coefficient was added to the speed of sound of all enclosed layers.

The initial model we will consider is a fluid layer of 10 centimeters bounded by air on both sides, with the density and (longitudinal) wave speed of the fluid equal that of the energetic material. As in Chapter 3, this will serve as a simplified model of wave propagation to allow for ease of analysis. This same geometry with a solid layer of energetic material will also be considered. In the next model, a thin, 2 millimeter

layer of polycarbonate will border the energetic material to provide a high-impedance material barrier to wave transmission. Lastly, the effects of having a fluid gap in the system between the barrier and the energetic material will be explored by inserting a 1 centimeter gap of air into the system. A schematic of all the multi-layer geometries are shown in Figure 5.7.

Unless noted, the intensity transmission loss is plotted in the figures below:

$$TL = 10 \log\left(\frac{I_i(z)}{I_0}\right),$$ (5.43)

where z is typically the center of the i-th layer of interest (which is noted in each individual analysis).

The wavenumber-frequency characteristics of the intensity transmission loss at the center of the single fluid layer is shown in Figure 5.8. The region that comprises subsonic transmission in air (below 343 meters per second of wave speed) has been excluded because the resulting incident wave generated in this region would not propagate, and the reference intensity is too low to provide a physically relevant measure of transmision loss in the system.

Between the wave speed of the incident air and the lowest wave speed in the material of interest (in this case, the fluid wave speed of 700 meters per second), all waves into the material are subsonic; the region of high transmission loss here is indicative of very little energy propagating into the material. Although the temperature plot of the transmission loss is cut off at 100 dB to show detail in the supersonic region, the actual transmission loss in this region is around 200 dB, and will be of no use in energy transmission into the material.

At $k = 0$, which corresponds to normal incidence of sound, there are modes at integer multiples of 3,500 Hertz, corresponding to the half-wavelength distance of sound in the energetic material $f = nc_i/L_i$. With increasing wavenumber, the frequency of these features increase in frequency to account for the longer distance imposed on the half-wavelength. They eventually become waves moving almost entirely down the
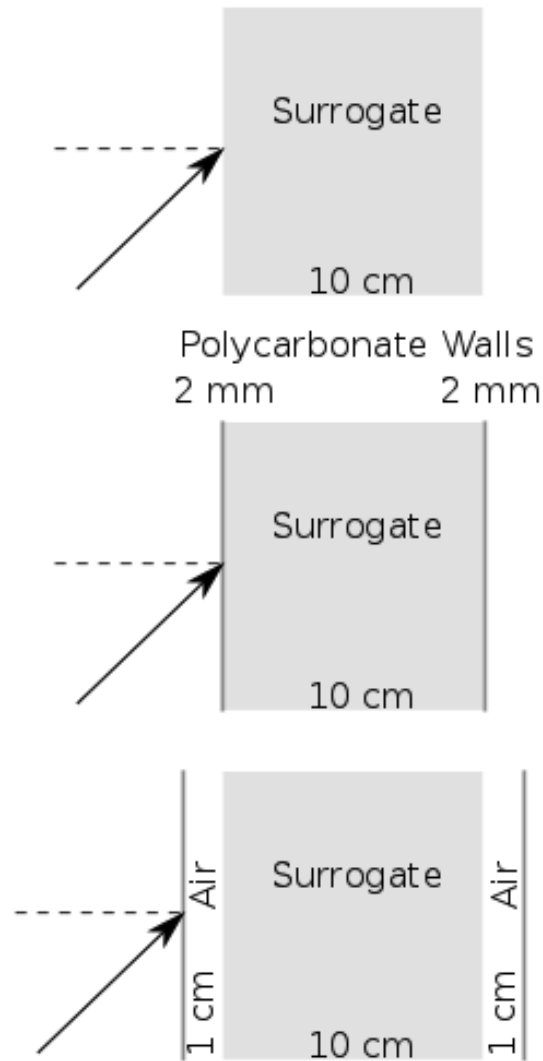
Figure 5.7. Geometries of modeled multi-layer systems. The top system consists of 10 centimeters of a surrogate layer (and will also be used for the single fluid case). The second system is the same surrogate layer enclosed by thin polycarbonate walls, to simulate a container. The lowest geometry is the same surrogate and walls, only with a 1 centimeter air gap between the surrogate and the polycarbonate wall.

waveguide of the center fluid layer, and the group speed of waves from this motion will approach the speed of longitudinal wave propagation in the material.
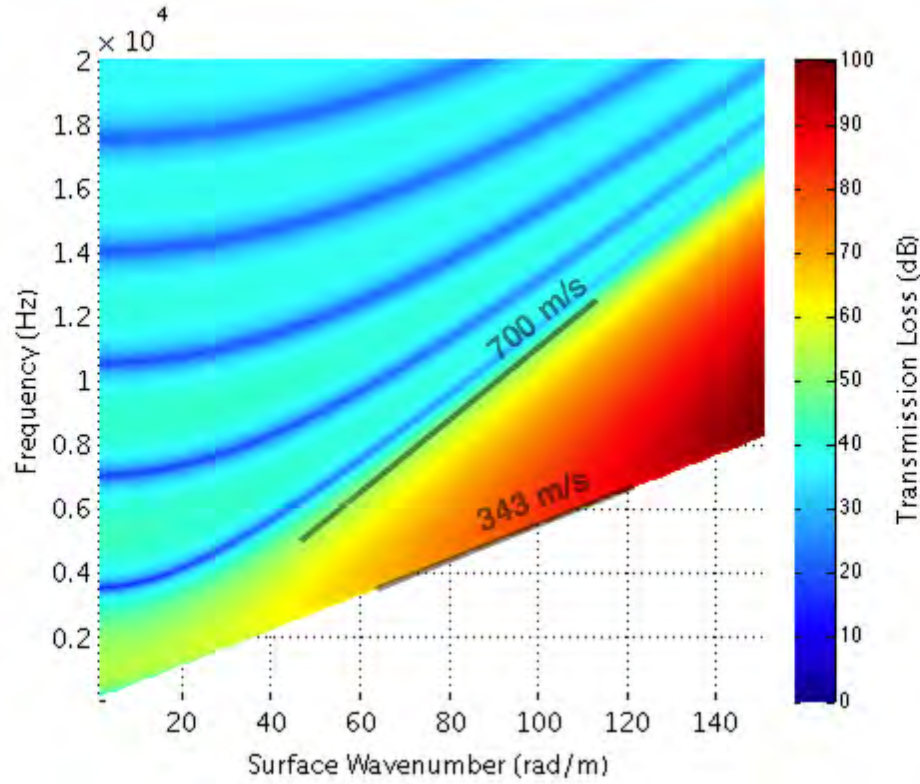
Figure 5.8. Intensity in middle layer of the fluid layer system, with the wave speed of the fluid (700 meters per second) and the wave speed in air (343 meters per second) indicated.

In the results for a solid layer of material, shown in Figure 5.9, the addition of shear waves to the system adds several features. The high-transmission loss region seen in the fluid layer modeled is not seen in this model; while there ought to be a high-transmission loss region below the shear speed in the material, that region is dominated by a flexural mode which decreases transmission loss. The effect of the shear wave on energy transmitted into the material is visible because of the features at integer multiples of 2,500 Hertz, which is the half wavelength frequency of materials traveling at 500 meters per second in a 10 centimeter gap.

Above normal incidence, the complex behavior introduced into the system by the addition is due to wave coupling phenomenon, wherein the shear waves that were not present in the fluid layer couple with the existing longitudinal waves to create Lamb
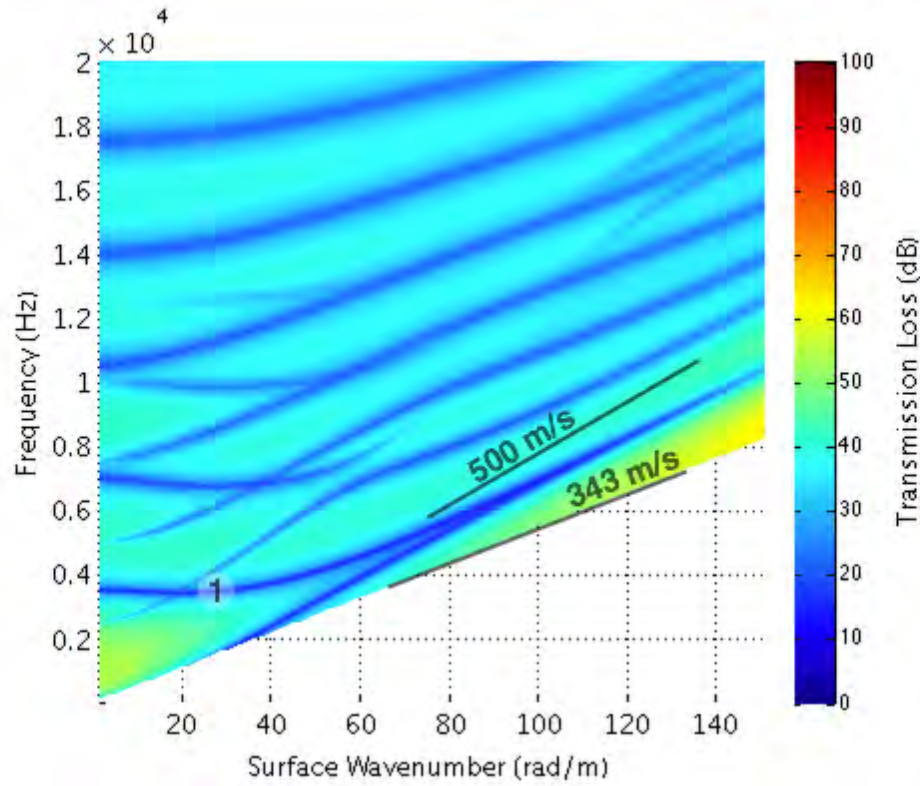
Figure 5.9. Intensity in the middle layer of the solid layer system, with relevent features and wave speeds labeled.

waves propagating within the solid layer. This causes behavior such as negative group speed seen in the curve beginning at 3,500 Hz (Feature 1). Auld [22] goes into this phenomenom more fully.

The addition of the polycarbonate bounding layer serves to lower the cut-on frequency and the frequencies for the equivalent wavetypes in the material, as shown in Figure 5.10. This is more evident at low frequencies, where the mode previously found at 3.5 kilohertz is now at 2.8 KHz. While the polycarbonate is a higher-impedance material, the layer is too thin to contribute additional stiffness, while increasing the length of the overall system in which waves can propagate.

The addition of an air gap between the two materials greatly increases transmission loss across all angles and wavenumbers, as seen in Figure 5.11. This shows the effects of decoupling the polycarbonate layers from the energetic; when the polycarbonate
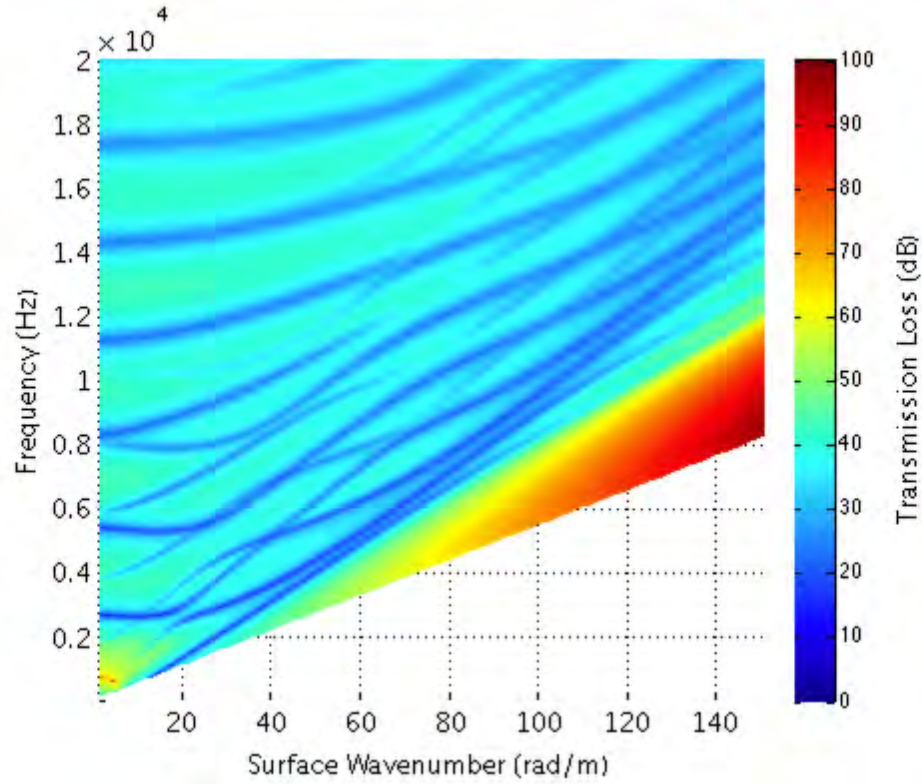
Figure 5.10. Intensity in the center of the middle (surrogate) layer of the plastic-bounded surrogate system.

was coupled to the solid layer as shown in Figure 5.10, the resulting system had little effect on the transmission loss. However, decoupling the layers greatly increases the transmission loss, as the polycarbonate layer induces a significant loss before transmission into the energetic layer.

5.3.1 The Effect of Evanescent Incident Waves

Evanescent waves were shown to be effective for overcoming subsonic transmission constraints in Chapter 3; their effect in multi-layer systems will allow for additional avenues of energy transmission.

In the model developed here, evanescent waves are represented by an adding an imaginary component to the trace surface wavenumber. Such a wavenumber will
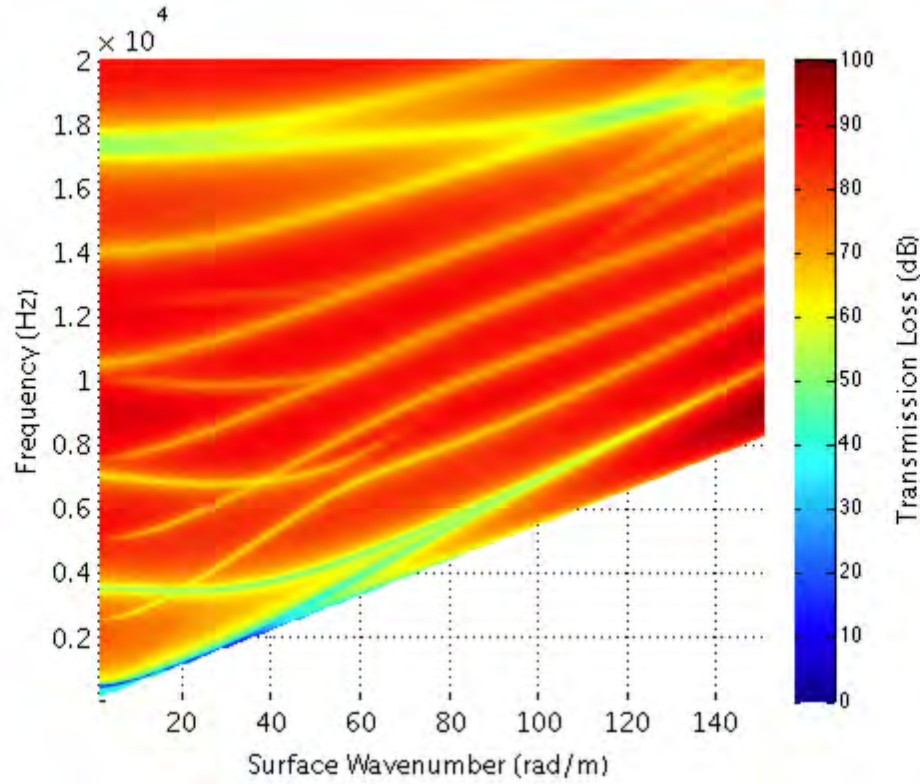
Figure 5.11. Intensity in the middle layer of middle (surrogate) layer of the plastic-bounded system with an air gap between the plastic and surrogate.

relate to a complex incident angle of propagation using our previous formulation in Equation 5.42.

The evanescent waves will not necessarily increase transmission into the system; rather, they will allow for additional transmission in subsonic (below the material wave speed) regions of the materials. For example, the intensity transmission loss due to a 0.1 complex component added to the single solid layer shown in Figure 5.9 is shown on the left side of Figure 5.12. The scale of this plot has been left at the same scale of the previous plot; the right plot shows the reduction in transmission loss between the transmission loss of the evanescent wave, TL_e compared to the transmission loss of the classical plane wave, TL_p, $TL_p - TL_e$. In such a case, a

positive value of TL reduction indicates an increase in energy transmission due to evanescent wave effects.

The use of evanescent waves causes increased energy transmission into the material, particularly at lower wave speeds, up to 20 dB. The evanescent wave also broadens the region of low transmission loss (Feature 2), increasing the width of the flexural mode components to lower the transmission loss in that region. There is an additional narrow high-transmission loss region that is below a surface wavenumber of 100 radians per meter (Feature 1); the cause of this is unknown.
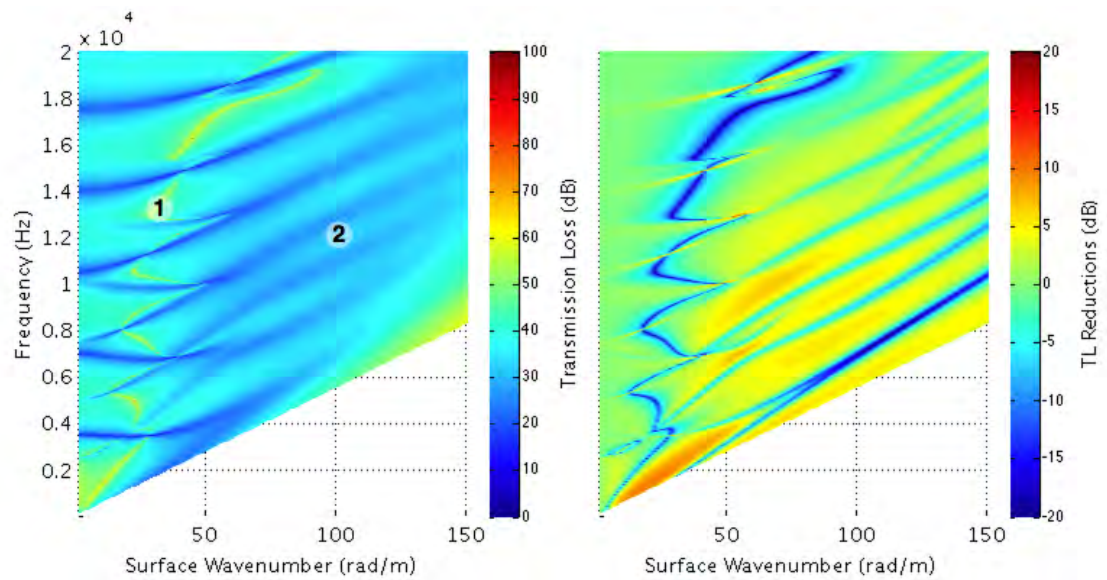
Figure 5.12. Intensity transmission loss in the center layer (left) and transmission loss improvement due to the evanescent wave (right) for the single-layer surrogate layer system with 0.1 radian evanescent component.

Evanescent waves ought to provide a method for propagating energy across a higher wave speed barrier region, particularly when the energetic behind the barrier has a lower wave speed. For example, a thick polycarbonate layer bonded to the surrogate material will provide significant energy loss in large regions of transmission. Such a system, with a 5 centimeter layer of polycarbonate in front of 10 centimeter layer of surrogate material, will show the contribution of evanescent waves. The in-

tensity transmission loss into the center of the polycarbonate and surrogate layers for non-evanescent wave transmission is shown in Figure 5.13. Intensity transmission in the system is dominated by the polycarbonate layer, causing subsonic transmission into the material below 700 meters per second. The addition of an evanescent component, shown in Figure 5.14, shows regions of improved and decreased intensity transmission loss. Figure 5.15 shows the TL reduction in the center layer due to the evanescent component. At higher wave speeds, there is a decrease in intensity transmission loss (Feature 1); this may be due to the increased decay of wave propagation limiting total intensity to the layer. At lower wave speeds (Feature 2), there is a slight increase in energy transmission (about 10 dB); this could be a region where the additional decay in the system is still greater than the effects of classical wave propagation, allowing a contribution from the evanescent wave.
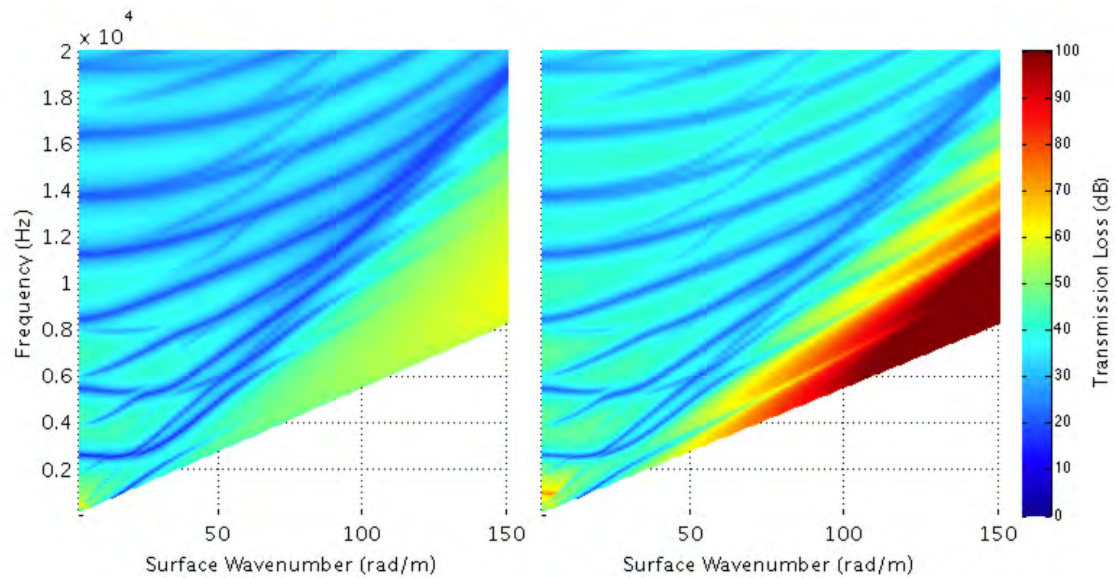
Figure 5.13. Intensity transmission loss for the polycarbonate-shielded surrogate system, consisting of polycarbonate in front of 10 centimeters of surrogate. Intensity transmission loss is shown in the polycarbonate layer (left) and the surrogate layer (right).
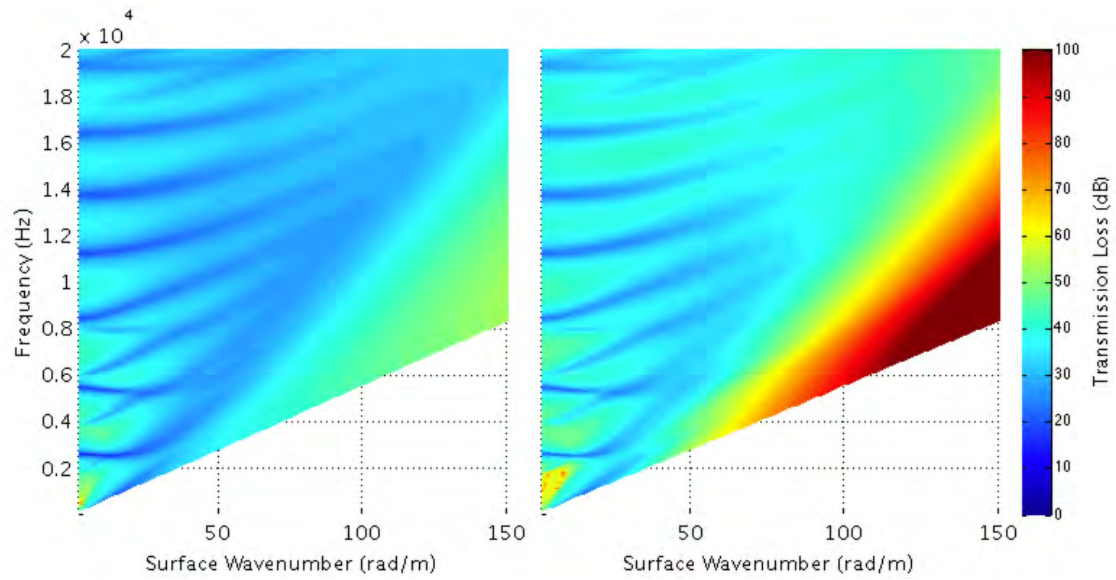
Figure 5.14.   Intensity transmission loss with evanescent component for the polycarbonate-shielded surrogate system, consisting of polycarbonate in front of 10 centimeters of surrogate. Intensity transmission loss is shown in the polycarbonate layer (left) and the surrogate layer (right).
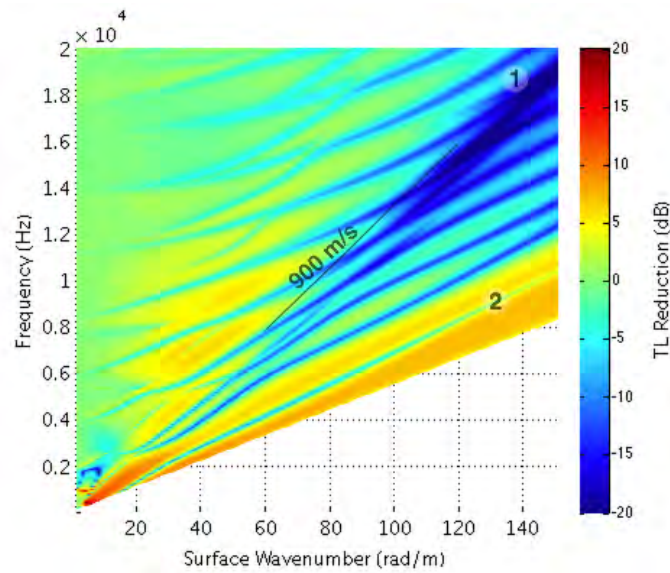
Figure 5.15.   Intensity transmission reduction in the surrogate layer for the polycarbonate-shielded surrogate system.

5.4   Conclusions

Wave propagation in multi-layer materials is governed by the coupled nature of the component layers. While previous models have developed transfer matrix and system of equation formulations for wave propagation through a multi-layer system, using wave potentials to calculate wave propagation has several advantages, such as allowing for evanescent incident waves and calculation of intensity in the system.

The wave potential model is generated for modeling wave propagation through each component layer of material, and equating the material states at each interface to solve for the appopriate wave properties. By replacing the transfer matrix-adapted method of wave propagation with a wave pontential method, the material states can be seen and intensity in each layer can be calculated. The model was verified by matching the results to existing closed-form solutions of panel vibration.

Several multi-layer materials were modeled, beginning with a single fluid or solid layer. A single layer exhibits both modes that are integer wavelengths of the layer's thickness, as well as coupled modes that are flexural or dilatational motion in the solid. When bounded by a higher-impedance material with low flexural stiffness, the materials couple together and produce a lower flexural stiffness multi-layer material. The removal of the coupling between the layers by adding a small fluid layer between each solid produces a much higher energy loss across the sample.

The model allows for evanescent incident waves; these effects are seen in the subsonic region of energy transmission, but have little or no effect in the classic regions. An evanescent waves can be used to propagate energy into the subsonic domain of a material, which can be useful to overcome a high-impedance barrier before a low-impedance target material. In cases where a particular frequency is desired that may impose limitations on classical wave propagation, the use of evanescent angles can add another parameter to overcome those limitations. However, the model constructed shows many regions of classical wave propagation that are as effective or better to excite material layers.

Because the evanescent waves offer improvement in sound transmission in the subsonic region, they pale in comparison to intensity transmission in supersonic regions.

CHAPTER 6. EXPERIMENTAL MEASUREMENTS OF WAVE PROPAGATION

The ability to quantify wave propagation characteristics in materials and structures experimentally depends significantly on conditions inherent to the testing setup. The resulting wave speeds found in testing can be used as inputs into the multi-layer model described in Chapter 5, as well as verification for that same model (particularly for geometry-based considerations such as flexural waves). Direct measurement of wave propagation is particularly important for inhomogeneous materials such as foams or aggregate composites, which may have wave properties that differ significantly from what the material properties would suggest. Furthermore, measurement of propagation characteristics will provide a better estimate of properties such as the speed of wave propagation, as well a geometry-specific properties such as cut-on frequencies or flexural wave speeds.

Vibration visualized in the wavenumber-frequency domain has distinct features that correspond to properties such as wave speeds, modes, and cut-on frequencies in a component. However, vibration measured during testing will be subject to conditions of the test, in particular excitation position and mounting conditions. Poor mounting conditions will mask the resulting waves in the system; while free-free simulated mounting commonly used in vibration classification of materials provide an ideal condition, they are insufficient in cases where the material needs support, and the mounting must be considered.

Another factor to be considered in experimental measurements is the effect of excitation locations, which may reveal different wavetypes in the system. For example, excitation at the end of a beam may excite longitudinal waves down the bar at the expense of transverse excitation. Care should be taken in designing an experiment to

assess the type of input and the effects it may have on the material. While the excitation type may be useful for illustrating different wavetypes, determining their relative susceptibility to excitation should only be performed with careful consideration of the system.

In this chapter, the effects of mounting conditions and excitation location are considered in the wave propagation classification of an unknown material.

6.1   Test Methodology

The motivation of this research is determining the wave propagation characteristics of a surrogate explosive material. Other methods of classification are being pursued simultaneously by Paripovic and Davies [48]; however, direct measurement of wave properties will be useful for modeling purposes. The material of interest is composite polymer composed of an ammonium chloride crystal in a hydroxyl-terminated polybutadiene (HTPB) resin binder, mixed together into a homogeneous mixture and poured into molds where they hardened to create a solid material. The surrogate is classified by the percentage of the crystal volume fraction, with 50% and 75% samples being used in our testing. The material was designed this way to simulate the dynamic properties of a commonly-used propellant while avoiding rapid energy release should the material be over-excited. In the propellant, the ammmonium chloride crystals would be replaced by ammonium perchloride.

The HTPB samples are cast into a mold 1.27 centimeters (0.5 inch) thick by 2.54 centimeters (1 inch) wide and 121.9 centimeters (48 inches) long. The properties of the HTPB surrogate vary significantly between the 50% and 75% samples. While the 50% samples are flexible and deform under their own weight, the 75% samples are more rigid but display significant granularity that is susceptible to breaking under deformation. Neither sample is rigid enough to stay intact if subject to its own weight, and cannot be machined or tapped for attachment of measuring devices. Figure 6.1 is a photo showing the textural differences between the two samples.
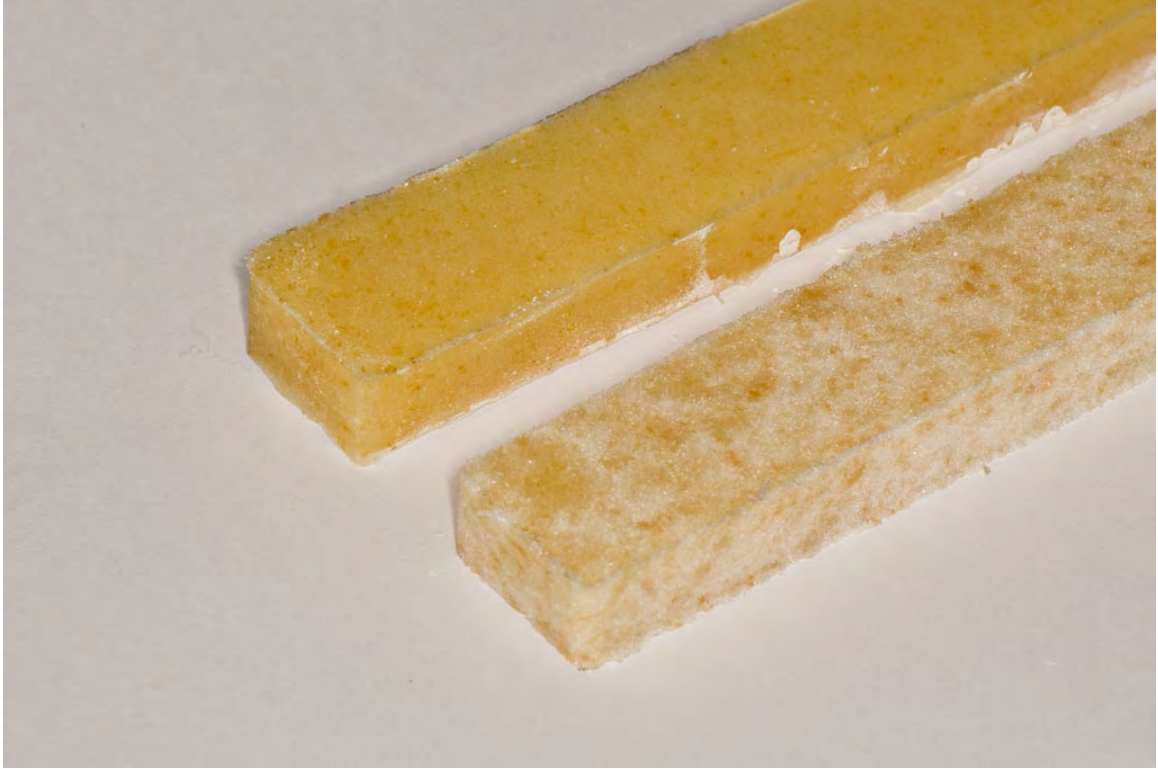
Figure 6.1. Surrogate samples tested. The 50% sample is on top, consisting of lower stiffness and a more elastic structure. The 75% sample is significantly more rigid, and would fracture under substantial deformation.

Because the surrogate samples are fragile and cannot support their own weight, mounting conditions are limited, especially those which provide a minimal support. In order to minimize the effects of the support, the samples were placed on Thinsulate layer that rested on a Quash foam board. A polycarbonate backing was also provided for comparison.

In addition to the HTPB surrogate material, polycarbonate was used as well to provide both a low-damping, thoroughly-quantified material. The polycarbonate is extruded as a thickness of 1.27 centimeters (0.5 inch) and cut to a width of 2.54 centimeters (1 inch) and a length of 121.9 centimeters (48 inches). The clear sides of polycarbonate were sanded to provide an opaque surface that could be measured by the laser vibrometer.

The density of polycarbonate is 1,200 kilograms per cubic meter (kg/m^3). The 50% surrogate material has a density of 1,156 kg/m^3, and the 75% has a density of 1,085 kg/m^3. While the ammonium chloride material has a higher density than the resin binder, manufacturing of the 75% samples produces air gaps that serve to reduce the density of the material. All of the foams have significantly lower densities than the test materials; the polyamide foam used in the minimal foam backing tests of polycarbonate had a density of 6.4 kg/m^3, while the Quash had a density of 32 kg/m^3. The volumetric density of the Thinsulate could not be found; however, the sheet material weighs 150 kg/m^2 for a sheet approximately 6 millimeters thick when uncompressed, which would yield a density of 9 kg/m^3. The density of the tested materials is at least 30 times greater than the backing material, and typically more.

The polycarbonate samples were tested in three mounting conditions. The first was a hung condition, wherein the polycarbonate rod was suspended from a hook by a string drilled into the far edge of the sample. This represents a minimal boundary condition, and is commonly used in modal testing of structures. The polycarbonte was then supported using the minimal foam support, as well as a more thorough foam backing consisting of the Thinsulate, the same method used for the surrogate sample.

The excitation locations used in testing were a side excitation, wherein the actuator was mounted within an inch from the end of the largest side (on the width-by-length plane). The other excitation location was on the end (on the width-by-height plane). The actuator-transducer stack was attached to the polycarbonate through a screw stud that was tapped into the polycarbonate. To attach the stack to the HTPB surrogate samples, an accelerometer mount was glued to the sample surface by using epoxy; these mounts have a screw stud that allows the stack to be attached.

The samples were excited using a PCB 712A02 stack actuator equipped with a 100 gram add-on mass. The actuator has an excitation range of 150 to 5000 Hertz, and was driven with a white-noise signal generated by a General Radio 1381 Random-Noise Generator, running at a brandwith of 5 KHz. The signal was amplifed with a QSC 1100 audio amplifier.
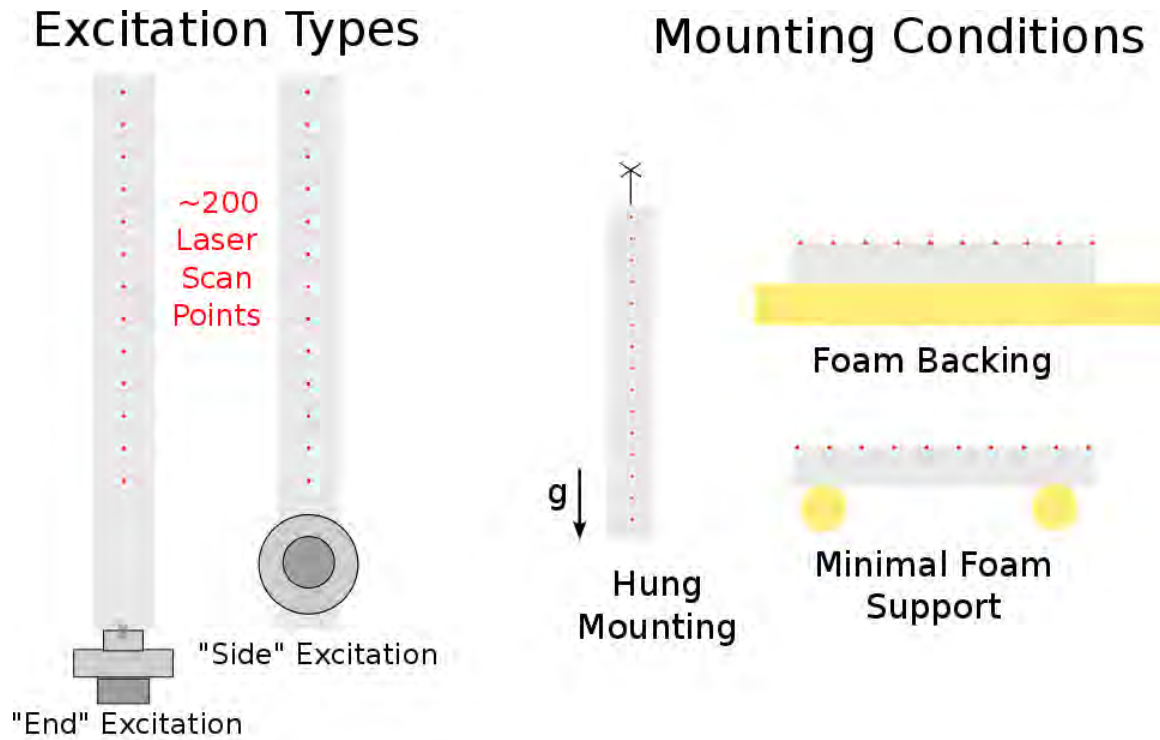
Figure 6.2. Schematic of experimental measurements of polycarbonate beam. Two excitation locations were used, with the "side" excitation being along the same plane as the measurement, and the "end" excitation being at the far end of the polycarbonate bar. For mounting, the beam was hung (suspended from the end above a fixed point), given a foam backing that covered the entirety of the surface opposite the measurement, and positioned with minimal support that allowed for reduced contact with the sample.

Force into the sample was measured using a PCB 208A02 force transducer, which is an ICP-powered transducer with a nominal output of 50 millivolts per Newton. This transducer was positioned between the actuator and the sample.

Vibration measurement along the sample was performed using a Polytec PSV-400 scanning laser vibrometer. The vibrometer measured a 4 KHz bandwidth with 1,600 points across that frequency range for a frequency resolution of 2.5 Hz. The number of points tested varied during particular tests; as least 200 points where measured

across every sample. Testing spanned over most of the bar, with a scan length of approximately 1.15 meters in length.

All data analysis was performed using the data acquisition system of the Polytec PSV-400; both the vibration signal and the force transducer signal were windowed using a Hann window and recorded for 50 averages with 50 percent overlap. The H1 estimator was calculated between the vibration and force transducer signal, and is the displayed signal on all results. A list of all the equipment used in testing is shown in Table 6.1.

Wave propagation measurement consists of exciting vibration in the sample using the actuator, then measuring the resulting vibration at number of points along the length of the sample. Conversion of the frequency-position data into wavenumber-frequency data enables visualization of wavetypes in the system. Wavenumber analysis was performed using the method specified in Section 5.2. A table showing experimental parameters and the resulting frequency and wavenumber resolution is shown in Table 6.2.

Use of the Discrete Fourier Transform results in a two-sided wavenumber-frequency plot, with information in both the negative and positive wavenumber values. This information is indicative of waves traveling in different directions in the system; the direction is relative to the numbering of points in the system, and in all cases points are numbered with low numbers being closer to the excitation location, and waves traveling away from the sensor have negative wavenumbers. Because waves traveling towards the excitation source can only be formed by reflection in the material, the difference between the features on the positive and negative sides of the wavenumber spectrum is due to reflection characteristics in the system.

Table 6.1. Equipment used in wave propagation testing.

Equipment Type	Manufacturer	Model Number	Serial Number
Stack Actuator	PCB	712A02	666
White Noise Source	General Radio	1381	41259
Amplifier	QSC	1100	109298995
Force Transducer	PCB	208A02	9273
Scanning Vibrometer	Polytec	PSV-400	0111421
Data Acquisition	Polytec	PSV-400	0111891-01

Table 6.2. Parameters for sample testing.

Parameter	Quantity	Units
Measurement Distance	1.15	meters
Spatial Resolution	5.6	millimeters
Wavenumber Resolution	5.3	rad/m
Sampling Frequency	4,000	Hz
Frequency Resolution	2.5	Hz
Number of Averages	50	N/A
Overlap	50	percent

6.2   Results

6.2.1   Polycarbonate Tests

The results of the tests on the polycarbonate samples are shown in Figure 6.3. In the foam mounting condition, the vibration spectrum of the side excitation is dominated by a dispersive wave with a phase speed between 114 meters per second

at 500 Hz and 332 meters per second at 3,500 Hz. This is most likely a flexural wave with deformation normal to the direction of measurement and excitation.

The end excitation shows the flexural wave, but has an equally prominent non-dispersive wave of about 1,700 meters per second. This would most likely be the longitudinal wave speed in the beam; from the material properties, polycarbonate is estimated to have a bulk longitudinal wave speed of 1,696 meters per second. While the flexural wave is seen in the end excitation, another slightly faster dispersive wave can also be observed. This is the transverse flexural wave causing motion in the normal direction. The wave speed of a flexural wave is proportional to the fourth-root of the bending moment; the approximate ratio between the two speeds, across all frequencies, is 1.7, which is nearly equal to the ratio of normal to transverse bending moment, $8^{1/4} = 1.68$.

Both the foam backed and minimal foam support mounting conditions show the same trend with regards to excitation as the hung mounting, wherein the side excitation exhibits a strong flexural wave and the end excitation shows multiple wavetypes. In contrast to the hung mounting condition, though, both foam mounting conditions exhibit the transverse flexural wave more prominently. This would indicate that the normal flexural wave is limited by the mounting conditions, while the transverse flexural motion is not subject to the same constraint. The additional prominence of the transverse wave in the minimal foam support condition is due to the decreased restriction in motion of the minimal foam support compared to the foam backing. The structure of the non-dispersive wave shown in the minimal foam supports with end excitation suggests that there are two waves with this high wave speed; however, it is unknown what this wavetype could be, and could be additional energy of the longitudinal wavetype.

The tests above show the results of changing the excitation location and mounting type on a polycarbonate beam. The hung mounting provides the best excitation of the wavetypes typically normal to the direction of measurements, but the foam mountings reveal additional wavetypes such as the transverse flexural wave. Similarly, the end
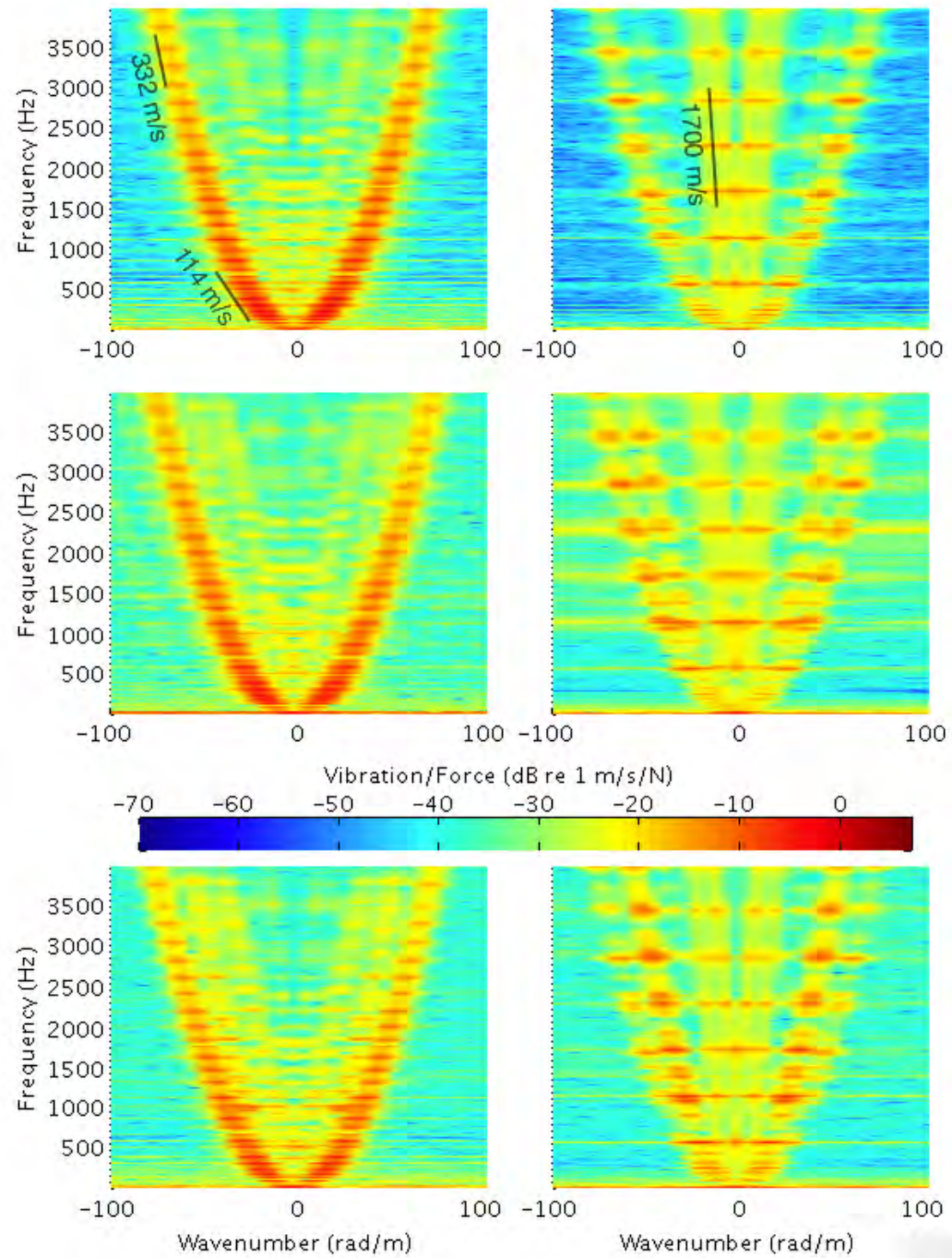
Figure 6.3. Polycarbonate vibration for the hung (top row), foam backing (middle row) and minimal foam support (bottom row) conditions, with side (left plots) and end (right plots) shown. Significant features have been labeled on the plot.

excitation shows several low level wavetypes, while a side excitation is dominated by a single wave.

6.2.2 Surrogate Tests

The surrogate sample differs from the polycarbonate in that the material properties were not known, making estimation and suggestion of what the visualize wavetypes might be attributed to in the material difficult. Therefore, the polycarbonate results will provide a template for which to interpret the features found in the surrogate tests.

Figure 6.4 shows the vibration spectra for the 50% surrogate sample tests. The sample exhibits a one-sided wave spectrum; this is indicative of a lack of reflection in the material due to damping. The effects of the damping can also be seen in the frequency response; there is substantially less energy above 2,500 Hertz. The lack of energy at higher frequencies can be seen in Figure 6.5, which shows the position-dependent frequency response. The higher-frequency components decay quickly, and therefore contribute less energy in the wavenumber domain.

The 50% surrogate test results show three waves of interest. Two dispersive waves in the same normal-transverse pair seen in the polycarbonate have maximum speeds (before damping becomes significant) of 95 and 113 meters per second, are visible in the end excitation, while only the slower wave can be seen in the side excitation. The non-dispersive wave has a wave speed of 244 meters per second, which is significantly slower than the sound speed in air. Therefore, the 50% surrogate material would have no subsonic range of acoustical transmission.

When the surrogate sample is backed with the higher-impedance material, such as in the results for the test on the polycarbonate-backed surrogate, the resulting vibration information is indiscernable; coupling with the polycarbonate obscures all pertinent wave information. This would suggest that the foam mounting is sufficiently
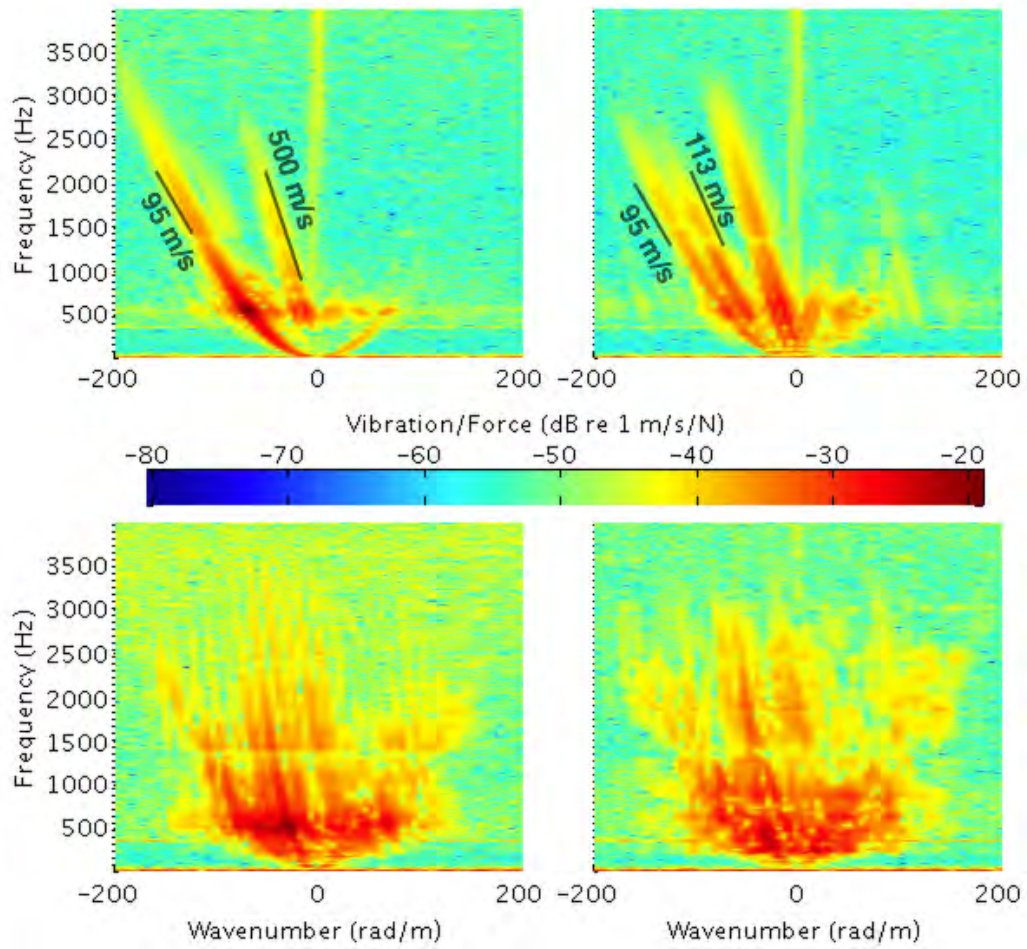
Figure 6.4.   50 % surrogate vibration for foam backing (top) and polycarbonate backing (bottom) conditions, with side (left plots) and end (right plots) shown. Significant features have been labeled on the plot.

low impedence to allow for wave propagation in the materials, but the polycarbonate material is too stiff and restrains motion.

For the results of the 75% surrogate sample tests, shown in Figure 6.6, the foam mounting conditions have much less prevalent damping than that which produced a one-sided wavenumber-frequency profile for the 50% surrogate sample. While the forward-going (left) side of the plot is slightly higher in amplitude, there is still significant energy traveling in the opposite direction through the bar. Two waves
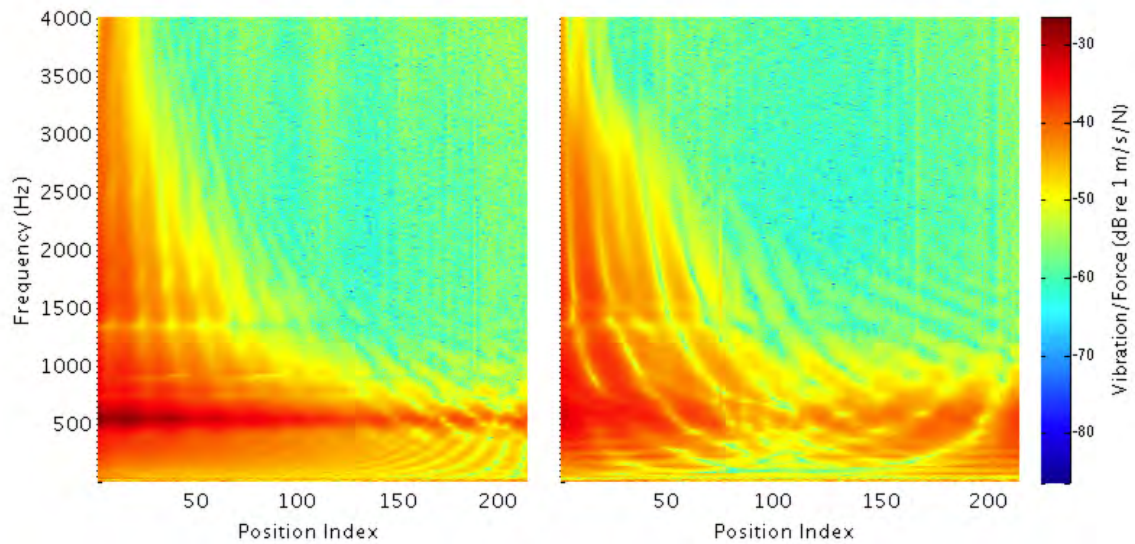
Figure 6.5. Vibration in the position-frequency domain for the 50% surrogate sample, comparing the foam mounting condition for side (left) and end (right) excitation.

are evident in testing: a dispersive wave with a speed of about 400 meters per second above 1000 Hertz, and a non-dispersive wave with a speed of about 900 meters per second. While the transverse flexural wave could possibly be seen as the higher component of the main dispersive wave, it is not discernable enough from the primary flexural wave to ascertain its properties.

The polycarbonate-backed tests of the 75% sample have more wave components than the foam mounting condition and the primary wavetypes are harder to discern; however, wave components can more clearly be seen than in the equivalent test of the 50% polycarbonate-mounted sample. This suggests that the additional stiffness in the 75% sample makes it more suitable for higher-impedance mounting.

6.3   Conclusions

Testing of material samples yielded different results depending on the excitation location and mounting of the specimen. Certain excitation effects, such as the promi-
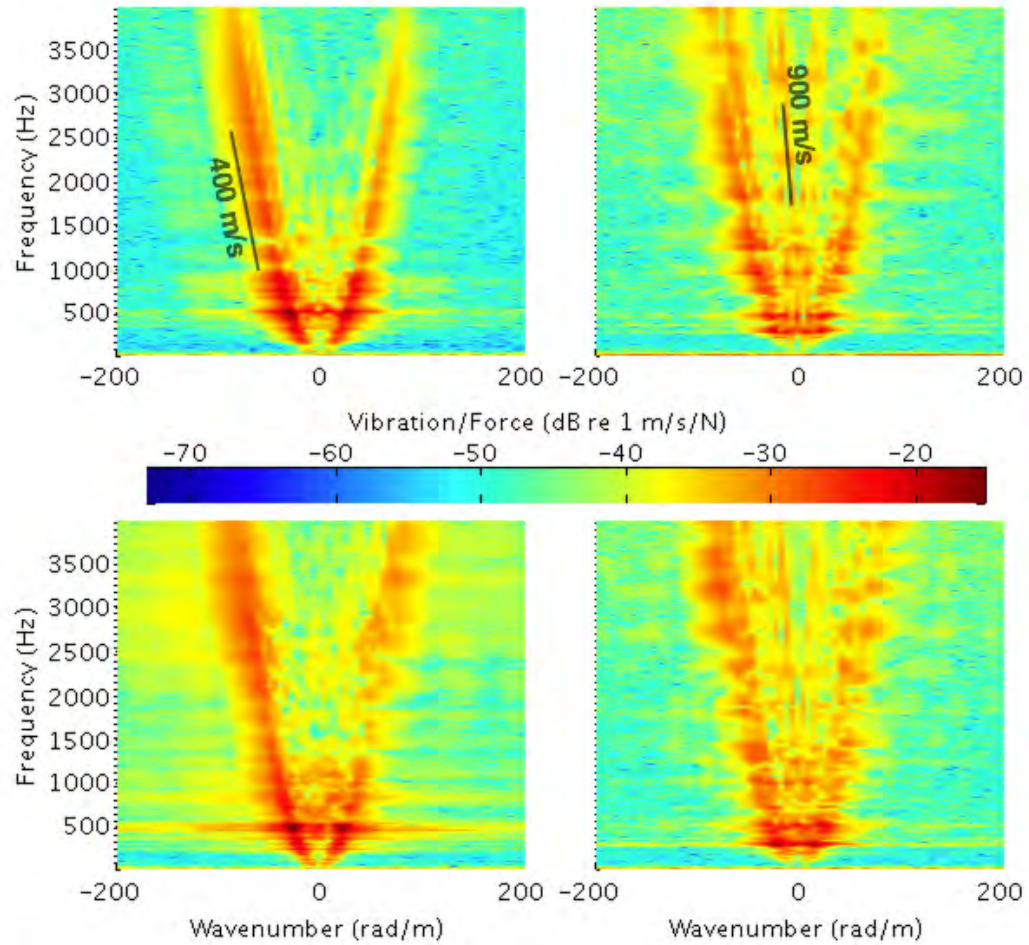
Figure 6.6. 75 % surrogate vibration for foam backing (top) and polycarbonate backing (bottom) conditions, with side (left plots) and end (right plots) shown. Significant features have been labeled on the plot.

nence of flexural waves in the side excitation of the beam, are obvious. However, a substantial difference can be seen in the testing in testing of different excitation types and mountings.

In the polycarbonate samples, the hung mounting showed fewer wavetypes than either of the foam mounting conditions, due to the lack of restriction on the normal vibration in the system. Under higher impedance mountings, the end excitation showed significantly more wavetypes than the side excitation, even some that ought

to be inherent to the side excitation (such as torsional waves). While waves relating to the flexural motion of the beam and longitudinal vibration can easily be discerned, there does not appear to be any features corresponding to shear waves through the beam.

The surrogate material samples showed similar characteristics to the polycarbonate samples; flexural waves and longitudinal waves can be seen in each sample, although the 75% flexural waves may be too close in speed to separate into normal and transverse components. The 50% sample showed significant damping, evident as a one-sided wavenumber-frequency plot that shows little energy propagation towards the excitation location. The addition of a stiff polycarbonate backing made a substantial difference in the 50% sample case, masking all relevant wavetypes that can clearly be seen in the foam-mounted condition. These effects were not seen in the stiffer 75% sample, which is of equivalent density but much stiffer.

The testing here will serve as a suitable assessment of wave propagation properties in the unknown surrogate material; of particular note is that the 50% material has a longitudinal wave speed slower than that in air. The subsonic region of wave propagation in air will therefore be supersonic in the surrogate, minimizing the effects of evanescent waves in air in its excitation.

CHAPTER 7. CONCLUSIONS

Evanescent waves have been shown to improve sound transmission across the fluid-solid interface in subsonic regions of sound transmission. By using evanescent waves to reduce the refraction effects associated with large impedance difference boundaries, energy can be transmitted into solid materials via acoustical excitation that could not be propagated in homogeneous energy transmission.

Evanescent waves are modeled for this work by using a complex angle of propagation, which produces a wavetype that decays normal to the direction of propagation; this wavetype obeys the wave equation, and the complex angle can be easily integrated into existing models of fluid-solid interaction. While such waves would be difficult to generate in open space, the pressure and velocity of such a wave can be generated over a limited space along a surface. The complex angle of propagation, then, is a convenient way to model evanescent waves in classical wave-propagation equations.

The use of evanescent waves has no beneficial effect on pressure transmission levels, and will make no contribution to transmission in supersonic regions of fluid-solid interaction. However, the intensity propagation into a material, particularly in the subsonic region, is improved by the use of incident evanescent waves. At incident angles above the critical angle, where the trace wave speed on the surface falls below that of the material's, refraction typically causes no energy propagation into the material. The refraction of an evanescent wave does not approach the critical angle, instead increasing the decay rate of the wave into the material. However, in appropriate situations, such a decay is worthwhile to allow for propagation into the material.

Monopoles have significant evanescent components, which can allow for experimental verification of evanescent wave effects. The decay of a monopole's trace

pressure distribution on a surface decays with distance, allowing for a controlled ratio of evanescent to homogeneous wave components. Using a monopole source to judge the effects of evanescent waves on fluid-solid energy transmission showed significant contributions of the evanescent waves to the total sound power transmitted into the solid.

While the sound field of an evanescent wave would be difficult to generate, approximating the boundary conditions seen by an evanescent wave on the fluid-solid interaction surface would allow for proper transmission into the material. A key effect of the evanescent wave is the phase difference between pressure and velocity; while classical plane waves have in-phase pressure and velocity, the addition of the complex angle component increases the phase difference towards a 90 degree difference.

Approximating the pressure distributions made by evanescent waves on the surface of a material can be done using multiple simple sources. A formulation is developed that computes the amplitude and phase of a monopole or dipole array based on a least-squares approximation of an ideal pressure distribution on a surface. An exploration of the parameters of the model shows a heavy emphasis on the incident angle and frequency of the incident wave being modeled, with angle of incidence being a particularly important parameter. The geometry of the source array shows a proportional relationship between the standoff of the array and the required length to obtain a good fit, with increased trace wavelength requiring additional source length.

Attempting to approximate evanescent waves on the surface showed a significant reduction in the quality of the surface velocity fit, most likely due to the phase difference between the pressure and velocity that cannot be easily duplicated using simple sources. Both monopole and dipole sources were found to model the desired incident waves equally well; however, the dipole sources will have less efficiency due to the reduced radiation efficiency of the dipole.

Modeling wave propagation through multi-layer materials allows for visualization of the effects of geometry and material coupling on the overall vibration characteristics of the system. A model for propagation was formulated using the wave potentials in

each layer, equating the material states at each interface to calculate the amplitudes of each potential. The use of wave potentials allows for inter-layer state calculation, as well as intensity calculation to allow for measurement of energy propagation into the material.

Simulations from the wave potential model show significant effects of flexural and dilatational waves, which are formed from coupling of the longitudinal and shear waves. The addition of thin, high-impedance materials as barrier materials will not affect these waves, as their increased material stiffness is overcome by the low flexural stiffness resulting from their narrow width. However, removing the direct coupling between the barrier and energetic layer causes an increase in energy transmission loss into the material. The effect of evanescent waves are put into context by the multi-layer model; while they can increase energy transmission in the subsonic region, other avenues of energy propagation may provide higher energy transmission, particularly in lower-speed materials.

Measuring wavetypes experimentally is a process dependent on careful planning in order to properly visualize the wavetypes in the system. The effects of mounting conditions and excitation location are shown through the classification of wave propagation through a polycarbonate beam and two beams of surrogate materials with unknown material properties. The polycarbonate beam's properties are well-known, and using the resulting vibration will allow a basis to analyze the properties of the unknown surrogate materials. For the mounting conditions, the effects of any restriction to the vibration caused by mounting can be seen in the relationship between the two flexural waves in the material; while the normal motion dominates in the low-impedance hung condition, the effects of the transverse wave on normal motion can be clearly under additional constraint. When lower-impedance materials are mounted to materials with significantly higher impedances, the wavetypes inherent to the material are masked by the effects of the mounting materials. The excitation location plays a significant role on waves excited in the material; while the side excitation

provides energy into the normal flexural wavetype, exciting the materials from the end provides excitation of significantly more wavetypes.

The research presented here provides an initial foray into the theory and practical considerations of evanescent wave propagation into multi-layer materials. Continuing upon this research will allow for more precise applications of the theory, especially in regards to development of novel excitation and detection technologies.

7.1   Future Work

Of primary concern to the research undertaken is the generation of evanescent waves; while the theory presented here is promising, an experimental method to generate such waves will be vital for exciting the systems of interest. The generation of controlled pressure distributions would, on their own, be a significant area of research, it would also allow for experimental measurements of evanescent wave propagation across fluid-solid boundaries.

The model developed here allows for angular variation of source output, as shown with the dipole model. Modifying the model slightly would allow for arbitrary angular variation of each source, and characteristics representing real speakers could be input and calculated. Additional modifications to the geometry can also be made from the limited one explored here; for example; changing the angle of the linear source array, or using creative geometries. Optimization of geometry for a desired pressure distribution would be a more complex task, possibly requiring the use of a genetic algorithm. Additional optimization of the model may also be possible by varying the angle of each speaker in the array. The final goal of this modeling would be the creation and experimental verification of an array. While other researchers have developed arrays that allow for phase variation of the sources, the use of a 64-channel output would be the basis of a setup that varies both amplitude and phase for a given frequency.

Understanding of the dynamic effects of the pressure-velocity phase difference, which is an inherent property in evanescent waves, may provide additional avenues of energy transmission. In the absence of evanescent wave generation, additional methods to excite evanescent wave motion through vibrating a structure may also be explored, such as monopole-like radiation in a solid resulting from a point excitation.

Once evanescent waves can be found to be generated in a solid, the effects of wavetypes with concentrated energy in a particular frequency should be explored, particularly in multi-layer materials. For example, the ability to excite resonance in a low-impedance interior layer bounded by high-impedance materials would show the transmission effects of evanescent waves and their ability to probe materials.

A detailed accounting for test methodology of unknown materials should be developed, taking into account the excitation type and mounting condition. Several wavetypes of interest, such as the shear wave and dilatational waves, could not be seen or verified during our tests; a novel excitation or measurement method may allow for their detection and classification.

LIST OF REFERENCES

LIST OF REFERENCES

[1] T.H. Gan, D.A. Hutchins, D.R. Billson, and D.W. Schindel. The use of broadband acoustic transducers and pulse-compression techniques for air-coupled ultrasonic imaging. *Ultrasonics*, 39(3):181 – 194, 2001.

[2] J.D. Fox, B.T. Khuri-Yakub, and G.S. Kino. High-frequency acoustic wave measurements in air. *1983 Ultrasonics Symposium*, p.p. 581 – 584, 1983.

[3] L.M. Brekhovskikh. *Waves in layered media*. Academic Press, 1960.

[4] A.A. Hudimac. Ray theory solution for the sound intensity in water due to a point source above it. *The Journal of the Acoustical Society of America*, 29:916, 1957.

[5] M.S. Weinstein and A.G. Henney. Wave solution for air-to-water sound transmission. *The Journal of the Acoustical Society of America*, 37:899, 1965.

[6] R.W. Young. Sound pressure in water from a source in air and vice versa. *The Journal of the Acoustical Society of America*, 53:1708, 1973.

[7] W.C. Meecham. High-frequency model for sound transmission from an airborne source into the ocean. *The Journal of the Acoustical Society of America*, 60(2):339–342, 1976.

[8] Y.I. Bobrovnitskii. On the energy flow in evanescent waves. *Journal of Sound and Vibration*, 152(1):175 – 176, 1992.

[9] Y.I. Bobrovnitskii. Author's reply. *Journal of Sound and Vibration*, 161(2):357, 1993.

[10] O.A. Godin. Transmission of low-frequency sound through the water-to-air interface. *Acoustical Physics*, 53:305–312, 2007.

[11] O.A. Godin. Sound transmission through waterair interfaces: new insights into an old problem. *Contemporary Physics*, 49(2):105–123, 2008.

[12] O.A. Godin. Anomalous transparency of water-air interface for low-frequency sound. *Physics Review Letters*, 97:164301, Oct 2006.

[13] O.A. Godin. Low-frequency sound transmission through a gas–solid interface. *The Journal of the Acoustical Society of America*, 129(2), 2011.

[14] B.E. McDonald and D.C. Calvo. Enhanced sound transmission from water to air at low frequencies. *The Journal of the Acoustical Society of America*, 122:3159, 2007.

[15] D. Calvo, M. Nicholas, and G. Orris. Experimental verification of enhanced sound transmission from water to air at low frequencies. *International Congress on Acoustics 2013 Montreal*, v. 19, p. 070074, Montreal, Canada, 2013. Acoustical Society of America.

[16] F. Fahy and P. Gardonio. *Sound and Structural Vibration: Radiation, Transmission and Response.* Elsevier/Academic Press, 2007.

[17] C.M. Park, J.J. Park, S.H. Lee, Y.M. Seo, C.K. Kim, and S.H. Lee. Amplification of acoustic evanescent waves using metamaterial slabs. *Physics Review Letters*, 107:194301, Nov 2011.

[18] M. Ambati, N. Fang, C. Sun, and X. Zhang. Surface resonant states and superlensing in acoustic metamaterials. *Physical Review B*, 75(19):195447, 2007.

[19] D.L. Folds and C.D. Loggins. Transmission and reflection of ultrasonic waves in layered media. *Acoustical Society of America Journal*, 62, November 1977.

[20] A.D. Pierce. *Acoustics: An Introduction to Its Physical Principles and Applications.* Acoustical Society of America, 1989.

[21] B. Brouard, D. Lafarge, and J.F. Allard. A general method of modelling sound propagation in layered media. *Journal of Sound and Vibration*, 183(1):129 – 142, 1995.

[22] B.A. Auld. *Acoustic Fields and Waves in Solids.* Robert E. Krieger Publishing Company, 1990.

[23] G. Maidanik and J. Dickey. A boundary that sustains a negligible specular reflection coefficient over a wide frequency band. *The Journal of the Acoustical Society of America*, 107(3):1103–1110, 2000.

[24] D.J. Mead. Wave propagation and natural modes in periodic systems: I. mono-coupled systems. *Journal of Sound and Vibration*, 40(1):1 – 18, 1975.

[25] D.J. Mead. Wave propagation and natural modes in periodic systems: Ii. multi-coupled systems, with and without damping. *Journal of Sound and Vibration*, 40(1):19 – 39, 1975.

[26] A.M. Jessop and J.S. Bolton. Calculation of pressure distribution of the interior acoustical mode of deformed tires. *INTER-NOISE and NOISE-CON Congress and Conference Proceedings*, v. 2011, p.p. 1034–1042, Portland, Oregon, USA, 2011. Institute of Noise Control Engineering.

[27] JK Thompson. Plane wave resonance in the tire air cavity as a vehicle interior noise source. *Tire Science and Technology*, 23(1):2–10, 1995.

[28] K. Grosh and E.G. Williams. Complex wave-number decomposition of structural vibrations. *The Journal of the Acoustical Society of America*, 93(2):836–848, 1993.

[29] T.J. Wahl and J.S. Bolton. The application of the wigner distribution to the identification of structure-borne noise components. *Journal of Sound and Vibration*, 163(1):101 – 122, 1993.

[30] J.S. Bolton, H.J. Song, and Y.K. Kim. The wave number decomposition approach to the analysis of tire vibration. *Publications of the Ray W. Herrick Laboratories*, 1(12), 1998.

[31] J.S. Bolton and Y.J. Kim. Wave number domain representation of tire vibration. Technical Report 14, Ray W. Herrick Laboratories, Purdue University, 2000.

[32] Y.J. Kim and J.S. Bolton. Effects of rotation on the dynamics of a circular cylindrical shell with application to tire vibration. *Journal of Sound and Vibration*, 275(35):605 – 621, 2004.

[33] B.D. Van Veen and K.M. Buckley. Beamforming: A versatile approach to spatial filtering. *ASSP Magazine, IEEE*, 5(2):4–24, 1988.

[34] H. Cox, R. Zeskind, and M. Owen. Robust adaptive beamforming. *IEEE Transactions on Acoustics, Speech and Signal Processing*, 35(10):1365–1376, 1987.

[35] A.J. Berkhout, D. de Vries, and P. Vogel. Acoustic control by wave field synthesis. *The Journal of the Acoustical Society of America*, 93(5):2764–2778, 1993.

[36] J.H. Chang, J.W. Choi, and Y.H. Kim. A plane wave generation method by wave number domain point focusing. *The Journal of the Acoustical Society of America*, 128(5):2758–2767, 2010.

[37] D.A. Russell, J.P. Titlow, and Y. Bemmen. Acoustic monopoles, dipoles, and quadrupoles: An experiment revisited. *American Journal of Physics*, 67:660, 1999.

[38] J.S. Bolton, B.K. Gardner, and T.A. Beauvilain. Sound cancellation by the use of secondary multipoles. *The Journal of the Acoustical Society of America*, 98(4):2343–2362, 1995.

[39] T.A. Beauvilain, J.S. Bolton, and B.K. Gardner. Sound cancellation by the use of secondary multipoles: Experiments. *The Journal of the Acoustical Society of America*, 107(3):1189–1202, 2000.

[40] J. Ahrens and S. Spors. An analytical approach to sound field reproduction using circular and spherical loudspeaker distributions. *Acta Acustica united with Acustica*, 94(6):988–999, 2008.

[41] J. Ahrens and S. Spors. An analytical approach to local sound field synthesis using linear arrays of loudspeakers. *Proceedings of the 36th International Congress on Acoustics, Speech, and Signal Processing (ICASSP2011)*, p.p. 65–68, Prague, Czech Republic, May 2011.

[42] O. Robin, A. Berry, S. Moreau, and R. Dia. Reproduction of random acoustic pressure fields using wave field synthesis and planar holography. *Proceedings of the Acoustics 2012 Congress*, Nantes, France, April 2012.

[43] Z. Wang and S.F. Wu. Helmholtz equation–least-squares method for reconstructing the acoustic pressure field. *The Journal of the Acoustical Society of America*, 102:2020, 1997.

[44] S.F. Wu and J. Yu. Reconstructing interior acoustic pressure fields via helmholtz equation least-squares method. *The Journal of the Acoustical Society of America*, 104(4):2054–2060, 1998.

[45] S.F. Wu and X. Zhao. Combined helmholtz equation–least squares method for reconstructing acoustic radiation from arbitrarily shaped objects. *The Journal of the Acoustical Society of America*, 112(1):179–188, 2002.

[46] O. Kirkeby and P.A. Nelson. Reproduction of plane wave sound fields. *The Journal of the Acoustical Society of America*, 94(5):2992–3000, 1993.

[47] K.F. Graff. *Wave Motion in Elastic Solids*. Dover Publications, 1975.

[48] J. Paripovic and P. Davies. Identification of the dynamic behavior of surrogate explosive materials. *ASME 2013 International Design Engineering Technical Conferences and Computers and Information in Engineering Conference*, number DETC2013-12755, Portland, Oregon, USA, August 2013.

APPENDICES

APPENDIX A: MULTI-LAYER PROPAGATION CODE

The code below comprises the multi-layer propagation model developed in Chapter 5. An input structure, comprising the geometry and material properties of the system, are input along with the frequency, incident angle, and requested positions for state calculation. The resulting output is the wave potential amplitudes, the states, and resulting matrices used in calculation.

The bulk of the code comprises formation of the multi-layer matrix, accounting for different interface types and material states, along with separate code for the first and last layers (which contain distinct wave features). This code calls on the code in Appendix B for calculation of postion-based states.

```
function [PSI,states,A,B] = MLpot(input,f,inc_angle,x_req,makeplot)



if nargin<5
    makeplot = 'n';
end

%computes potential amplitudes (vector PSI) for multi-layer fluid-solid
%system by constructing a linear system of equations governing the
%interactions of each layer

%OUTPUTS:
% PSI - structure with of potential amplitudes and angles
    % contains 1 incident reflected amplitude, 1 transmitted output,
    % and 4 states for each interior layer
% states - structure of position-dependent material states
% A - constructed matrix
% B - constructed matrix in A*PSI=B
```

```
%INPUTS:
% input - structure describing materials and geometry of system
%    input structure (each layer is an input in a row vector):
%       type - 'f' for fluid and 's' for solid
%       c - longitudinal wavespeed
%       b - shear wavespeed ('0' in fluids)
%       rho - density
%       L - length ('Inf' on both sides)
% f - frequency
% inc_angle - complex incident angle (degrees)
% x_req - position vector for state calculation
% makeplot - make plot of position-dependent states


%convert incident angle to radians
inc_theta = real(inc_angle)*pi/180+1i*imag(inc_angle);
omega = 2*pi * f; %frequency in radians


PSI.f = f;


N = length(input.type); %number of layers


PSI_N = 4*(N-2)+2; %number of points in PSI


%calculate lambda and mu for each layer
mu = input.b.^2.*input.rho;
lambda = input.c.^2.*input.rho-2*mu;


kt = omega/input.c(1)*sin(inc_theta); %trace wavelength - constant!
```

```matlab
% material wavenumbers
k = omega./input.c;
kappa = omega./input.b;


%calculate normal wavenumbers and angles in each layer
k_z = sqrt(k.^2-kt^2);
kappa_z = sqrt(kappa.^2-kt^2); %check for imaginary numbers!!
theta = asin(kt./k);
gamma = asin(kt./kappa);


PSI.theta = theta;
PSI.gamma = gamma;


%calculate z-coordinates of each interface
z=zeros(1,N-1);
z(1) = 0;
for i = 2:N-1;
    z(i) = sum(input.L(2:i));
end
PSI.z = z;


% PSI format:
% (1) incoming long
% (2) incoming shear
% (3) outgoing long
% (4) outgoing shear


A = zeros(PSI_N,PSI_N);
```

```
B = zeros(PSI_N,1);


%construct matrix
%first layer - incident fluid only, only part with positive B input
if input.type(2) == 'f' %only pressure, velocity conditions
    %pressure condition
    A(1,1) = -1i*omega*input.rho(1)*exp(1i*k_z(1)*-z(1)); %reflected long
    A(1,2) = -1*(-1i*omega*input.rho(2)...
        *exp(-1i*k_z(2)*-z(1))); %transmitted long
    %A(1,4) components in "if" loop below
    B(1) = -1*(-1i*omega*input.rho(1)*exp(-1i*k_z(1)*-z(1))); %INCOMING WAVE


    %velocity condition
    A(2,1) = 1i*k(1)*cos(theta(1))*exp(1i*k_z(1)*-z(1)); %reflected long
    A(2,2) = -1*(-1i*k(2)*cos(theta(2))*...
        exp(-1i*k_z(2)*-z(1))); %transmitted long
    %A(2,4) component in "if" loop below
    B(2) = -1*(-1i*k(1)*cos(theta(1))*...
        exp(-1i*k_z(1)*-z(1))); %INCOMING WAVE


    if N>2 %incorporate back-going waves
        A(1,4) = -1*(-1i*omega*input.rho(2)*...
            exp(1i*k_z(2)*-z(1))); %back-going long (in second fluid) %for N>2


        A(2,4) = -1*(1i*k(2)*cos(theta(2))*...
            exp(1i*k_z(2)*-z(1))); %back-going long for N>2


        %set shear coefficients of layer 2 to zero
        A(3,3) = 1;
```

```
        A(4,5) = 1;

    end


    r = 5;


elseif input.type(2) =='s'


    %stress relationship
    A(1,1) = -1*(  -1i * omega * input.rho(1) *...
        exp(1i * -z(1) * k_z(1) )); %reflected long
    A(1,2) = ( lambda(2) * -k(2)^2 + 2 * mu(2) * -k(2)^2 *...
        cos(theta(2))^2)/(-1i*omega)*exp(-1i*-z(1)*k_z(2) ); %transmitted long
    A(1,3) = (2*mu(2)*kappa(2)^2*cos(gamma(2))*sin(gamma(2)))/...
        (-1i*omega)*exp(-1i*-z(1)*kappa_z(2) );  %transmitted shear


    B(1) = (-1i*omega*input.rho(1))*exp(-1i*z(1)*k_z(1)); %INCOMING WAVE


    %shear relationship
    A(2,1) = 0; %reflected long
    A(2,2) = mu(2)*(2*k(2)^2*cos(theta(2))*sin(theta(2)))/...
        (-1i*omega)*exp(-1i*-z(1)*k_z(2)); %transmitted long
    A(2,3) = mu(2)*(-kappa(2)^2*(sin(gamma(2))^2-cos(gamma(2))^2))/...
        (-1i*omega)*exp(-1i*-z(1)*kappa_z(2)); %transmitted shear


    B(2) = 0; %INCOMING WAVE


    %normal velocity
    A(3,1) =    -1*(  1i*k(1)*cos(theta(1))*exp( 1i*-z(1)*k_z(1)));
    A(3,2) = -1i*k(2)*cos(theta(2))*exp(-1i*-z(1)*k_z(2));
```

```
A(3,3) = 1i*kappa(2)*sin(gamma(2))*exp(-1i*-z(1)*kappa_z(2));


B(3) = -1i*k(1)*cos(theta(1))*exp(-1i*-z(1)*k_z(1));


if N>2 %add backward-going components

    A(1,4) = (lambda(2)* -k(2)^2 + 2*mu(2)*-k(2)^2*...
        cos(theta(2))^2)/(-1i*omega)*...
        exp(1i*-z(1)*k_z(2));%back-going long
    A(1,5) = (2*mu(2)*-kappa(2)^2*cos(gamma(2))*sin(gamma(2)))/...
        (-1i*omega)*exp(1i*-z(1)*kappa_z(2));%back-going shear


    A(2,4) = mu(2)*(2*-k(2)^2*cos(theta(2))*sin(theta(2)))/...
        (-1i*omega)*exp(1i*-z(1)*k_z(2));%back-going long
    A(2,5) = mu(2)*(-kappa(2)^2*(sin(gamma(2))^2-cos(gamma(2))^2))/...
        (-1i*omega)*exp(1i*-z(1)*kappa_z(2));%back-going shear


    A(3,4) = 1i*k(2)*cos(theta(2))*...
        exp(1i*z(1)*k_z(2));%back-going long
    A(3,5) = 1i*kappa(2)*sin(gamma(2))*...
        exp(1i*-z(1)*kappa_z(2));%back-going shear


elseif N==2 %zero out backward components
    A(4,4) = 1;
    A(5,5) = 1;


    B(4) = 0;
    B(5) = 0;
```

```
        end


    r = 4;
end


if N>3
    for i = 3:N-1


        if input.type(i) == 'f'
            if input.type(i-1)=='f'
                %pressure
                A(r,1+4*(i-3)+1) = -1i*omega*input.rho(i-1) *...
                    exp(- 1i * k_z(i-1) * -z(i-1)); %incoming long
                A(r,1+4*(i-3)+3) = -1i*omega*input.rho(i-1) *...
                    exp( 1i * k_z(i-1) * -z(i-1)); %reflected long
                A(r,1+4*(i-2)+1) = -1*(-1i*omega*input.rho(i) * ...
                    exp(- 1i * k_z(i) * -z(i-1))); %transmitted long
                A(r,1+4*(i-2)+3) = -1*(-1i*omega*input.rho(i) * ...
                    exp( 1i * k_z(i) * -z(i-1))); %back-going long


                %velocity
                A(r+1,1+4*(i-3)+1) = -k(i-1)*cos(theta(i-1))*...
                    exp(-1i * k_z(i-1) * -z(i-1));
                A(r+1,1+4*(i-3)+3) =  k(i-1)*cos(theta(i-1))*...
                    exp(1i * k_z(i-1) * -z(i-1));
                A(r+1,1+4*(i-2)+1) =  -1*(-k(i)*cos(theta(i))*...
                    exp(-1i * k_z(i) * -z(i-1)));
                A(r+1,1+4*(i-2)+3) =  -1*(k(i)*cos(theta(i))*...
                    exp(1i * k_z(i) * -z(i-1)));
```

```
        %shear components in i-th fluid = 0
        A(r+2,1+4*(i-2)+2) = 1;
        A(r+3,1+4*(i-2)+4) = 1;


        r = r+4;


elseif input.type(i-1)=='s' %solid-fluid interface


        %normal stress
        A(r,1+4*(i-3)+1) = (lambda(i-1)*-k(i-1)^2+...
            2*mu(i-1)*-k(i-1)^2*cos(theta(i-1))^2)*...
            exp(-1i*k_z(i-1)*-z(i-1))/(-1i*omega);
        A(r,1+4*(i-3)+2) = 2*mu(i-1)*kappa(i-1)^2*...
            cos(gamma(i-1))*sin(gamma(i-1))*...
            exp(-1i*kappa_z(i-1)*-z(i-1))/(-1i*omega);
        A(r,1+4*(i-3)+3) = (lambda(i-1)*-k(i-1)^2+...
            2*mu(i-1)*-k(i-1)^2*cos(theta(i-1))^2)*...
            exp(1i*k_z(i-1)*-z(i-1))/(-1i*omega);
        A(r,1+4*(i-3)+4) = 2*mu(i-1)*-kappa(i-1)^2*...
            cos(gamma(i-1))*sin(gamma(i-1))*...
            exp(1i*kappa_z(i-1)*-z(i-1))/(-1i*omega);
        A(r,1+4*(i-2)+1) = -1*(-1i*omega*input.rho(i)*...
            exp(-1i*k_z(i)*-z(i-1)));
        A(r,1+4*(i-2)+3) = -1*(-1i*omega*input.rho(i)*...
            exp(1i*k_z(i)*-z(i-1)));


        %transverse stress
        A(r+1,1+4*(i-3)+1) = mu(i-1)*(2*k(i-1)^2*...
```

```
        cos(theta(i-1))*sin(theta(i-1)))*...
        exp(-1i*k_z(i-1)*-z(i-1))/(-1i*omega);
A(r+1,1+4*(i-3)+2) = mu(i-1)*(-kappa(i-1)^2*...
        (sin(gamma(i-1))^2-cos(gamma(i-1))^2))*...
        (exp(-1i*kappa_z(i-1)*-z(i-1)))/(-1i*omega);
A(r+1,1+4*(i-3)+3) = mu(i-1)*(2*-k(i-1)^2*...
        cos(theta(i-1))*sin(theta(i-1)))*...
        (exp(1i*k_z(i-1)*-z(i-1)))/(-1i*omega);
A(r+1,1+4*(i-3)+4) = mu(i-1)*(-kappa(i-1)^2*...
        (sin(gamma(i-1))^2-cos(gamma(i-1))^2))*...
        exp(1i*kappa_z(i-1)*-z(i-1))/(-1i*omega);
A(r+1,1+4*(i-2)+1) = 0;
A(r+1,1+4*(i-2)+3) = 0;


%normal velocity
A(r+2,1+4*(i-3)+1) = -1i*k(i-1)*cos(theta(i-1))*...
        exp(-1i*k_z(i-1)*-z(i-1));
A(r+2,1+4*(i-3)+2) = 1i*kappa(i-1)*sin(gamma(i-1))*...
        exp(-1i*kappa_z(i-1)*-z(i-1));
A(r+2,1+4*(i-3)+3) = 1i*k(i-1)*cos(theta(i-1))*...
        exp(1i*k_z(i-1)*-z(i-1));
A(r+2,1+4*(i-3)+4) = 1i*kappa(i-1)*sin(gamma(i-1))*...
        exp(1i*kappa_z(i-1)*-z(i-1));
A(r+2,1+4*(i-2)+1) = -1*(-1i*k(i)*cos(theta(i))*...
        exp(-1i*k_z(i)*-z(i-1)));
A(r+2,1+4*(i-2)+3) = -1*(1i*k(i)*cos(theta(i))*...
        exp(1i*k_z(i)*-z(i-1)));


% set shear components in i-th fluid to 0
```

```
        A(r+3,1+4*(i-2)+2) = 1;
        A(r+4,1+4*(i-2)+4) = 1;


        r = r+5;
    end


elseif input.type(i) == 's'
    if input.type(i-1)=='s'


        %normal stress
        A(r,1+4*(i-3)+1) = (lambda(i-1)*-k(i-1)^2+...
            2*mu(i-1)*-k(i-1)^2*cos(theta(i-1))^2)*...
            exp(-1i*k_z(i-1)*-z(i-1))/(-1i*omega);
        A(r,1+4*(i-3)+2) = 2*mu(i-1)*kappa(i-1)^2*...
            cos(gamma(i-1))*sin(gamma(i-1))*...
            exp(-1i*kappa_z(i-1)*-z(i-1))/(-1i*omega);
        A(r,1+4*(i-3)+3) = (lambda(i-1)*-k(i-1)^2+...
            2*mu(i-1)*-k(i-1)^2*cos(theta(i-1))^2)*...
            exp(1i*k_z(i-1)*-z(i-1))/(-1i*omega);
        A(r,1+4*(i-3)+4) = 2*mu(i-1)*-kappa(i-1)^2*...
            cos(gamma(i-1))*sin(gamma(i-1))*...
            exp(1i*kappa_z(i-1)*-z(i-1))/(-1i*omega);
        A(r,1+4*(i-2)+1) = -1*((lambda(i)*-k(i)^2+...
            2*mu(i)*-k(i)^2*cos(theta(i))^2)*...
            exp(-1i*k_z(i)*-z(i-1))/(-1i*omega));
        A(r,1+4*(i-2)+2) = -1*(2*mu(i)*kappa(i)^2*...
            cos(gamma(i))*sin(gamma(i))*...
            exp(-1i*kappa_z(i)*-z(i-1))/(-1i*omega));
        A(r,1+4*(i-2)+3) = -1*((lambda(i)*-k(i)^2+...
```

```
            2*mu(i)*-k(i)^2*cos(theta(i))^2)*...
            exp(1i*k_z(i)*-z(i-1))/(-1i*omega));
A(r,1+4*(i-2)+4) = -1*(2*mu(i)*-kappa(i)^2*...
            cos(gamma(i))*sin(gamma(i))*...
            exp(1i*kappa_z(i)*-z(i-1))/(-1i*omega));


%tangential stress
A(r+1,1+4*(i-3)+1) = mu(i-1)*(2*k(i-1)^2*...
            cos(theta(i-1))*sin(theta(i-1)))*...
            exp(-1i*k_z(i-1)*-z(i-1))/(-1i*omega);
A(r+1,1+4*(i-3)+2) = mu(i-1)*(kappa(i-1)^2*...
            (-sin(gamma(i-1))^2+cos(gamma(i-1))^2))*...
            (exp(-1i*kappa_z(i-1)*-z(i-1)))/(-1i*omega);
A(r+1,1+4*(i-3)+3) = mu(i-1)*(2*-k(i-1)^2*...
            cos(theta(i-1))*sin(theta(i-1)))*...
            (exp(1i*k_z(i-1)*-z(i-1)))/(-1i*omega);
A(r+1,1+4*(i-3)+4) = mu(i-1)*(kappa(i-1)^2*...
            (-sin(gamma(i-1))^2+cos(gamma(i-1))^2))*...
            exp(1i*kappa_z(i-1)*-z(i-1))/(-1i*omega);
A(r+1,1+4*(i-2)+1) = -1*(mu(i)*(2*k(i)^2*...
            cos(theta(i))*sin(theta(i)))*...
            exp(-1i*k_z(i)*-z(i-1))/(-1i*omega));
A(r+1,1+4*(i-2)+2) = -1*(mu(i)*(kappa(i)^2*...
            (-sin(gamma(i))^2+cos(gamma(i))^2))*...
            (exp(-1i*kappa_z(i)*-z(i-1)))/(-1i*omega));
A(r+1,1+4*(i-2)+3) = -1*(mu(i)*(2*-k(i)^2*...
            cos(theta(i))*sin(theta(i)))*...
            (exp(1i*k_z(i)*-z(i-1)))/(-1i*omega));
A(r+1,1+4*(i-2)+4) = -1*(mu(i)*(kappa(i)^2*...
```

```
        (-sin(gamma(i))^2+cos(gamma(i))^2))*...

        exp(1i*kappa_z(i)*-z(i-1))/(-1i*omega));


%normal velocity
A(r+2,1+4*(i-3)+1) = 1i* -k(i-1)*cos(theta(i-1))*...

        exp(-1i*k_z(i-1)*-z(i-1));
A(r+2,1+4*(i-3)+2) = 1i*kappa(i-1)*sin(gamma(i-1))*...

        exp(-1i*kappa_z(i-1)*-z(i-1));
A(r+2,1+4*(i-3)+3) = 1i*k(i-1)*cos(theta(i-1))*...

        exp(1i*k_z(i-1)*-z(i-1));
A(r+2,1+4*(i-3)+4) = 1i*kappa(i-1)*sin(gamma(i-1))*...

        exp(1i*kappa_z(i-1)*-z(i-1));
A(r+2,1+4*(i-2)+1) = -1*(1i*-k(i)*cos(theta(i))*...

        exp(-1i*k_z(i)*-z(i-1)));
A(r+2,1+4*(i-2)+2) = -1*(1i*kappa(i)*sin(gamma(i))*...

        exp(-1i*kappa_z(i)*-z(i-1)));
A(r+2,1+4*(i-2)+3) = -1*(1i*k(i)*cos(theta(i))*...

        exp(1i*k_z(i)*-z(i-1)));
A(r+2,1+4*(i-2)+4) = -1*(1i*kappa(i)*sin(gamma(i))*...

        exp(1i*kappa_z(i)*-z(i-1)));


%tangential velocity
A(r+3,1+4*(i-3)+1) = 1i*k(i-1)*sin(theta(i-1))*...

        exp(1i * -k_z(i-1) * -z(i-1));
A(r+3,1+4*(i-3)+2) = -1i*-kappa(i-1)*cos(gamma(i-1))*...

        exp(1i * -kappa_z(i-1) * -z(i-1));
A(r+3,1+4*(i-3)+3) = 1i*k(i-1)*sin(theta(i-1))*...

        exp(1i * k_z(i-1) * -z(i-1));
A(r+3,1+4*(i-3)+4) = -1i*kappa(i-1)*cos(gamma(i-1))*...
```

```
            exp(1i * kappa_z(i-1) * -z(i-1));
        A(r+3,1+4*(i-2)+1) = -1*( 1i*k(i)*sin(theta(i))*...
            exp(1i * -k_z(i) * -z(i-1) ) );
        A(r+3,1+4*(i-2)+2) = -1*(-1i*-kappa(i)*cos(gamma(i))*...
            exp(1i * -kappa_z(i) * -z(i-1)) );
        A(r+3,1+4*(i-2)+3) = -1*( 1i*k(i)*sin(theta(i))*...
            exp(1i * k_z(i) * -z(i-1)) );
        A(r+3,1+4*(i-2)+4) = -1*(-1i*kappa(i)*cos(gamma(i))*...
            exp(1i * kappa_z(i) * -z(i-1)) );


        r = r+4;


    elseif input.type(i-1)=='f' %fluid-solid interface
        %normal stress
        A(r,1+4*(i-3)+1) = -1*(-1i*omega*input.rho(i-1)*...
            exp(-1i*k_z(i-1)*-z(i-1)));
        A(r,1+4*(i-3)+3) = -1*(-1i*omega*input.rho(i-1)*...
            exp(1i*k_z(i-1)*-z(i-1)));
        A(r,1+4*(i-2)+1) = (lambda(i)*-k(i)^2+2*mu(i)*...
            -k(i)^2*cos(theta(i))^2*...
            exp(-1i*k_z(i)*-z(i-1))/(-1i*omega);
        A(r,1+4*(i-2)+2) = 2*mu(i)*kappa(i)^2*...
            cos(gamma(i))*sin(gamma(i))*...
            exp(-1i*kappa_z(i)*-z(i-1))/(-1i*omega);
        A(r,1+4*(i-2)+3) = (lambda(i)*-k(i)^2+2*mu(i)*...
            -k(i)^2*cos(theta(i))^2*...
            exp(1i*k_z(i)*-z(i-1))/(-1i*omega);
        A(r,1+4*(i-2)+4) = 2*mu(i)*-kappa(i)^2*...
            cos(gamma(i))*sin(gamma(i))*...
```

```
        exp(1i*kappa_z(i)*-z(i-1))/(-1i*omega);


%transverse stress
A(r+1,1+4*(i-3)+1) = 0;
A(r+1,1+4*(i-3)+3) = 0;
A(r+1,1+4*(i-2)+1) = mu(i)*2* k(i)^2*cos(theta(i))*...
    sin(theta(i))*exp(-1i*k_z(i)*-z(i-1))/(-1i*omega);
A(r+1,1+4*(i-2)+2) = mu(i)*(-kappa(i)^2*...
    (sin(gamma(i))^2-cos(gamma(i))^2))*...
    exp(-1i*kappa_z(i)*-z(i-1))/(-1i*omega);
A(r+1,1+4*(i-2)+3) = mu(i)*(2*-k(i)^2*cos(theta(i))*...
    sin(theta(i)))*exp(1i*k_z(i)*-z(i-1))/(-1i*omega);
A(r+1,1+4*(i-2)+4) = mu(i)*(-kappa(i)^2*...
    (sin(gamma(i))^2-cos(gamma(i))^2))*...
    exp(1i*kappa_z(i)*-z(i-1))/(-1i*omega);


%normal velocity
A(r+2,1+4*(i-3)+1) = -1*(-1i*k(i-1)*cos(theta(i-1))*...
    exp(-1i*k_z(i-1)*-z(i-1)));
A(r+2,1+4*(i-3)+3) = -1*(1i*k(i-1)*cos(theta(i-1))*...
    exp(1i*k_z(i-1)*-z(i-1)));
A(r+2,1+4*(i-2)+1) = -1i*k(i)*cos(theta(i))*...
    exp(-1i*k_z(i)*-z(i-1));
A(r+2,1+4*(i-2)+2) = 1i*kappa(i)*sin(gamma(i))*...
    exp(-1i*kappa_z(i)*-z(i-1));
A(r+2,1+4*(i-2)+3) = 1i*k(i)*cos(theta(i))*...
    exp(1i*k_z(i)*-z(i-1));
A(r+2,1+4*(i-2)+4) = 1i*kappa(i)*sin(gamma(i))*...
    exp(1i*kappa_z(i)*-z(i-1));
```

```
                r = r+3;
            end
        end
    end
end


if N>2
    i = N; %final layer - only outgoing long (into infinite fluid)


    if input.type(N-1) == 'f'
        %pressure
        A(PSI_N-1,1+4*(i-3)+1) = -1i*omega*input.rho(i-1)...
            * exp(- 1i * k_z(i-1) * -z(i-1)); %incoming long
        A(PSI_N-1,1+4*(i-3)+3) = -1i*omega*input.rho(i-1)...
            * exp( 1i * k_z(i-1) * -z(i-1)); %reflected long
        A(PSI_N-1,1+4*(i-2)+1) = -1*(-1i*omega*input.rho(i)....
            * exp( -1i * k_z(i) * -z(i-1))); %transmitted long long


        %velocity
        A(PSI_N,1+4*(i-3)+1) = -k(i-1)*cos(theta(i-1))...
            *exp(-1i * k_z(i-1) * -z(i-1));
        A(PSI_N,1+4*(i-3)+3) =  k(i-1)*cos(theta(i-1))...
            *exp(1i * k_z(i-1) * -z(i-1));
        A(PSI_N,1+4*(i-2)+1) =  -1*(-k(i)*cos(theta(i))...
            *exp(-1i * k_z(i) * -z(i-1))); %outgoing long


    elseif input.type(N-1) == 's'
```

```
%normal stress
A(PSI_N-2,1+4*(i-3)+1) = (lambda(i-1)*-k(i-1)^2+...
    2*mu(i-1)*-k(i-1)^2*cos(theta(i-1))^2)...
    *exp(-1i*k_z(i-1)*-z(i-1))/(-1i*omega);
A(PSI_N-2,1+4*(i-3)+2) = 2*mu(i-1)*kappa(i-1)^2*...
cos(gamma(i-1))*sin(gamma(i-1))...
    *exp(-1i*kappa_z(i-1)*-z(i-1))/(-1i*omega);
A(PSI_N-2,1+4*(i-3)+3) = (lambda(i-1)*-k(i-1)^2+...
2*mu(i-1)*-k(i-1)^2*cos(theta(i-1))^2)...
    *exp(1i*k_z(i-1)*-z(i-1))/(-1i*omega);
A(PSI_N-2,1+4*(i-3)+4) = 2*mu(i-1)*-kappa(i-1)^2*...
cos(gamma(i-1))*sin(gamma(i-1))*exp(1i*kappa_z(i-1)...
    *-z(i-1))/(-1i*omega);
A(PSI_N-2,1+4*(i-2)+1) = -1*(-1i*omega*input.rho(i)*...
    exp(-1i*k_z(i)*-z(i-1)));


%transverse stress
A(PSI_N-1,1+4*(i-3)+1) = mu(i-1)*2*k(i-1)^2*cos(theta(i-1))...
    *sin(theta(i-1))*exp(-1i*k_z(i-1)*-z(i-1))/(-1i*omega);
A(PSI_N-1,1+4*(i-3)+2) = mu(i-1)*(-kappa(i-1)^2*...
(sin(gamma(i-1))^2-cos(gamma(i-1))^2))...
    *(exp(-1i*kappa_z(i-1)*-z(i-1)))/(-1i*omega);
A(PSI_N-1,1+4*(i-3)+3) = mu(i-1)*(2*-k(i-1)^2*...
cos(theta(i-1))*sin(theta(i-1)))...
    *(exp(1i*k_z(i-1)*-z(i-1)))/(-1i*omega);
A(PSI_N-1,1+4*(i-3)+4) = mu(i-1)*(-kappa(i-1)^2*...
(sin(gamma(i-1))^2-cos(gamma(i-1))^2))...
    *exp(1i*kappa_z(i-1)*-z(i-1))/(-1i*omega);
A(PSI_N-1,1+4*(i-2)+1) = 0;
```

```
        %normal velocity
        A(PSI_N,1+4*(i-3)+1) = -1i*k(i-1)*cos(theta(i-1))...
            *exp(-1i*k_z(i-1)*-z(i-1));
        A(PSI_N,1+4*(i-3)+2) = 1i*kappa(i-1)*sin(gamma(i-1))...
            *exp(-1i*kappa_z(i-1)*-z(i-1));
        A(PSI_N,1+4*(i-3)+3) = 1i*k(i-1)*cos(theta(i-1))...
            *exp(1i*k_z(i-1)*-z(i-1));
        A(PSI_N,1+4*(i-3)+4) = 1i*kappa(i-1)*sin(gamma(i-1))...
            *exp(1i*kappa_z(i-1)*-z(i-1));
        A(PSI_N,1+4*(i-2)+1) = -1*(-1i*k(i)*cos(theta(i))...
            *exp(-1i*k_z(i)*-z(i-1)));


    end
end


PSI.pot = inv(A)*B;


if nargin>3
    states = MLstate_calc(input, PSI, x_req,makeplot);
else
    states = '';
end
```

APPENDIX B: MULTI-LAYER STATE CALCULATION CODE

This code calculates position-based states for the model presented in Chapter 5. When given the input parameters for the model along with the solutions obtained using the code in Appendix A, the calculation of pressure, stress, velocity, and intensity is performed at the requested positions.

The inputs for the model are the input parameters of geometry and material properties in the system (the same input used in Appendix A), the solutions obtained by the code in Appendix A, and the position vector for calculation. The resulting output is a structure containing all the material states, including intensity and reference input parameters, for each position.

```
function states = MLstate(input, PSI, x,makeplot)


%EDITS 4/30 - added conditions for infinite solid interface


if nargin<4
    makeplot = 'n';
end


%compute states in material (as a function of incoming pressure)


%initial propagation angle basked into solution?


N = length(input.type); %number of layers


omega = 2*pi * PSI.f;


mu = input.b.^2.*input.rho;
lambda = input.c.^2.*input.rho-2*mu;
```

```
%compute x-coordinates of borders
z=zeros(1,N-1);


z(1) = 0;
for i = 2:N-1;
    z(i) = sum(input.L(2:i));
end


k = omega./input.c;
kappa = omega./input.b;
k_x = k.*sin(PSI.theta);
k_z = k.*cos(PSI.theta);
kappa_x = kappa.*sin(PSI.gamma);
kappa_z = kappa.*cos(PSI.gamma);


%if borders (z) not present, add to system


for i = 1:length(z)
    ind = find(z(i)>=x,1,'last');
    % add a second point if already there
    if length(ind)==0


        x = [z(1) z(1) x];
    else


        x = [x(1:ind) z(i) x(ind+1:end)];
        if x(ind) ~= z(i)
            x = [x(1:ind) z(i) x(ind+1:end)];
```

```
        end
    end
end


states.x = x;


%reference intensity - intensity at z = 0;
I_ref = 1/2*real(-1i*omega*input.rho(1) * conj(1i*k_z(1)* (-1)));


j = 1; %start on first layer


for i = 1:length(x) %cycle through all points


    if j == 1
        Zz_in = -1i*omega*input.rho(1) * (1*exp(-1i*k_z(1)*-x(i)));
        Zz_out = -1i*omega*input.rho(1) * (PSI.pot(1)*...
            exp(1i*k_z(1)*-x(i)));
        Vz_in = 1i*k_z(1)* (-1*exp(-1i*k_z(1)*-x(i)));
        Vz_out = 1i*k_z(1)* (PSI.pot(1)*exp(1i*k_z(1)*-x(i)));


        states.Zz(i) = Zz_in+Zz_out;
        states.Zx(i) = 0;
        states.Vz(i) = Vz_in+Vz_out;
        states.Vx(i) = 1i*k_x(j)*(PSI.pot(1)*exp(1i*k_z(1)*-x(i))+...
            1*exp(-1i*k_z(1)*-x(i)));


        states.I(1,i) = 1/2*real(Zz_out*conj(Vz_out));
```

```
elseif j == N

    if input.type(j) == 'f'

        Zz_out = -1i*omega*input.rho(N) *...
            (PSI.pot(1+4*(N-2)+1)*exp(-1i*k_z(N)*-x(i)));

        Vz_out = -1i*k_z(N)*PSI.pot(1+4*(N-2)+1)*...
            exp(-1i*k_z(N)*-x(i));


        states.Zz(i) = Zz_out;

        states.Zx(i) = 0;

        states.Vz(i) = Vz_out;

        states.Vx(i) = 1i*k_x(N)*PSI.pot(1+4*(N-2)+1)*...
            exp(-1i*k_z(N)*-x(i));


        states.I(1+4*(N-2)+1,i) = 1/2*real(Zz_out*conj(Vz_out));


    elseif input.type(j) == 's'


        Zz_forward = ((lambda(j)*-k(j)^2+2*mu(j)*-k_z(j)^2)*...
            PSI.pot(1+4*(j-2)+1)*exp(-1i*k_z(j)*-x(i))...
            +2*mu(j)*kappa_z(j)*kappa_x(j)*PSI.pot(1+4*(j-2)+2)*...
            exp(-1i*kappa_z(j)*-x(i)))/(-1i*omega);


        Vz_forward = (1i*k_z(j)*-PSI.pot(1+4*(j-2)+1)*...
            exp(-1i*k_z(j)*-x(i))+1i*kappa_x(j)*...
            PSI.pot(1+4*(j-2)+2)*exp(-1i*kappa_z(j)*-x(i)));


        Zx_forward = mu(j)*(2*k_x(j)*k_z(j)*PSI.pot(1+4*(j-2)+1)*...
            exp(-1i*k_z(j)*-x(i))+(-kappa_x(j)^2+kappa_z(j)^2)*...
            PSI.pot(1+4*(j-2)+2)*exp(-1i*kappa_z(j)*-x(i)))/...
```

```
                (-1i*omega);


        Vx_forward = (1i*k_x(j)*PSI.pot(1+4*(j-2)+1)*...
            exp(-1i*k_z(j)*-x(i))-1i*kappa_z(j)*...
            -PSI.pot(1+4*(j-2)+2)*exp(-1i*kappa_z(j)*-x(i)));


        states.Zz(i) = Zz_forward;
        states.Zx(i) = Zx_forward;
        states.Vz(i) = Vz_forward;
        states.Vx(i) = Vx_forward;


        states.I(1+4*(j-2)+1,i) = 1/2*real(Zz_forward*...
            conj(Vz_forward));
        states.I(1+4*(j-2)+2,i) = 1/2*real(Zx_forward*...
            conj(Vx_forward));


    end


else


    if input.type(j) == 'f'


        Zz_forward = -1i*omega*input.rho(j)*...
            (PSI.pot(1+4*(j-2)+1)*exp(-1i*k_z(j)*-x(i)));
        Zz_backward = -1i*omega*input.rho(j) *...
            (PSI.pot(1+4*(j-2)+3)*exp(1i*k_z(j)*-x(i)));
        Vz_forward = 1i*k_z(j)*...
            -PSI.pot( 1+4*(j-2)+1)*exp(-1i*k_z(j)*-x(i));
        Vz_backward = 1i*k_z(j)*...
```

```
            PSI.pot(1+4*(j-2)+3)*exp(1i*k_z(j)*-x(i));


        states.Zz(i) = Zz_forward + Zz_backward;
        states.Zx(i) = 0;
        states.Vz(i) = Vz_forward + Vz_backward;
        states.Vx(i) = 1i*k_x(j)*(PSI.pot( 1+4*(j-2)+1)*...
            exp(-1i*k_z(j)*-x(i))+PSI.pot(1+4*(j-2)+3)*...
            exp(1i*k_z(j)*-x(i)));


        states.I(1+4*(j-2)+1,i) = 1/2*real(Zz_forward*...
            conj(Vz_forward));
        states.I(1+4*(j-2)+3,i) = 1/2*real(Zz_backward*...
            conj(Vz_backward));


    elseif input.type(j) == 's'


        Zz_forward = ((lambda(j)*-k(j)^2+2*mu(j)*-k_z(j)^2)*...
            PSI.pot(1+4*(j-2)+1)*exp(-1i*k_z(j)*-x(i))+2*mu(j)*...
            kappa_z(j)*kappa_x(j)*PSI.pot(1+4*(j-2)+2)*...
            exp(-1i*kappa_z(j)*-x(i)))/(-1i*omega);
        Zz_backward =((lambda(j)*-k(j)^2+2*mu(j)*-k_z(j)^2)*...
            PSI.pot(1+4*(j-2)+3)*exp(1i*k_z(j)*-x(i))+2*mu(j)*...
            -kappa_z(j)*kappa_x(j)*PSI.pot(1+4*(j-2)+4)*...
            exp(1i*kappa_z(j)*-x(i)))/(-1i*omega);


        Vz_forward = (1i*k_z(j)*-PSI.pot(1+4*(j-2)+1)*...
            exp(-1i*k_z(j)*-x(i))+1i*kappa_x(j)*...
            PSI.pot(1+4*(j-2)+2)*exp(-1i*kappa_z(j)*-x(i)));
        Vz_backward = (1i*k_z(j)*PSI.pot(1+4*(j-2)+3)*...
```

```
        exp(1i*k_z(j)*-x(i))+1i*kappa_x(j)*...
        PSI.pot(1+4*(j-2)+4)*exp(1i*kappa_z(j)*-x(i)));


    Zx_forward = mu(j)*(2*k_x(j)*k_z(j)*PSI.pot(1+4*(j-2)+1)*...
        exp(-1i*k_z(j)*-x(i))...
        +(-kappa_x(j)^2+kappa_z(j)^2)*PSI.pot(1+4*(j-2)+2)*...
        exp(-1i*kappa_z(j)*-x(i)))/(-1i*omega);
    Zx_backward = mu(j)*(2*k_x(j)*k_z(j)*...
        -PSI.pot(1+4*(j-2)+3)*exp(1i*k_z(j)*-x(i))...
        +(-kappa_x(j)^2+kappa_z(j)^2)*PSI.pot(1+4*(j-2)+4)*...
        exp(1i*kappa_z(j)*-x(i)))/(-1i*omega);


    Vx_forward = (1i*k_x(j)*PSI.pot(1+4*(j-2)+1)*...
        exp(-1i*k_z(j)*-x(i))-1i*kappa_z(j)*...
        -PSI.pot(1+4*(j-2)+2)*exp(-1i*kappa_z(j)*-x(i)));
    Vx_backward =  (1i*k_x(j)*PSI.pot(1+4*(j-2)+3)*...
        exp(1i*k_z(j)*-x(i))-1i*kappa_z(j)*...
        PSI.pot(1+4*(j-2)+4)*exp(1i*kappa_z(j)*-x(i)));


    states.Zz(i) = Zz_forward + Zz_backward;
    states.Zx(i) = Zx_forward + Zx_backward;
    states.Vz(i) = Vz_forward + Vz_backward;
    states.Vx(i) = Vx_forward + Vx_backward;


    states.I(1+4*(j-2)+1,i) = 1/2*real(Zz_forward*...
        conj(Vz_forward));
    states.I(1+4*(j-2)+2,i) = 1/2*real(Zx_forward*...
        conj(Vx_forward));
    states.I(1+4*(j-2)+3,i) = 1/2*real(Zz_backward*...
```

```
                    conj(Vz_backward));
                states.I(1+4*(j-2)+4,i) = 1/2*real(Zx_backward*...
                    conj(Vx_backward));


            end
        end


        if j~=N
            if z(j) == x(i) && z(j) == x(i+1)
                %compute on both sides of the material border..
                %(increases j by one after first border x value)
                j = j+1;


            end
        end
end


%normalize against incoming pressure

states.Pin = -1i*omega*input.rho(1);

states.Zz = states.Zz/states.Pin;
states.Zx = states.Zx/states.Pin;
states.Vz = states.Vz/states.Pin;
states.Vx = states.Vx/states.Pin;

states.I= states.I./I_ref;
states.I_ref = I_ref;
```

```
states.I1(1) = states.I(1,1)+1;


for i = 2:length(x)


    if states.x(i)<=0 && states.x(i-1)~=0
        states.I1 = states.I(1,:)+1;
    else
        states.I1(i) = 0;
    end
end



%calculat Iz, Ix for each component

if strcmp(makeplot, 'n')~=1
    % %plot data
    figure
    subplot(221)
    hold on
    plot(states.x,abs(states.Zz))
    plot(states.x,real(states.Zz),'r')
    axis tight
    borderlines(z,input)
    plot(states.x,abs(states.Zz)); plot(states.x,real(states.Zz),'r')
    ylabel('Longitudinal Stress')
    subplot(222)
    hold on
    plot(states.x,abs(states.Vz))
    plot(states.x,real(states.Vz),'r')
```

```
    axis tight

    borderlines(z,input)

    plot(states.x,abs(states.Vz)); plot(states.x,real(states.Vz),'r')

    ylabel('Longitudinal Velocity')

    subplot(223)

    hold on

    plot(states.x,abs(states.Zx))

    plot(states.x,real(states.Zx),'r')

    axis tight

    borderlines(z,input)

    plot(states.x,abs(states.Zx)); plot(states.x,real(states.Zx),'r')

    ylabel('Transverse Stress')

    subplot(224)

    hold on

    plot(states.x,abs(states.Vx))

    plot(states.x,real(states.Vx),'r')

    axis tight

    borderlines(z,input)

    plot(states.x,abs(states.Vx)); plot(states.x,real(states.Vx),'r')

    ylabel('Transverse Velocity')
end
end


function borderlines(z,input)
[Ybounds] = get(gca,'YLim');


if nargin<2
    for j = 1:length(z)
        plot([z(j) z(j)], Ybounds,'--k')
```

```
        end


else
    %make rectangles corresponding to types instead!
    rheight = Ybounds(2)-Ybounds(1)+2;
    for j = 2:(length(input.type)-1)
        rwidth = z(j)-z(j-1);
        if input.type(j)=='s' %orange rectangle
            rectangle('Position',[z(j-1),Ybounds(1)-1,rwidth,...
                rheight],'FaceColor',[255 177 86]/255,'Linestyle','--')
        elseif input.type(j)=='f'
            rectangle('Position',[z(j-1),Ybounds(1)-1,rwidth,...
                rheight],'FaceColor',[128 207 110]/255,'Linestyle','--')
        end
    end
end
end
```

APPENDIX C: MULTI-SOURCE CODE

The code below is the code for the model presented in Chapter 4 for generating plane and evanescent wave pressure distributions using a source array. The model is input with the desired frequency and angle of plane wave to be modeled (an evanescent wave can be modeled using a complex angle of incidence), along with the length of the pressure distribution, the standoff of the array, and the length and number of sources in the array. It outputs a vector of the monopole source amplitudes (which incorporate phase through a complex component), the resulting approximate pressure and velocity generated, the correlation coefficients for both pressure and the velocity, and the position, pressure, and velocity vectors for the ideal pressure distribution.

The program first generates the ideal plane wave pressure and velocity, then constructs the matrix for calculation. Once the complex amplitudes of the sources has been found, the program calculates the pressure and velocity resulting from the multiple sources and the correlation coefficients of the pressure and velocity distributions.

```
function [A,Papprox,Vapprox,R_sq,X,Pideal,Videal,PdzApprox] =...
    PV_approx(f,angle,L_x,Z0,L,N,phaseshift)

if nargin<7
    phaseshift = 0;
end

%approximates monopole source strength using least-squares formulation
%OUTPUTS:
% A - source strengths
% Papprox - resulting pressure distribution in space
% Vapprox - resulting velocity distribution in space
% R_sq.P - fit coefficient for the pressure
% R_sq.V - fit coefficient for the velocity
```

```
% X - x-coordinates for
% Pideal - ideal pressure on surface (to be fit)
% Videal - ideal velocity on surface
%INPUTS:
% f - frequency
% angle - complex angle of incidence
% L_x - length of desired pressure distribution
% Z0 - standoff distance of array
% L - length of array
% N - number of sources


% air material properties
c = 343;
rho = 1.2;


% functions of frequency
omega = 2*pi*f;
k = omega/c;


theta = real(angle)*pi/180+imag(angle)*1i; %incident angle in radians


X = linspace(-L_x/2,L_x/2,1024)'; %position vector


%ideal pressure/velocity distributions
Pideal = exp(1i*k*sin(theta)*X+phaseshift*pi/180)';
Videal = -k*cos(theta)/(omega*rho)*exp(1i*k*sin(theta)*X+phaseshift*pi/180)';


% source posiion vector
Y_x = linspace(-L/2,L/2,N)'; % x-positions
```

```
Y = [Y_x Z0*ones(N,1)]; %matrix of x,y positions


%construct green's function matrix
G_P = zeros(length(X),N);


for i = 1:length(X)
    for j = 1:N


        %Green's function for distance r from source to point
        r = sqrt((X(i,1)-Y(j,1))^2+(Y(j,2))^2);
        H(i,j) = exp(1i*k*r)/(r);


    end
end


%solve system HA = B for A
B = Pideal';
A = pinv(H'*H)*H'*B;


% generate pressure, velocity from sources
Papprox = zeros(length(X),1);
Vapprox = zeros(length(X),1);


%compute approximate pressure, velocity distributions
for j = 1:N
    for i = 1:length(X)


        r(i) = sqrt((X(i,1)-Y(j,1))^2+(Y(j,2))^2);
        phi(i) = atan((X(i,1)-Y(j,1))/Y(j,2));
```

```
        Papprox(i) = Papprox(i)+A(j)*exp(1i*k*r(i))/(r(i));

        Vapprox(i) = Vapprox(i)-A(j)*1/(rho*c)*...

            (1-1/(1i*k*r(i)))*exp(1i*k*r(i))/(r(i))*cos(phi(i));


    end

end


%calculate R from P,V
MSE.P= sqrt(sum((real(Pideal)-real(Papprox')).^2));
RMS.P = sqrt(sum(real(Pideal).^2));


MSE.V = sqrt(sum((real(Videal)-real(Vapprox')).^2));
RMS.V = sqrt(sum(real(Videal).^2));


R_sq.P = 1-MSE.P/RMS.P;
R_sq.V = 1-MSE.V/RMS.V;
```

VITA

VITA

Andrew M. Jessop is a native of San Diego, California and majored in Mechanical Engineering and Material Science Engineering, with a Minor in Physics, at the University of California at Berkeley. After graduating in 2004, he worked in Oakland, California for three years as an acoustical consultant with Wilson Ihrig and Associates, primarily focusing on data collection and analysis of transportation noise and vibration.

Andrew came to Purdue in 2007 eager to expand his knowledge of acoustics, and found the field of structural acoustics to his liking. His Masters Thesis was on the effects of non-periodic stiffening on the sound transmission of windows, and was completed in 2009. This thesis work won him recognition as the FAA Center of Excellence's Outstanding Graduate Researcher in 2009. The work in this dissertation was preceded by additional work on the tire acoustic mode, focusing on detection of the mode by external means. That work won a student paper competition prize at NoiseCon 2010.

In his spare time, Andrew (who goes by "Andy") enjoys photography and triathlon training - swimming, biking, and running. If he had more spare time, he might enjoying racing triathlons.